

FREQUENCY CONVERSION IN NEAR-STOICHIOMETRIC
LITHIUM TANTALATE FABRICATED BY VAPOR TRANSPORT
EQUILIBRATION

A DISSERTATION
SUBMITTED TO THE DEPARTMENT OF ELECTRICAL
ENGINEERING
AND THE COMMITTEE ON GRADUATE STUDIES
OF STANFORD UNIVERSITY
IN PARTIAL FULFILLMENT OF THE REQUIREMENTS
FOR THE DEGREE OF
DOCTOR OF PHILOSOPHY

David Hum

March 2007

© Copyright by David Hum 2007
All Rights Reserved

I certify that I have read this dissertation and that, in my opinion, it is fully adequate in scope and quality as a dissertation for the degree of Doctor of Philosophy.

Martin M. Fejer Principal Adviser

I certify that I have read this dissertation and that, in my opinion, it is fully adequate in scope and quality as a dissertation for the degree of Doctor of Philosophy.

Robert L. Byer

I certify that I have read this dissertation and that, in my opinion, it is fully adequate in scope and quality as a dissertation for the degree of Doctor of Philosophy.

David A. B. Miller

Approved for the University Committee on Graduate Studies.

Abstract

Near-stoichiometric lithium tantalate (SLT) crystals were produced from congruent lithium tantalate by vapor transport equilibration (VTE), and several important optical and ferroelectric properties were measured. The effect of vapor transport conditions and surface preparation on reproducible ferroelectric engineering of SLT have been studied. Control of these effects along with dramatic decreases in the sensitivity to photorefractive damage and 532-nm absorption has allowed near-room-temperature generation of 10 W of CW 532-nm radiation by second harmonic generation from 29 W of 1064-nm radiation in a 4-cm-long device. Devices periodically poled for watt-level generation of 589-nm radiation by both second harmonic and sum frequency generation have also been demonstrated. Control of ferroelectric properties allowed periodic poling down to a period of 5 μm suitable for generation of 458.3-nm radiation by second harmonic generation. Investigations into the application of periodic poling and vapor transport equilibration on rotated-cut crystals have led to the development of aperture-scalable, quasi-phasematched devices suitable for high peak- and average-power nonlinear optics.

Acknowledgements

Academic research is a collaborative effort and the work presented in this thesis is no exception. Without the support of my family, friends and colleagues, I would have never achieved the results contained in this document. Although timing and luck speed successful results, persistence and hard work by the individual and support from family and friends are essential. With that in mind, there are several people who have provided me this support and require my gratitude for all their help.

Through my graduate career, I have been fortunate enough to have been advised by Professor Marty Fejer. Marty has been extremely helpful in identifying the critical steps to achieving success. Without fail, Marty will have wonderful suggestions for any perceived obstacle that is the barrier to your goals.

I would like to thank Professor Bob Byer for his overwhelming enthusiasm for all the research takes place at Ginzton. His technical experience and wealth of knowledge has been immeasurably helpful. I would like to thank Professor David Miller, who as well as being my academic advisor, was the first person I met at Stanford and I attribute part of my decision to come to Stanford to him.

Without Dr. Roger Route, none of the experiments would have been possible. Although most fabrication steps were done by myself, the vapor transport equilibration step was in most part executed by Roger. This allowed me to spend my time isolating the key fabrication steps to make this project successful.

A key part of this research was timing. When I joined Marty's research group, Dr. Mordechai (Moti) Katz and Dr. Greg Miller had already spent much of their time starting this project at Stanford. When Moti was leaving, I began to become very interested in this project and I attribute much of this thesis to their hard work.

All of the students at Stanford that I have collaborated with are exceptional but most importantly make research at Stanford an enjoyable and fun place to work. In Marty's group, several students have contributed to this work. Jonathan Kurz, Krishnan Parameswaran, Rosti Roussev and Andy Schober all helped me learn how to conduct optical experiments and how to perform the microfabrication necessary to be successful. I have had the pleasure to work with Xiuping Xie, Carsten Langrock, Jie Huang and Mathieu Charbonneau-Lefort on a day-to-day basis to solve many of the nonlinear optics problems associated with lithium niobate and lithium tantalate. I have enjoyed working and discussing nonlinear optics problems with Paulina Kuo, Joe Schaar, Xiaojun Yu, Luigi Scaccabarozzi and Yijie Huo who all work on gallium arsenide for nonlinear optics. Beyond Marty's group, there are many students in Professor Byer's group that have helped me over the years. Tomas Plettner, Shally Saraf, Arun Sridharan, Supriyo Sinha, Yin-wen Lee, Jeff Wisdom, Patrick Lu, Karel Urbanek, Amber Bullington and Sam Wong have all helped me with their useful discussions about laser equipment and laser experiments.

There is an extended family of Byer/Fejer group members all of whom have provided stimulating conversation and insight into research problems. Dr. Norna Robertson, Dr. Sheila Rowan, Dr. Brian Lantz, Vivian Drew, Dr. Peter Beyersdorf, Dr. Ke-Xun Sun, Dr. Gennady Imeshev, Nancy Christiansen and Tami Reynolds all have contributed to this family atmosphere. Additionally, Alex Alexandrovski, Volodymyr Kondilenko and Ashot Markosyan have helped me measure absorption to levels previously unattainable using the photothermal common-path interferometer. In addition to Moti and Greg, our group has been blessed with several visitors who provide much diversity to our family: Takashi Saida, Matthias Falk, Manfred Mueller.

Process development of the fabrication of the devices in this work was perhaps the most difficult challenge. I would like to thank Paul Jerabek, Mahnaz Mansapour, Mario Vilanova and Mike Martinez in Stanford Nanofabrication Facility for all their help. I would like to thank Tom Carver, organizes and maintains the Ginzton microfabrication facility, for all his useful discussions about fabrication methods and deposition possibilities. I would like to thank Tim Brand and his staff (Marco, Mike and Ryan) for all their help in finishing the fabrication in the Ginzton Crystal Shop.

Working at Stanford has allowed me to collaborate with researchers around the world. I would like to thank Claudia Kajiyama and Dieter Jundt from Crystal Technology, Inc., Alex Drobshoff and Jay Dawson at Lawrence Livermore National Laboratory, Luke Taylor and Yan Feng at the European Southern Observatory, Allen Tracy and Camilo Lopez at Lockheed Martin - Coherent Technologies, Prof. Takunori Taira and Dr. Hideki Ishizuki from the Institute for Molecular Science, Michio Oka and Tatsuo Fukui from Sony Corporation, Junji Hirohashi and Yasu Furukawa from Oxide Corporation and Vladimir Shur from Ural State University.

I would like to thank all my friends and family. Near or far, big or small, my friends are important to me wherever they may reside. I thank all my friends for being supportive during my educational experiences. I would like to thank all my extended family including my cousins, uncles, aunts and grandparents for their support. I would like to thank my parents, Robert and Susan, and my brother, Stan, who have given me their unconditional love and support. Finally, I would like to thank Shirly for her love, support and patience over these last few years.

Contents

Abstract	v
Acknowledgements	vi
1 Introduction	1
1.1 Motivation	1
1.2 Periodically poled materials	2
1.3 Nonlinear Optics	4
1.3.1 Slowly Varying Envelope Approximation	6
1.3.2 Second Harmonic Generation and the Coupled Mode Equations	7
1.3.3 Interactions including focussing and diffraction	15
1.3.4 Sum Frequency Generation	17
1.4 Limitations on Nonlinear Devices	19
1.4.1 Photorefraction	19
1.4.2 Laser-induced damage	23
1.4.3 Absorption	23
1.5 Overview	28
2 Crystal fabrication	30
2.1 Vapor Transport Equilibration of Lithium Tantalate	30
2.2 Experimental Apparatus for VTE	34
2.3 Electric-field poling	36
2.3.1 Domain Visualization	37

3	Properties of VLT	39
3.1	Ferroelectric Properties	39
3.1.1	Coercive Field	39
3.1.2	Domain Wall Velocity	44
3.1.3	Domain Stability and Backswitching	47
3.1.4	Domain Patterning and Domain Instabilities	50
3.2	Optical Properties	54
3.2.1	Nonlinear Coefficient	57
3.2.2	Photorefraction	57
3.2.3	Absorption	62
3.2.4	Optical Damage Threshold	68
3.2.5	Two-photon absorption of 532-nm radiation	70
3.2.6	Ordinary-wave birefringence at 1- and 2- μm wavelengths	71
3.3	Thermal Conductivity	73
4	Conventional z-cut Bulk Devices	78
4.1	Generation of 532-nm radiation by SHG	78
4.2	Generation of 589-nm radiation	86
4.3	Generation of 458.3-nm radiation by SHG	92
5	Rotated cut bulk devices	94
5.1	Motivation	94
5.2	Theory of rotated-cut bulk devices	95
5.3	Ferroelectric Properties of rotated-cut LT	103
5.4	25-degree-rotated, X-cut VLT	105
5.5	Generation of 532-nm radiation by SHG	109
6	Summary and Future Directions	114
6.1	Summary of Contributions	114
6.2	Future Directions	116
6.2.1	Material improvements and characterization	116
6.2.2	Bulk Nonlinear Devices	117

6.2.3	Waveguide Nonlinear Devices	118
6.2.4	Rotated-cut devices	118
6.3	Conclusion and Forward Outlook	118
	Bibliography	120

List of Tables

1.1	Nonlinear coefficients of some widely used nonlinear materials.	13
1.2	Normalized bulk efficiencies for SHG of 532-nm radiation of some commonly used nonlinear materials	17
3.1	Effects of pre-poling and post-poling etching using 50 % HF on attempts to pole an 8 - μm period.	51
3.2	Qualitative observations of the domain stability and periodic poling quality of poled samples after polishing and etching.	53
3.3	Maker fringe measurements of various crystals.	57
3.4	Photorefractive Properties of various VLT samples.	59
3.5	Photorefractive Properties as a function of wavelength for sample 147D.	60
3.6	Absorptivity of VLT samples at various wavelengths. Variations in the absorptivity listed are sample-to-sample variations.	66
3.7	Birefringence and temperature coefficient at 1 and 2 μm	73

List of Figures

1.1	SHG power as a function of phase mismatch	10
1.2	Perfect, quasi- and not phasematched interactions	12
1.3	The effect of focussing on SHG output power	16
1.4	Energy and momentum conservation for SFG	18
1.5	Undistorted gaussian beam compared with a photorefractively distorted beam	21
1.6	Green-induced infrared absorption measured by photothermal common-path interferometry	25
1.7	Contour plot of efficiency versus total dephasing and nonlinear drive .	27
2.1	A phase diagram of LN and the effect of VTE	33
2.2	Process flow chart to fabricate VTE'ed, periodically poled devices. . .	34
2.3	Photograph of the VTE crucible	35
2.4	Diagram of patterned electrodes for periodic poling	36
2.5	Fixtures for periodic poling and ferroelectric characterization	37
2.6	Domain rearrangement from etching with hydrofluoric acid	38
3.1	A typical hysteresis loop for VLT	41
3.2	Coercive field dependence as a function of measurement loop period .	42
3.3	Coercive field as a function of VTE time at 1360 °C	43
3.4	Coercive field uniformity over a typical wafer. The observed 15 V/mm variation corresponds to a difference in $[Li]/([Li]+[Ta])$ of approximately 15 ppm.	44
3.5	Voltage and current races for a typical domain wall velocity measurement	45

3.6	Relative domain wall velocity as a function of applied field	46
3.7	Voltage and current measurements during a typical backswitching measurement	49
3.8	Backswitching field as a function of hold time	50
3.9	Process flow chart shows the positions where polishing or etching could occur	52
3.10	A 2" SLT wafer (202-18) poled with an 8 μm period. Etched +Z and -Z faces are shown inset.	53
3.11	Images of 7- μm -period, 11- μm -period, 32- μm -period poling	55
3.12	Image of 5- μm -period domains	56
3.13	A typical Maker fringe measurement	56
3.14	Experimental diagram of apparatus for measurement of photoconductivity and photogalvanic coefficients.	58
3.15	Experimental diagram of an improved apparatus for photoconductivity and photogalvanism measurements	61
3.16	Reduced current fluctuations using an improved apparatus.	62
3.17	Ultraviolet ordinary and extraordinary wave absorptivities for both CLT and VLT.	64
3.18	Ordinary-wave absorptions for both CLT and VLT in the mid-infrared	67
3.19	Ordinary-wave OH^- absorptions of CLT and VLT.	67
3.20	Diagram of the damage threshold measurement setup	68
3.21	Damage statistics for CLT, CLN and VLT	69
3.22	Two-photon absorption as a function of 532-nm average power	72
3.23	Quasi-phasesmatching wavelengths for SHG of 1- μm radiation with d_{33} , d_{24} (the fundamental polarized along the ordinary and extraordinary axes and the second harmonic polarized along the ordinary axis) and d_{22}	74
3.24	Room-temperature thermal conductivities of various compositions of LT and LN	75
3.25	Temperature dependence of thermal diffusivity of LN	76
3.26	Temperature dependence of thermal diffusivity of LT	77

4.1	Temperature tuning curve of for a 17-mm-long, 8- μ m-period VLT for 532-nm SHG	79
4.2	SHG conversion efficiency versus time measured for 1000 hours	80
4.3	532-nm SHG output power as a function of input infrared power	82
4.4	Temperature tuning curve for 532-nm SHG at 10-W CW.	83
4.5	SHG output power as a function of time for a high peak intensity experiment	84
4.6	SHG temperature tuning curve for a 12-mm-long grating generating 532-nm radiation	85
4.7	Wavelength tuning curve for generation of \sim 589-nm radiation by SFG	88
4.8	Generated 589-nm power as a function of input powers	89
4.9	Temperature tuning curve for the generation of 589-nm radiation by SHG	90
4.10	Generation of 3.25 W of 589-nm radiation by SHG	91
4.11	Temperature tuning curve for 458.3-nm SHG	93
5.1	Topology for large-aperture periodically poled crystals	95
5.2	The input face of a rotated-cut periodically poled ferroelectric	97
5.3	Vector diagram of a noncollinear QPM process	98
5.4	Theoretical tuning curves for 532-nm SHG in a 25-degree-rotated, X-cut VLT crystal	100
5.5	Theoretical nonlinear drive and efficiency for 532-nm SHG as a function of pulse width	102
5.6	Theoretical nonlinear drive and efficiency for 532-nm SHG as a function of pulse width	103
5.7	“Apparent” ferroelectric properties change in a rotated-cut crystal	104
5.8	Rotated-cut LN cracks before domain inversion	105
5.9	Side etching of a rotated-cut VTE’ed LN sample.	106
5.10	Periodic poling of a 42-degree-rotated, Y-cut VLT crystal	107
5.11	SHG in a 25-degree-rotated, X-cut VLT crystal	108
5.12	Hysteresis loop of a 25-degree-rotated, X-cut VLT crystal	110

5.13 Angle tuning curve of a 25-degree-rotated, 8- μm -period sample. (Inset)
 A photograph of the side etching of the 8- μm domains 111

5.14 A spatial profile of the generated 532-nm power as a function of position 113

Chapter 1

Introduction

1.1 Motivation

Studies into nonlinear optics date as far back as Raman [1] who noted color shifts in light as it passed through various liquids in 1928. In the 1960s, works by Bloembergen, Boyd and Kleinman outlined the necessary semi-classical electromagnetic theory that would cover many of the important nonlinear optical interactions that are widely used today.[2, 3] An important quantity for these nonlinear interactions is a phase velocity mismatch term which represents the difference in the phase velocities of the nonlinear output and its generating nonlinear polarization. This phasemismatch is usually non-zero due to material dispersion. Thus, for efficient nonlinear optical interactions, it is clear that a method of compensating for this phase velocity mismatch (or phasematching) must be employed since long crystals are required due to the small magnitude of the nonlinear coefficients.

There are two common methods of phasematching in nonlinear optical interactions: birefringent phasematching (BPM)[4] and quasi-phasematching (QPM)[2, 5]. In both cases, the nonlinear optical material is carefully selected for its engineerable properties and the polarizations and peak intensities of the interacting optical waves are chosen for efficient interactions. Although QPM was invented before BPM, the technical challenges in fabricating crystals with micron-scale features prevented its

practical development until the late 1980s. Though BPM has been very well developed and has shown to be practical in a wide variety of commercial applications, QPM provides some significant advantages over BPM. In particular, QPM allows nonlinear interactions where all the waves are polarized along the same axis. For many materials, these interactions utilize the largest nonlinear coefficient and can be two orders of magnitude more efficient than their birefringently phasematched counterparts. Since most QPM materials require lithographic techniques to fabricate the structures for phasematching, they can be engineered to be spatially inhomogeneous for use in a wide variety of applications, such as enhanced tunability[6, 7] and temporal pulse compression and shaping.[8]

Despite all the success of QPM materials in the research environment, QPM materials have had limited success in commercial settings. Practical applications for QPM materials have been limited to niche roles in the near-infrared radiation or for low-power visible light. The key factor limiting commercial application is that many QPM materials suffer from photorefractive damage which then requires operation at elevated ($\sim 150^\circ\text{C}$) temperatures which are, in general, higher than desirable. To extend the practical application of these materials requires development of improved materials that can support several watts of visible light near room temperature.[9]

1.2 Periodically poled materials

Quasi-phasematching can be realized by several methods. Periodic poling of ferroelectrics is perhaps the most common of all of these methods, however, it is worth noting the successes of both patterned semiconductors [10] and periodically poled quartz [11]. As early as 1964, multidomain ferroelectrics had been recognized to enhance the efficiency of nonlinear interactions.[12] Efforts to control the ferroelectric domain structure by modulation of crystal growth conditions allowed the demonstration of quasi-phasematched interactions.[13, 14] However, these techniques were limited by the lack of long range period control. In the late 1980's, lithographic techniques developed for the semiconductor processing industry enabled several techniques for periodic

poling (PP) of ferroelectrics with micron-scale precision over centimeter lengths. Indiffusion of dopants[15] and ion exchange [16] were the earliest of these techniques, however, due to the limited depth of the domain reversal, only waveguide devices could take advantage of the patterned region. With the development of electric-field poling,[17, 18] millimeter-thick ferroelectrics could be periodically poled and thus enable both waveguide and bulk QPM interactions. For the most part, electric-field poling techniques have supplanted the ion-exchange techniques for waveguide QPM applications.

Of all the available ferroelectrics, lithium niobate (LiNbO_3 , LN) has widely used because of its high nonlinearity, and the availability of high optical quality substrates. Because of its favorable piezoelectric qualities, LN is widely used in surface acoustic wave (SAW) applications and is available in a wide array of crystal orientations.[19] Furthermore, the high demand for these SAW devices has enabled the development of large (4-inch-diameter) crystals. Unfortunately, SAW applications do not require the stringent purity requirements of nonlinear optics applications and many LN manufacturers do not produce optical quality LN in significant quantity. However, by leveraging the technological advancements of producing high quality SAW-grade LN, optical-grade LN, developed for integrated-optics applications, has become relatively inexpensive in comparison to other birefringently phasematched materials.

Due to favorable properties for Czochralski growth, the common composition of commercially available LN is the congruently melting composition.[20] This congruently melting composition is the composition where the liquid and solid phases are in equilibrium. These congruently melting composition crystals are limited in applications involving visible light by photorefractive (PR) effects (light-induced index changes) [21] and by photochromic effects (light-induced absorption changes), e.g. green-induced infrared absorption (GRIIRA)[22]. Recently, studies of the mechanisms responsible for these effects suggest that the material limitations arise from native defects in the congruently melting crystals, which are $\sim 1.5\%$ lithium deficient. By reducing the concentration of the native defects, the use of magnesium-oxide doping has been shown to be quite effective at reducing both the photorefractive and photochromic effects.[23] Near-stoichiometric LN has also been investigated but has not

shown the same reduction in photorefractive damage and photochromism without the addition of a small concentration of magnesium oxide.[24, 25]

Although LN has been widely used, lithium tantalate (LiTaO_3 , LT), an isomorph of LN, has also been quite popular. The nonlinear coefficient (d_{33}) of LT is 13.8 pm/V, slightly smaller than LN, which has a nonlinear coefficient of 25.2 pm/V, but is still large compared to birefringently phasematched materials.[26] LT is also available in large (3-inch-diameter) wafers, with a wide array of crystal orientations and is grown in the congruently melting composition. This composition is also lithium deficient and carries similar native defects that are correlated with photorefractive and photochromic effects. For practical applications, melt-grown near-stoichiometric crystals with and without magnesium-doping have been shown to be less susceptible to photorefractive damage (PRD) and GRIIRA[27, 21] and are viable candidates for efficient frequency conversion.[9, 28]

Techniques that produce near-stoichiometric crystals from a melt are technically challenging.[29] In particular, they require precise control of temperature, temperature gradients and material feed rates. The vapor-transport-equilibration (VTE) method provides an alternative to direct melt-growth techniques to produce crystals of various compositions including near-stoichiometric crystals.[30] Near-stoichiometric crystals have been shown to have dramatically reduced intrinsic defect concentrations, have reduced susceptibility to PRD[31], and have enabled demonstration of efficient and stable frequency conversion at high average and high peak powers at near room temperature.[32] The advantage of the VTE method is the simplicity and reduced sensitivity to process parameters.

1.3 Nonlinear Optics

The principles behind nonlinear optics are well known and well explained in a multitude of references.[2] To orient the reader, a brief discussion of the important material characteristics for efficient QPM frequency conversion is required. This discussion will be limited to interactions that involve the second-order nonlinear susceptibility, $\chi^{(2)}$.

Electromagnetic radiation at optical frequencies induces an electric polarization in

a dielectric medium. The direction and magnitude of the polarization are dependent on the magnitude, the direction of propagation and the direction of polarization of the electric field inside the medium. The polarization \mathbf{P} can then be described as a power series in the applied electric field \mathbf{E} .

$$\mathbf{P} = \epsilon_0 \left(\chi^{(1)} \mathbf{E} + \chi^{(2)} \mathbf{E}^2 + \chi^{(3)} \mathbf{E}^3 \dots \right) \quad (1.1)$$

where $\chi^{(j)}$ represents the j th-order polarizability tensor. The first-order term is well known from linear electromagnetics and is responsible for refraction, dispersion, and diffraction. The higher order terms of this equation represent terms which can generate new frequencies. As stated earlier, we will limit our discussion to the second-order nonlinear susceptibility $\chi^{(2)}$. If we assume an applied electric field of a single frequency such that $\mathbf{E} = E \cos(\omega t)$, the polarization has the form of:

$$\begin{aligned} \mathbf{P} &= \epsilon_0 d \mathbf{E}^2 \\ &= 2\epsilon_0 d (E \cos(\omega t))^2 \\ &= 2\epsilon_0 d E^2 \cos^2(\omega t) \\ &= d\epsilon_0 E^2 (1 + \cos(2\omega t)) \end{aligned} \quad (1.2)$$

where $d = \frac{\chi^{(2)}}{2}$ is the effective nonlinear coefficient, which is obtained from the tensor $\chi^{(2)}$ by projection onto the polarization vectors of the fundamental and generated waves. We use d rather than $\chi^{(2)}$ in the remainder of this dissertation as it is more common in the experimental literature. The resultant polarization shown in Equation 1.2 has two components that do not oscillate at the frequency of the applied electric field. These components serve as driving terms when inserted into Maxwell's equations, the DC term driving optical rectification and the 2ω term driving second harmonic generation. Note that the nonlinear coefficient d for the 2ω term is not strictly the same as the nonlinear coefficient for the DC term but we have neglected the difference for mathematical convenience.

1.3.1 Slowly Varying Envelope Approximation

Beginning with a source-free Helmholtz wave equation (Equation 1.3), we can find the necessary parameters for efficient nonlinear conversion. Before we get to second harmonic generation we will need one more important step and that is to develop the slowly varying envelope approximation. Maxwell's equations in a homogenous source-free medium can be easily cast into the form.

$$\nabla^2 \mathbf{E} = \mu \frac{\partial^2 \mathbf{D}}{\partial t^2} \quad (1.3)$$

Here, \mathbf{E} and \mathbf{D} are the usual electric field and displacement (electric-flux density) including complete space and time dependence. With the definition of the displacement vector \mathbf{D} in terms of the polarization \mathbf{P} and the applied electric field \mathbf{E} , and using the constitutive relation in Equation 1.1, Equation 1.3 becomes

$$\nabla^2 \mathbf{E} = \mu \epsilon_0 (1 + \chi^{(1)}) \frac{\partial^2 \mathbf{E}}{\partial t^2} + 2\mu \epsilon_0 d \frac{\partial^2 \mathbf{E}^2}{\partial t^2} + \dots \quad (1.4)$$

For interactions where the amplitudes of the fields change slowly on the time scale of the wavelength in space and the optical period in time, one can invoke the Slowly Varying Envelope Approximation (SVEA) which simplifies our results by factoring out a plane-wave with the carrier frequencies ω_0 and $k_0 = \omega_0 c_0 n$, where c_0 is the speed of light and n is the refractive index of the medium at ω_0 , and leaving the slowly varying envelope of the electric field $\hat{\mathbf{E}}$. We relate the envelope to the complete field by

$$\mathbf{E}(x, y, z, t) = \frac{\hat{\mathbf{E}}(x, y, z, t)}{2} \exp(-i(\omega_0 t - k_0 z)) + c.c. \quad (1.5)$$

Here *c.c.* indicates the complex conjugate of the previous terms, and we assume, without loss of generality, propagation along the z-axis. Substituting into Equation

1.4 and using the approximations $\omega_0^2 \gg \omega_0 \frac{\partial}{\partial t} \gg \frac{\partial^2}{\partial t^2}$ and $k_0^2 \gg k_0 \frac{\partial}{\partial z} \gg \frac{\partial^2}{\partial z^2}$, and neglecting diffraction, loss, dispersion, group velocity mismatch and Poynting vector walkoff, we obtain

$$2ik_0 \frac{\partial \hat{\mathbf{E}}}{\partial z} = \mu\epsilon_0 \omega_0^2 \hat{\mathbf{P}}_{\text{NL}} \quad (1.6)$$

Equation 1.6 collects all the nonlinear polarization source terms into one vector $\hat{\mathbf{P}}_{\text{NL}}$ which describes the generating polarization at the appropriate temporal frequency ω_0 .

1.3.2 Second Harmonic Generation and the Coupled Mode Equations

Equation 1.6 is the basis for analyzing the important parameters for the nonlinear interactions explored later in this work. In particular, let us examine the case where there are two specific frequencies of interest ω_1 and ω_2 . We assume that the two frequencies are simply co-propagating plane waves, i.e.

$$\begin{aligned} \mathbf{E}_1 &= \frac{E_1}{2} \exp(-i(\omega_1 t - k_1 z)) + c.c. \\ \mathbf{E}_2 &= \frac{E_2}{2} \exp(-i(\omega_2 t - k_2 z)) + c.c. \\ \mathbf{E}_{\text{Total}} &= \mathbf{E}_1 + \mathbf{E}_2 \end{aligned}$$

The generated polarization will then be a power series of $\mathbf{E}_{\text{Total}}$ and thus all the polarization will be composed of all the possible combinations of \mathbf{E}_1 and \mathbf{E}_2 . The nonlinear polarization is given by

$$\begin{aligned} \mathbf{P}_{\text{NL}} &\approx 2d \mathbf{E}_{\text{Total}}^2 \\ &= \frac{1}{2} [d_{\text{SHG}} E_1^2 \exp(-2i(\omega_1 t - k_1 z)) + d_{\text{OR}} E_1^2 + d_{\text{SHG}} E_2^2 \exp(-2i(\omega_2 t - k_2 z)) + d_{\text{OR}} E_2^2] \end{aligned}$$

$$\begin{aligned}
& +d_{\text{DFG}}E_1E_2^* \exp(-i((\omega_1 - \omega_2)t - (k_1 - k_2)z)) \\
& +d_{\text{SFG}}E_1E_2 \exp(-i((\omega_1 + \omega_2)t - (k_1 + k_2)z)) + c.c.].
\end{aligned} \tag{1.7}$$

From this form of the nonlinear polarization we can see that there are several generated frequencies, $2\omega_1$, $2\omega_2$, $\omega_1 + \omega_2$, $\omega_1 - \omega_2$ and two zero frequency or DC terms, where we have introduced different nonlinear coefficients for the different nonlinear susceptibilities to account for dispersion in the nonlinear response, and for factors of two arising in counting the terms in the expansion of the products of fields. These are the basis for sum frequency generation (SFG), difference frequency generation (DFG), second harmonic generation (SHG) and optical rectification (OR). In this section we will examine SHG, which is the special case where $\omega_2 = 2\omega_1$. In this situation, the nonlinear polarization is given by

$$\begin{aligned}
\mathbf{P}_{\text{NL}} = & \frac{d}{2} [E_1^2 \exp(-i(\omega_2 t - 2k_1 z)) \\
& + 2E_1^* E_2 \exp(-i(\omega_1 t - (k_2 - k_1)z)) + c.c.]
\end{aligned} \tag{1.8}$$

where we have taken $d = d_{\text{SHG}}$. From this nonlinear polarization, two important coupled differential equations can be written that describe the evolution of the fundamental and second harmonic waves when Equation 1.8 is substituted into Equation 1.6.

$$\frac{\partial E_2}{\partial z} = -i \frac{\omega_2 d}{2c_0 n_2} E_1^2 \exp(i\Delta k z) \tag{1.9}$$

$$\frac{\partial E_1}{\partial z} = -i \frac{\omega_1 d}{2c_0 n_1} E_1^* E_2 \exp(i\Delta k z) \tag{1.10}$$

where we have introduced $\Delta k = k_2 - 2k_1$ which represents the phase mismatch of the material at the two different wavelengths. These two equations are the coupled mode equations for SHG where n_1 and n_2 are the refractive index of the two frequencies in the medium.

If we approximate the nonlinear interaction in the low conversion efficiency limit,

we can assume that the electric field of the fundamental does not change ($\frac{\partial E_1}{\partial z} = 0$). This approximation is accurate up to conversion efficiencies of $\sim 25\%$. Thus, we can take Equation 1.9 and integrate with respect to z from 0 to L yielding

$$E_2(L) - E_2(0) = -i \frac{\omega_2 d}{2c_0 n_2} E_1^2 \frac{\exp(i\Delta k L) - 1}{i\Delta k} \quad (1.11)$$

$$= -iGL \exp\left(i\frac{\Delta k L}{2}\right) E_1^2 \text{sinc}\left(\frac{\Delta k L}{2}\right) \quad (1.12)$$

where $G = (\omega_2 d)/(2c_0 n_2)$. It can be seen that the function reaches its maximum when $\Delta k = 0$, i.e. when the two waves are perfectly phasematched. In the case where $E_2(0) = 0$, we can define a conversion efficiency (the ratio of the second harmonic intensity $I_2 = c_0 \epsilon_0 n_2 |E_2|^2/2$ to the first harmonic intensity $I_1 = c_0 \epsilon_0 n_1 |E_1|^2/2$) intensity by

$$\begin{aligned} \eta &= \frac{I_2(L)}{I_1(0)} \\ &= \eta_{\text{nor}} I_1 L^2 \text{sinc}^2\left(\frac{\Delta k L}{2}\right) \end{aligned} \quad (1.13)$$

In the conversion efficiency relation (Equation 1.13), $\eta_{\text{nor}} = (2\omega_1^2 d^2)/(n_1^2 n_2 c_0^3 \epsilon_0)$ is the normalized conversion efficiency with units of $(\text{Watts})^{-1}$. It is then easy to see the few important parameters for plane-wave SHG. The conversion efficiency is proportional to the intensity of the pump, the normalized efficiency and the square of the length of the medium. Finally, the conversion efficiency is strongly dependent on the phase mismatch Δk and crystal length. The best way to illustrate the effect these two parameters is to examine Figures 1.1 and 1.2. Figure 1.1 shows the conversion efficiency as a function of total phase mismatch, $\frac{\Delta k L}{2}$. The sinc^2 shape defines how close to perfect phasematching is required for efficient SHG to occur.

As an example, with a one-centimeter-long device at a fundamental wavelength of $1 \mu\text{m}$, to be within the zeroes of the main lobe of the sinc^2 shape, the index difference ($n_2 - n_1$) must be less than $\pm 0.5 \times 10^{-4}$. If phasematching is not achieved,

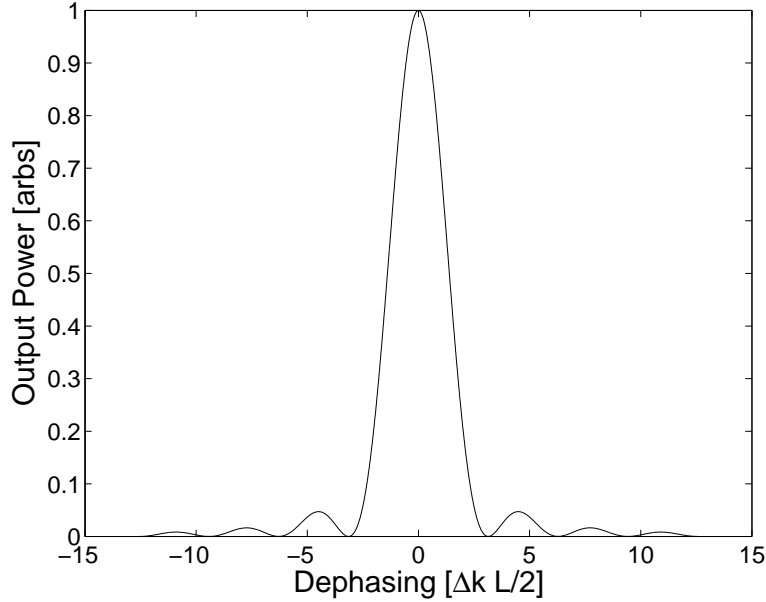


Figure 1.1: SHG conversion efficiency as a function of total phase mismatch $\frac{\Delta k L}{2}$. It illustrates the sinc^2 dependence of the conversion efficiency.

the efficiency will oscillate along the length of the device. This results from the oscillation of the relative phase between the driving nonlinear polarization and the generated second harmonic, which causes the direction of power flow to change periodically. This oscillation is illustrated as the non-phased curve in Figure 1.2. A critical length, the coherence length $L_c = \frac{\pi}{\Delta k}$, is the length over which the driving nonlinear polarization and the generated second harmonic stay in a phase relationship where the power flows from the driving nonlinear polarization to the second harmonic. To achieve the phasematching required, either birefringent phasematching or quasi-phasematching techniques must be employed. In birefringent phasematching, phasematching is achieved by choosing the correct polarization and propagation direction where the phase velocity of the second harmonic is equal to that of the fundamental. In this case, the conversion efficiency follows a quadratic growth as a function of length and is illustrated in Figure 1.2.

Alternatively, quasi-phasematching allows some phase slip between the driving nonlinear polarization and the generated second harmonic, however, just as the phase

difference reaches π (and hence will start to reverse power flow) the sign of the nonlinear coefficient is reversed to retain monotonic power flow from the driving nonlinear polarization to the second harmonic. In this case, we allow for a spatially varying nonlinear coefficient, $d(z)$ and insert this into Equation 1.9 in place of the constant d .

$$\frac{\partial E_2}{\partial z} = -i \frac{\omega_2 d(z)}{2c_0 n_2} E_1^2 \exp(i\Delta k z) \quad (1.14)$$

Integrating Equation 1.14 from $z = 0$ to $z = L$ gives

$$E_2(L) - E_2(0) = -i \frac{\omega_2}{2c_0 n_2} E_1^2 \int_0^L d(z') \exp(i\Delta k z') dz' \quad (1.15)$$

where we again assume an undepleted pump so that the amplitude of the fundamental field can be taken as constant. Here the integral in this equation is simply taken as the Fourier transform of the spatially varying nonlinear coefficient $d(z)$ evaluated at a spatial frequency of Δk . In all periodically poled QPM materials, only the sign and not the amplitude of the nonlinear coefficient is modulated so that the spatial function which maximizes the Fourier component at Δk is a square wave with spatial period $\Lambda = 2L_c = 2\pi/\Delta k$. If we assume that the first Fourier component of such a square wave is much closer to phasematching, i.e. $2\pi/\Lambda \approx \Delta k$, and neglect the contribution of the other Fourier components, Equation 1.14 becomes

$$E_2(L) - E_2(0) = -i \frac{2}{\pi} \frac{\omega_2 d}{2c_0 n_2} E_1^2 \exp\left(i \left(\Delta k - \frac{2\pi}{\Lambda}\right) z\right) \quad (1.16)$$

where the $2/\pi$ comes from the fundamental Fourier coefficient of the square wave. A QPM interaction involving a modulation of nonlinear coefficient with a period of Λ is called a first-order QPM interaction. Interactions involving higher Fourier components of the modulation, i.e. with period Λ/m , may also have non-zero Fourier components which become dominant when $2\pi m/\Lambda \approx \Delta k$ and thus are denoted as

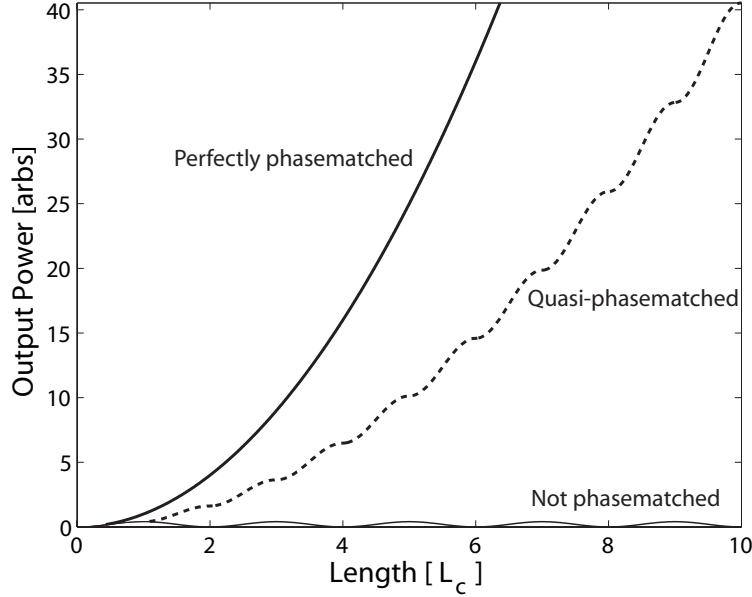


Figure 1.2: Second harmonic conversion efficiency as a function of length for various phasematching conditions: perfectly phasematched ($\Delta k = 0$), not phasematched and first-order quasi-phasematched.

higher order QPM, i.e. second-order QPM denotes $m = 2$, third-order QPM denotes $m = 3$. Note Equation 1.16 looks exactly like Equation 1.9 and thus the conversion efficiency for a QPM interaction becomes

$$\begin{aligned} \eta_{\text{QPM}} &= \frac{I_2(L)}{I_1(0)} \\ &= \eta_{\text{nor,QPM}} I_1 L^2 \text{sinc}^2 \left(\frac{\Delta k' L}{2} \right) \end{aligned} \quad (1.17)$$

Here $\eta_{\text{nor,QPM}} = (2\omega_1^2 d_{\text{eff}}^2) / (n_1^2 n_2 c_0^3 \epsilon_0)$ is the normalized conversion efficiency with units of $(\text{Watts})^{-1}$, $d_{\text{eff}} = 2d / (m\pi)$ is the effective nonlinear coefficient and $\Delta k' = \Delta k - 2\pi m / \Lambda$. Since the higher Fourier components contribute to the small scale variations in the generated field (though not to the average over significant distances), the conversion efficiency has its average quadratic growth (as described by Equation 1.17) modulated by ripples on the scale of a coherence length, as shown in Figure 1.2.

Table 1.1: Nonlinear coefficients of some widely used nonlinear materials.

Material	Nonlinear coefficient	Phasematching method	Nonlinear Coefficient [pm/V] (SHG of 532 nm)
LiB ₃ O ₅ , LBO	d_{31}	BFM	0.85[33]
KH ₂ PO ₄ , KDP	d_{36}	BFM	0.39 [33]
BaB ₂ O ₄ , BBO	d_{22}	BFM	2.3 [33]
LiNbO ₃ , LN	d_{31}	BFM	4.3[33]
KTiOPO ₄ , KTP	d_{33}	QPM	14.6 [26]
LiNbO ₃ , LN	d_{33}	QPM	25.2 [26]
LiTaO ₃ , LT	d_{33}	QPM	13.8 [26]

Although quasi-phasematching, as depicted in Figure 1.2, is less efficient than perfect phasematching (by a factor of $\frac{4}{\pi^2}$) for the same nonlinear coefficient, quasi-phasematching is often more efficient than the birefringent counterpart for several reasons:

Quasi-phasematching allows the use of the nonlinear coefficient that couples waves of the same polarization, often the largest of the nonlinear susceptibilities, which is unavailable to birefringent phasematching. This increase in nonlinear coefficient alone can easily increase the theoretical conversion by a factor of 50 or more, vastly surpassing the reduction of $\frac{4}{\pi^2}$. A comparison of several nonlinear coefficients of various nonlinear materials for birefringent and quasi-phasematched devices is compiled in Table 1.1. Quasi-phasematching always allows non-critically phasematched interactions, which often cannot be birefringently phasematched for the interactions of interest. The effective interaction length of critically phasematched interactions in birefringently phasematched devices is usually limited by Poynting vector walk-off. This limitation is eliminated in a non-critically phasematched interaction. QPM can sometimes provide a phasematching option when no birefringence (such as in III-V semiconductor materials such as gallium arsenide (GaAs)) or when not enough birefringence exists for the desired interaction (as in LT). Finally, QPM can provide a level of engineerability through the use of spatially inhomogeneous gratings. As previously stated, these devices can be particularly useful to provide multifunctionality,[6] tunability,[7] and temporal pulse shaping.[8]

Fabrication errors in QPM gratings can significantly reduce the nonlinear efficiency. Two types of fabrication errors are quite common in lithographically controlled poling processes, duty-cycle error and missing reversals (i.e. areas of the grating that do not have the appropriate sign of nonlinearity).

It has been shown in Equation 1.17 that the second harmonic will grow quadratically in a quasi-phasesmatching grating with a period Λ . The maximum growth rate for this process will occur if the grating has a 50 % duty cycle, i.e. the reversal occurs at exactly L_c . [34] If, however, the duty cycle is not 50 %, the second harmonic will still grow quadratically but at a reduced rate, proportional to the Fourier component of the modulation of the nonlinear susceptibility at the spatial frequency required for QPM, as seen in Equation 1.15. We define a value D_{grating} as the ratio of the length of reversed domain to the quasi-phasesmatching grating period (i.e. $D_{\text{grating}}=0.5$ for 50 % duty cycle). The efficiency for first-order QPM [34] is then given by

$$\eta = \eta_{\text{nor}} I_1 L^2 \text{sinc}^2 \left(\frac{\Delta k' L}{2} \right) \sin^2 (\pi D_{\text{grating}}) \quad (1.18)$$

i.e. the effective nonlinearity becomes $d_{\text{eff}} = (2d/\pi) \sin(\pi D_{\text{grating}})$. If there are missing reversals, the efficiency is no longer perfectly sinc^2 in shape as a function of the phase mismatch. The peak efficiency in the case is reduced by a factor of $(1 - 2f)^2$ where f is the fraction of reversals that are missing. [34]

Although the quadratic growth in conversion efficiency as a function length that is obtained under the undepleted pump approximation is appropriate in many situations, in other practical cases it is important to understand the regime of moderate to high efficiency. A full examination of the plane-wave, depleted pump regime of SHG is covered in Ref [2] and the result for the efficiency is given by

$$\eta_{\text{depleted}} = \eta_m \text{sn} \left(\sqrt{\frac{\eta_0}{\eta_m}}, \eta_m^2 \right) \quad (1.19)$$

where $\text{sn}(u, m)$ is the Jacobi elliptic integral of the first-kind defined in Equation 1.20, $\eta_0 = \eta_{\text{nor}} I_1 L^2$, $\eta_m = 1 + \delta^2 / 2\eta_0 - \sqrt{(1 + \delta^2 / 2\eta_0)^2 - 1}$ and $\delta = \frac{\Delta k L}{2}$.

$$u = \int_0^{\text{sn}(u,m)} \frac{dy}{\sqrt{(1-y^2)(1-my^2)}} \quad (1.20)$$

An important case is perfect phasematching, where the efficiency reduces to

$$\eta_{\text{depleted}} = \tanh^2 \left(\sqrt{\eta_{\text{nor}} I_1 L^2} \right) \quad (1.21)$$

1.3.3 Interactions including focussing and diffraction

The previous discussion examined only plane-wave SHG interactions. In practical experiments involving bulk crystals, an appropriate choice of focussing conditions must be made. Although tighter focussing allows for higher peak intensities, these peak intensities are only achieved in a short interaction length. Loose focussing provides long interactions lengths but lower peak intensities. Boyd and Kleinman (Ref. [35]) covered the necessary formalism to assess the appropriate choice of focussing; the resulting conversion efficiency in the low conversion limit is given by

$$\eta_{\text{nor,focussed}} = \frac{16\pi^2 d_{\text{eff}}^2}{\lambda^3 n_1 n_2 c_0 \epsilon_0} \quad (1.22)$$

$$\begin{aligned} \eta &= \frac{P_2}{P_1} \\ &= \eta_{\text{nor,focussed}} P_1 L h \left(\alpha, B, \xi, \mu, \frac{\Delta k L_{\text{conf}}}{2} \right) \end{aligned} \quad (1.23)$$

Equation 1.22 is the normalized efficiency for a focussed interaction with units of %/(Watt-cm). Here d_{eff} is the effective nonlinear coefficient and λ is the fundamental wavelength. Equation 1.23 gives the total efficiency for a process using a focussed gaussian beam given a length L and input fundamental power P_1 . The value h is called the Boyd and Kleinman h -factor and is dependent on the absorptivity (α), the Poynting vector walk-off (B), the focussing parameter ($\xi = L/L_{\text{conf}}$, for a confocal length, $L_{\text{conf}} = 2\pi w^2 n_1 / \lambda$, with a focussed, $1/e^2$ -intensity radius of w), the focus position (μ) and the phase mismatch, $\Delta k L_{\text{conf}} / 2$. Perhaps the most important

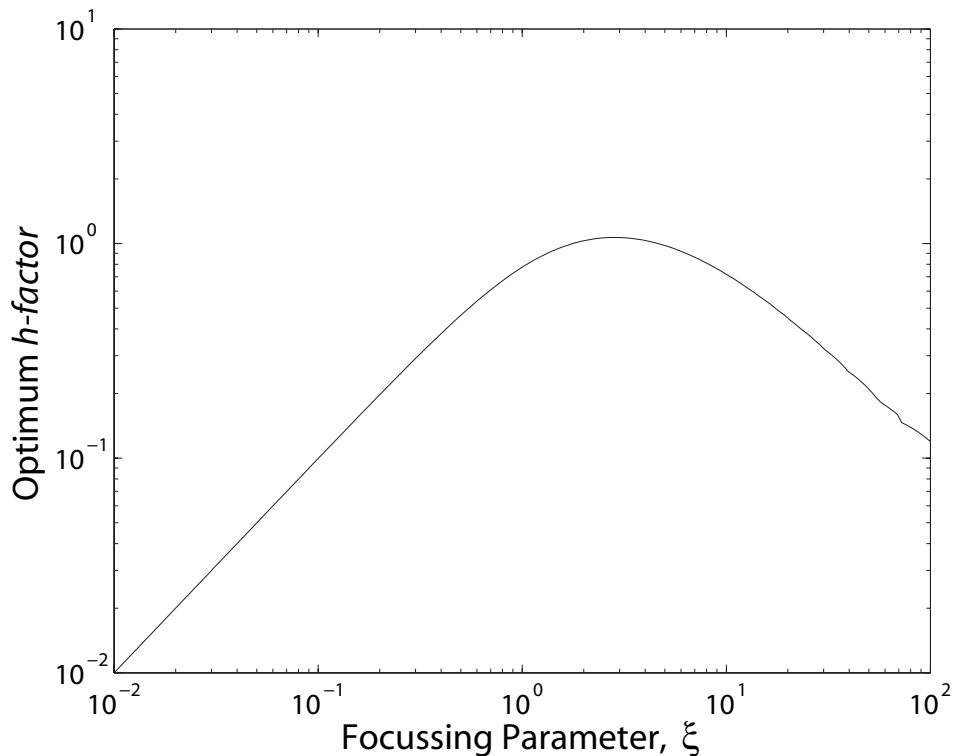


Figure 1.3: Optimized h -factor values for various focussing parameters assuming absorption, Poynting vector walk-off and focus position mismatch are all zero.[35]

parameter in QPM experiments is the focussing parameter which is the ratio of the crystal length to the confocal length of the fundamental beam. For a given focussing parameter the h -factor is maximized by tuning the phase mismatch (often by adjusting temperature). A plot of optimal h -factor versus focussing parameter for the case where loss and Poynting-vector walkoff are negligible, and the focus is at the center of the crystal is shown in Ref. [35] and reproduced in Figure 1.3.

The maximum value of h is 1.07 and occurs at a focussing parameter of 2.84. It is often more convenient to use confocal focussing ($\xi = 1$) and, at this focus, the value of h is 0.78. Collected in Table 1.2 are several normalized efficiencies for SHG of 532-nm radiation of different nonlinear materials at $h = 1$.

Although these normalized focussed interaction efficiencies were originally derived with the undepleted-pump approximation, Ref. [36] tried to extend this to

Table 1.2: Normalized bulk efficiencies for SHG of 532-nm radiation of some commonly used nonlinear materials

Material	η_{nor} for $h = 1$ in $\% / (\text{watt-cm})$
LBO	0.006
KDP	0.001
BBO	0.044
PPKTP	1.8
PPLN	3.0
PPLT	1.1

the depleted-pump regime. Unfortunately, the equations did not allow for an analytical solution. However close to perfect phasematching, the conversion efficiency calculated by numerical simulation qualitatively followed the relation in Equation 1.24.

$$\eta_{\text{depleted,focussed}} = \tanh^2 \left(\sqrt{\eta_{\text{nor,focussed}} P_1 L h} \right) \quad (1.24)$$

1.3.4 Sum Frequency Generation

The method to derive the conversion efficiency for sum frequency generation (SFG) is similar to the SHG case. The sum frequency interaction involves the generation of a frequency, ω_3 , from two lower frequencies, ω_1 and ω_2 where $\omega_3 = \omega_1 + \omega_2$. The appropriate photon energy and momentum diagrams are illustrated in Figure 1.4. The phase mismatch is then defined as $\Delta k = k_3 - k_2 - k_1$.

For the plane-wave case, the output intensities for the undepleted situation are given in Equation 1.25.

$$I_{3,\text{undep}} = \eta_{\text{nor,SFG}} I_1 I_2 L^2 \quad (1.25)$$

where

$$\eta_{\text{nor,SFG}} = \frac{2\omega_1\omega_2 d_{\text{eff,SFG}}^2}{n_1 n_2} \quad (1.26)$$

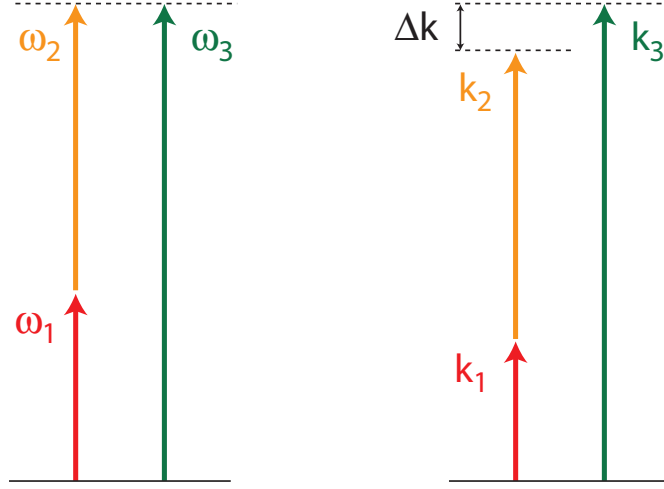


Figure 1.4: Energy and momentum conservation are required for efficient SFG.

For focussed gaussian beams, Ref. [37] extended the work of Boyd and Kleinman (Ref. [35]) to the sum frequency case and showed that in the low conversion limit the generated SFG power follows the relation

$$P_{3,\text{SFG}} = \eta_{\text{nor,bulk,SFG}} P_1 P_2 L h_{\text{SFG}} \left(K, \xi_1, \xi_2, \frac{\Delta k L}{2}, B \right) \quad (1.27)$$

where

$$\eta_{\text{nor,bulk,SFG}} = \frac{16\pi^2 d_{\text{eff,SFG}}^2}{\lambda_1 \lambda_2 \lambda_3 n_1 n_2 c_0 \epsilon_0} \quad (1.28)$$

$$d_{\text{eff,SFG}} = 2d_{\text{eff,SHG}} \quad (1.29)$$

$$(1.30)$$

Here there are two focussing parameters (ξ_1, ξ_2) and an important value $K = \frac{k_1}{k_2}$ that describes how similar the interacting wavevectors are. The function h is similar to the h -factor for SHG interactions. For cases where walkoff is negligible and phase-mismatch optimized, the h -factor is optimized for all values of K when the focussing parameters $\xi_1 = \xi_2 = 2.84$ just as in SHG.

1.4 Limitations on Nonlinear Devices

All nonlinear devices have limitations that prevent further improvement of device performance. Many of these limitations are material dependent and some of the characteristics that cause these limitations are unavoidable and inherent to the chosen nonlinear material. Effects like Poynting vector walk-off, group velocity mismatch, group velocity dispersion and pure two-photon absorption are intrinsic material characteristics that are in some ways unavoidable. With careful choice of experimental parameters or device topology, the effects of some of these characteristics can be minimized.

Other characteristics, which are often defect-related, can be mitigated by minimizing or eliminating the defects either during the initial material fabrication or by post-processing the material. A good summary of various defects in lithium niobate can be found in Ref. [38]. Unfortunately, the effects of the limitations caused by these defects do not usually have consequences that can be perfectly modeled. However, simple models allow us to estimate the realm of efficient frequency conversion available for a particular material. In many situations, these characteristics limit the performance of nonlinear devices well before any inherent limitations are apparent. Many of these characteristics are described as “optical damage” or “laser damage” without specifying the underlying cause. It is then extremely important to examine possible sources of “laser damage” to understand the true limitations imposed by these effects.

1.4.1 Photorefraction

In 1966, Ashkin et al.[39] observed optically-induced refractive index inhomogeneities in LT and LN. This light-induced index change has since been well studied and is more commonly known as photorefraction. These index changes either distort the wavefront of the laser beam or scatter optical radiation into various directions and are often referred to as “laser damage”. [19] Although these index changes may be undesirable in nonlinear optics applications, they can be used for optical data storage and a multitude of other applications.[40] However, for frequency conversion applications,

photorefractive prevents efficient conversion if not appropriately mitigated.

In 1969, Chen postulated that photorefractive arose from the redistribution of light-induced free carriers causing index changes (Δn) by the linear electro-optic effect (Equation 1.31) from the space-charge field E_{SC} . [41]

$$\Delta n = \frac{1}{2} r n^3 E_{SC} \quad (1.31)$$

Here r represents the electro-optic coefficient of the photorefractive material and n is the refractive index of the material. This simple model successfully explains photorefractive in various materials and experimental conditions.

Free carriers are a result of photoionization of deep levels. The transport properties of ferroelectrics are unusual in that there is a photogalvanic term in addition to the usual drift and diffusion term. Ref. [42] observed constant currents along the ferroelectric axis in LN when the sample was illuminated. This “bulk photovoltaic” effect is also known as the “photogalvanic” effect and results in a source term directed along the polar axis in the constitutive relation for current density

$$\mathbf{J} = \sigma \mathbf{E}_{SC} + \kappa I \hat{\mathbf{z}} \quad (1.32)$$

Here \mathbf{J} is the current density vector, σ is the conductivity (assumed isotropic), κ is the photogalvanic coefficient (though this is actually a tensor quantity [40], we retain in this simple model only the dominant term along $\hat{\mathbf{z}}$), I is the intensity of the light and $\hat{\mathbf{z}}$ is a unit vector along the polar axis. In this relation, we have neglected the diffusion term.

A crystal illuminated with a beam of light reaches steady state ($\mathbf{J} = 0$) when a space charge field builds up large enough to generate a current that balances the PG current, i.e. $E_{SC} \approx -\frac{\kappa}{\sigma} I$. This space charge field induces a change in the refractive index through the electro-optic effect, as given in Equation 1.31. These index inhomogeneities cause either reduced conversion efficiency because of dephasing or scattering and beam distortion which prevent useful laser output. In typical congruent lithium niobate and tantalate these space charge fields can reach values in excess

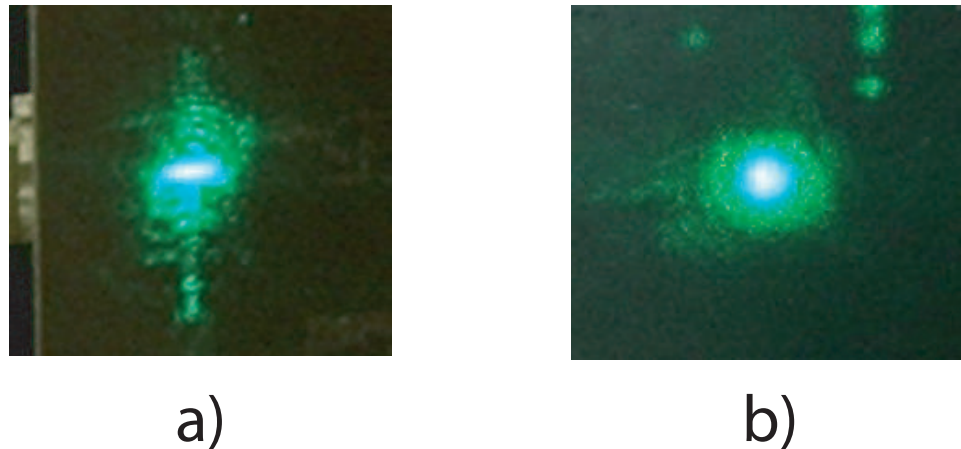


Figure 1.5: a) A typical photorefractive beam distortion in a LN when illuminated with visible light. b) A photorefractive-damage resistant LN shows no beam distortion even at a higher average power.

of 10 000 V/cm. The electro-optic coefficient of LN is close to 30 pm/V, and thus these space charge fields can easily cause enough scattering to render a 1-mm-long crystal useless. Moreover, the performance of nonlinear devices can degrade over time since these charges can accumulate due to the long dielectric lifetimes observed in LN (on the order of months in the dark). A typical one-dimensional beam distortion often associated with photorefraction in LN is illustrated in Figure 1.5.

To quantify the sensitivity of the index change of photorefractive materials to intensities at various wavelengths a few techniques have been used. Optical measurements [43] have been used to directly measure the refractive index change by holographic techniques and by measuring the amount polarization rotation. Charge transport measurements [44] that measure the underlying photogalvanic and photoconductive coefficients have also been used.

It has been shown that many defects, both impurities and native defects, alter photoconductivity and photogalvanism of photorefractive materials. In particular, magnesium doping [23] and stoichiometry control [45] have been shown to be effective at increasing the photoconductivity of both lithium tantalate and lithium niobate and thus reducing the susceptibility to photorefractive damage.

To examine the effect of stoichiometry control on photoconductivity more closely,

we will follow the formalism of Refs. [31], [40], and [44]. In their formalism, the conductivity is given by Equation 1.33.

$$\sigma = q\mu_e N_e \quad (1.33)$$

where q is the charge of an electron, μ_e is the mobility and N_e is the free-carrier density. In undoped lithium tantalate, one can model the rate of change of the free-carrier density with a two-band model,[46] as

$$\frac{dN_e}{dt} = N_{th} + S_{TaLi}IN_{TaLi} + S_{imp}IN_{imp} - r_{TaLi}N_{TaLi}N_e - r_{imp}N_{imp}N_e \quad (1.34)$$

where N_{TaLi} and N_{imp} are the densities of Ta anti-sites and other impurities, respectively, and S_i and r_i are the generation and recombination coefficients for those defects. The thermal generation rate is given by N_{th} . In steady state, the free-carrier density is given by

$$N_e = \frac{N_{th} + S_{TaLi}IN_{TaLi} + S_{imp}IN_{imp}}{r_{TaLi}N_{TaLi} + r_{imp}N_{imp}} \quad (1.35)$$

In congruent-composition lithium tantalate, the recombination rate is dominated by $r_{TaLi}N_{TaLi}$ and the generation coefficient for impurities is usually much greater than the generation coefficient for Ta anti-sites, $S_{imp} \gg S_{TaLi}$. [47, 48, 49] Since the density of Ta anti-sites is proportional to the deviation from stoichiometry, Δx , (i.e. $N_{TaLi} = A\Delta x$) we find that

$$N_e = \frac{N_{th} + \rho I \Delta x + \gamma I}{\nu \Delta x} \quad (1.36)$$

where $\rho = S_{TaLi}A$, $\gamma = S_{imp}N_{imp}$ and $\nu = r_{TaLi}A$. Substituting Equation 1.36 into Equations 1.32 and 1.31, we can then calculate the space charge field and the refractive index change to be

$$E_{\text{SC}} = -\frac{\kappa\nu I\Delta x}{q\mu(N_{th} + (\rho\Delta x + \gamma)I)} \quad (1.37)$$

$$\Delta n = -\frac{rn^3\kappa\nu I\Delta x}{2q\mu(N_{th} + (\rho\Delta x + \gamma)I)} \quad (1.38)$$

In LT, where $\rho\Delta x \ll \gamma$, for light intensities typical of many nonlinear optics applications, the space charge fields (and hence the light-induced index changes) can be drastically reduced by reducing the deviation from stoichiometry with techniques to produce near-stoichiometric crystals.

1.4.2 Laser-induced damage

Laser-induced bulk and surface damage are limitations on the usefulness of nonlinear optical materials. Laser-induced damage under various conditions is very dependent on crystal growth and preparation conditions. Damage thresholds vary spatially within apparently homogenous crystals, so the damage threshold is treated as a statistical quantity.[50, 51] The limitation they impose on current quasi-phaseshifted nonlinear devices is mainly an issue of minimum beam size for a given peak power (or equivalently a maximum peak power for a given aperture) and hence maximum nonlinear drive (here defined as the square root of the extrapolated low conversion efficiency, $\sqrt{\eta_0}$) available in a particular experiment.

1.4.3 Absorption

Both linear and nonlinear absorption are perhaps the ultimate limiting characteristics in a well engineered nonlinear device. There are many possible experimental outcomes that may limit the performance of nonlinear devices. The most common of these are: a) absorption of the input radiation or nonlinear output causing lower peak intensities and thus limiting effective interaction length, b) absorption causing thermal dephasing[52] (longitudinal or transverse, cumulative or single-shot) and thus reduced efficiency, c) thermal lensing[53] of the input radiation and the generated nonlinear

output causing either reduced efficiency or damage, and d) thermal stresses at cooling interfaces causing fracture of the nonlinear device.

For all of these experimental outcomes, the absorption is related to the concentrations of impurities and native defects. In ferroelectric oxides, the linear absorption is often dominated by concentrations of transition metal impurities incorporated into the crystal during growth either intentionally, e.g. iron-doped or chromium-doped LN, or unintentionally, e.g. iron impurities in LN.[54]

Many of the absorption bands in lithium niobate are often attributed to iron impurities. Thus, the effects of these iron impurities have been well studied by the photorefractive community. Kurz and Kratzig matched many of the UV, visible, and near-infrared absorption bands to Fe^{2+} and Fe^{3+} complexes.[55] Others have measured the cross-section of these two oxidation states.[54] Still others have looked at other transition metal impurities such as Cr^{2+} . [56] It is important to note, however, that the oxidation/reduction state of these impurities greatly affects the observed absorption in these crystals.

Photochromism

Other than extrinsic impurities, color centers can arise from native defects. While photorefractive is an optically-induced refractive index change, photochromism is an optically-induced absorption (or color change). The electronic state of native defects can be altered by the illumination with optical radiation. This change of electronic state can then alter the absorption spectra of the native defects.

A well-known and studied example is green-induced infrared absorption (GRIIRA) in LN and LT.[57] In these crystals, the infrared absorption can increase several times when illuminated with even small intensities of green light. This absorption change can occur on a time scale of 400 fs.[58] Figure 1.6 illustrates the change in absorption in LN with and without the presence of green light. The generally accepted model for this process is that the green light excites a Nb^{5+} atom sitting on a Li^+ site, a Nb anti-site ($\text{Nb}_{\text{Li}}^{4+}$), and photoionize it to a $\text{Nb}_{\text{Li}}^{5+}$ creating a small polaron.[58] This small polaron has absorption bands centered in the near-infrared (NIR) causing an enhanced absorption in the NIR. This effect can be reduced by eliminating the Nb

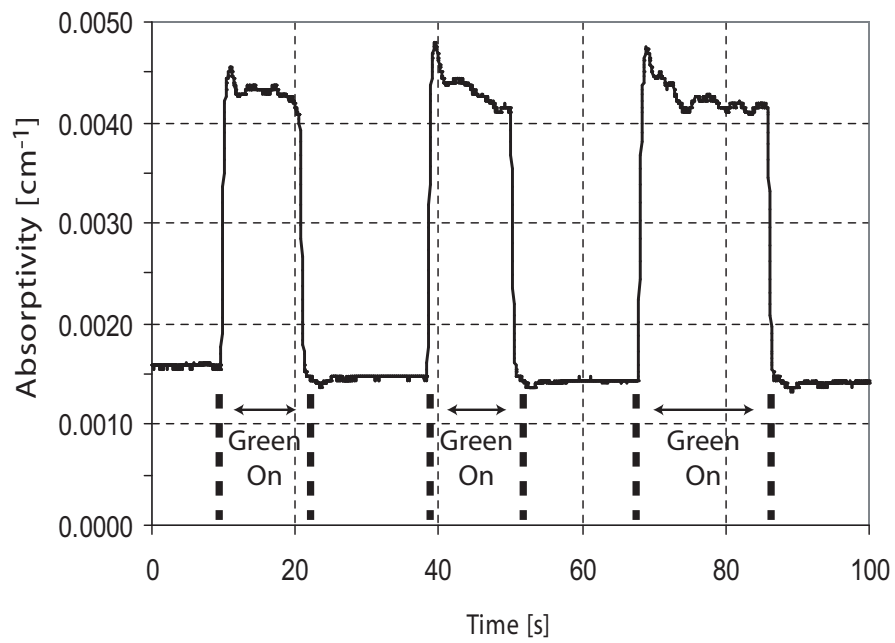


Figure 1.6: Absorption of 1064-nm radiation in lithium niobate as a function of time. At three separate instances, 514.5-nm radiation illuminates the same volume as the 1064-nm radiation and increases the absorption three-fold. The intensity of the 514.5-nm radiation used in this experiment was approximately 5 kW/cm^2 .

anti-sites which are created during the growth process. The situation in LT is the same with Nb anti-sites replaced by Ta anti-sites. By using similar methods which reduce photorefraction, namely magnesium doping and composition control, GRIIRA in LN (and LT) can be reduced.[22, 32]

Thermal Dephasing

Although absorption could cause enough heat to permanently damage the nonlinear device, in practical application, one would like to avoid this situation. In many cases, thermal dephasing[52] will limit the efficiency of the frequency conversion. Eimerl [52] examines the effect of thermal dephasing on efficient conversion for high nonlinear drive. In particular, he provides a contour plot of the SHG conversion efficiency (Equation 1.21) versus total dephasing, $\delta = \frac{\Delta k L}{2}$, and nonlinear drive, $\sqrt{\eta_0}$. Eimerl focusses his attention on birefringently phasematched materials and his contour plot extends to total dephasing close to 1.5 (because of Poynting vector walk-off) and nonlinear drives larger than 15. Fortunately, with quasi-phasematched materials, we can consider the efficient conversion region near perfect phasematching ($\delta \approx 0$) and nonlinear drives less than 3. This part of Eimerl's contour plot is reproduced in Figure 1.7.

This contour plot demonstrates the importance of phasematching bandwidth for efficient conversion. For efficient conversion, the total dephasing, the sum of all dephasing elements, must be less than $\pi/10$ for efficient conversion.[52] If one considers thermal dephasing alone, efficient conversion requires that Equation 1.39 be approximately satisfied.

$$\delta = \frac{d\Delta k}{dT}(\Delta T_{\text{long}} + \Delta T_{\text{trans}}) < \frac{\pi}{10} \quad (1.39)$$

Here ΔT_{long} is the longitudinal temperature difference and ΔT_{trans} is the transverse temperature difference.

For typical focussed nonlinear interactions where the heat is removed transverse to the propagation direction, we can calculate the temperature difference between the

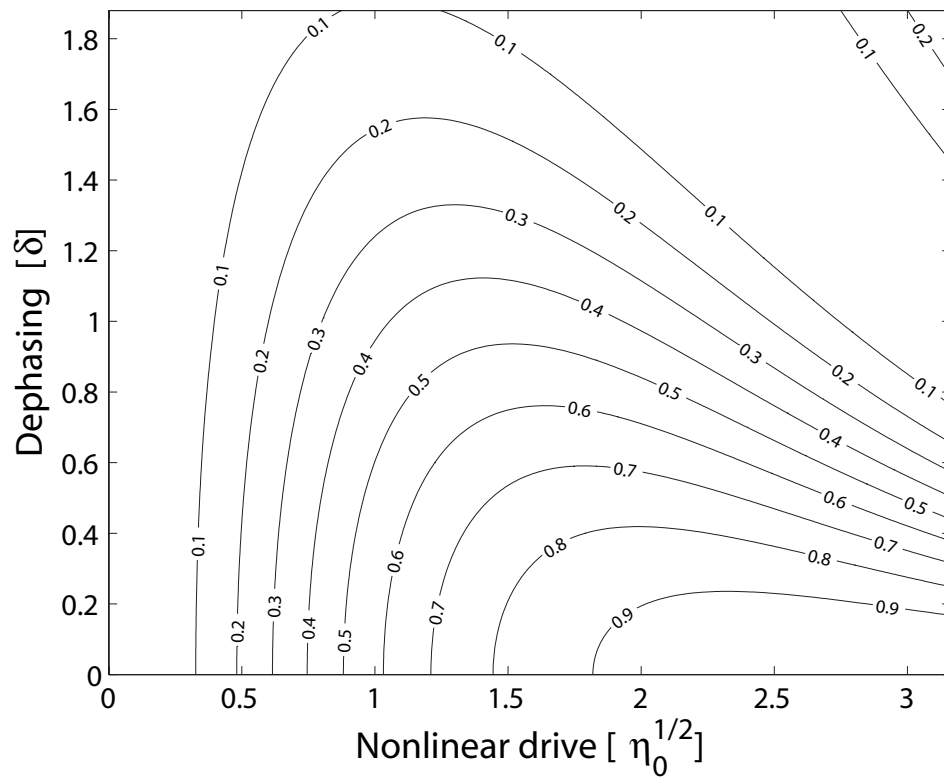


Figure 1.7: Contour plot of efficiency versus total dephasing and nonlinear drive. (Reproduced from Ref. [52]).

center and the edge of a cylindrical beam assuming an isotropic thermal conductivity. In this situation, the transverse temperature difference is given by

$$\Delta T_{\text{trans}} = \frac{\alpha P}{\pi \kappa_{th}} \quad (1.40)$$

Here κ_{th} is the thermal conductivity and αP represents the total absorbed power per unit length. A 1-cm-long lithium tantalate crystal used for generation of 532-nm radiation by SHG with a thermal conductivity of 4 W/(mK) and an absorptivity of 0.1 %/cm can handle approximately 70 W of incident laser power before thermal dephasing becomes important.

1.5 Overview

The goal of this dissertation is to characterize the practical applicability of near-stoichiometric lithium tantalate fabricated by vapor transport equilibration for frequency conversion. Additionally, the ability to estimate the boundaries of practical and efficient frequency conversion is of interest.

Detailed discussions on lithium tantalate, the vapor-transport-equilibration method, the process of crystal fabrication and equipment used to fabricate devices are presented in Chapter 2,.

Chapter 3 describes the measurement techniques and provides the measured data of ferroelectric, optical and thermal properties of the crystals fabricated.

Chapter 4 summarizes the nonlinear performance of traditional, z-cut, bulk, quasi-phasematched devices based on near-stoichiometric lithium tantalate. Specifically, the generation of watt-level 532-nm radiation, watt-level 589-nm radiation, and the demonstration of the SHG of 458.3-nm radiation are shown.

A topology for scaling to large-aperture devices is presented in Chapter 5. The motivation for large aperture devices is first discussed. The theory and experimental demonstration of scalable, large-aperture devices based on rotated-cut, near-stoichiometric lithium tantalate is shown.

Finally, Chapter 6 summarizes the work and provides future directions for research.

Chapter 2

Crystal fabrication

2.1 Vapor Transport Equilibration of Lithium Tantalate

As discussed in Chapter 1, near-stoichiometric lithium tantalate has shown great promise for practical applicability for efficient frequency conversion because of its improved resistance to photorefractive damage (PRD) and green-induced infrared absorption (GRIIRA) as the composition tends towards stoichiometry.[32] Crystals of lithium tantalate can exist in a wide range of compositions from approximately 47 mol % lithium-oxide to approximately 50 mol % lithium-oxide. In addition to the susceptibility to PRD and GRIIRA, many other physical properties of lithium tantalate depend strongly on crystal composition.[19] Properties such as ferroelectric coercive field, Curie temperature, birefringence, NMR and Raman spectra are dependent on composition. Most commercially available lithium tantalate is grown from melts of the congruently melting composition with 48.39 mol % lithium-oxide (Li_2O) by the Czochralski method. This process produces crystals of the same composition with a Curie temperature of 605.3 °C.[59] In comparison, crystals of near-stoichiometric composition, 49.95 mol % lithium-oxide (Li_2O) with a Curie temperature of 695 °C, are grown from melts with a substantial excess of lithium oxide (~ 58 mol %

lithium-oxide).[29] The defects associated with the lithium deficiency of the congruently melting composition are widely accepted to be one Ta^{4+} anti-site defect ($\text{Ta}_{\text{Li}^{5+}}^{5+}$)⁴⁺ plus an additional four lithium vacancies nearby which are required for charge neutrality.[60] The concentration of anti-site Ta^{4+} native defects closely correlates with the magnitude of PRD and GRIIRA[32] under the high optical intensities typical of frequency conversion applications. Defect studies by others have led to the polaron model for the Ta^{4+} defect which accounts reasonably well for an absorption band in congruent lithium tantalate, and it provides a plausible mechanism for carrier excitation and trapping and the resultant optical properties seen in this material.[61]

Due to the strong compositional dependence of PRD and GRIIRA, an accurate measure of the deviation from stoichiometry is essential for process development, process control and predicting device performance in this material. Recently, the ferroelectric coercive field of lithium tantalate has been shown to be a sensitive measure of crystal composition.[62] Previous measurements suggest that the ferroelectric coercive field is linearly proportional to the lithium deficiency, ranging from 21 kV/mm in congruently melting lithium tantalate (~ 1.61 mol % lithium deficient) to 0.1 kV/mm at a near-stoichiometric lithium tantalate (estimated to be ~ 0.008 mol % lithium deficient).[62]

Ferroelectricity in lithium tantalate was first described by Matthias and Remeika in 1949.[63] Early work in the growth of lithium tantalate characterized crystal composition by measuring the Curie temperature.[64, 65] In particular, Ballman et al. report Curie temperatures as high as 690 °C via growth from lithium-oxide-rich melts.[65] Measurements of the Curie temperature of ceramic samples suggest that the composition of crystals with that Curie temperature correspond to a composition in the range 49.9 mol % to 50.0 mol % Li_2O . These crystals were apparently the first near-stoichiometric lithium tantalate (SLT) crystals grown, but they suffered from significant inhomogeneity and poor yield. Thus, most manufacturers have chosen to grow congruently melting crystals which provide homogeneous crystals and result in extremely good yield.[59]

Recently, techniques such as the double-crucible, melt-replenishment Czochralski method have produced high-quality SLT crystals with Curie temperatures as high

as 695 °C and coercive fields as low as 800 V/mm.[60] These self-flux techniques require precise control of the temperature and material feed rates to ensure homogenous results. SLT produced in this manner has improved characteristics for frequency conversion applications, including reduced photorefraction[21], reduced susceptibility to GRIIRA[22], and improved thermal conductivity [28]. Measurements of ferroelectric coercive field suggest that these techniques have achieved compositions close to 49.95 mol % Li_2O .[60]

As an alternative to direct melt-growth methods, the VTE method can be used to convert commercially available, congruently grown crystals into crystals of a desired composition.[66] By heating the sample crystal with an appropriate composition of powder in a loosely sealed system, crystals of nearly any composition that falls within the single-phase LiTaO_3 existence region can be produced. In the case of lithium tantalate, Li_2O is exchanged between the single crystal and the powder by vapor transport until equilibrium is achieved. For low photorefractivity and GRIIRA, it is desirable to produce compositions that are very near to 50 mol % Li_2O , which lies close to the boundary of the single phase LiTaO_3 existence region, adjacent to the $\text{LiTaO}_3+\text{Li}_3\text{TaO}_4$, two-phase existence region. The vapor pressure of Li_2O for all compositions within the two-phase field is a function only of temperature and does not depend on the specific composition. Thus, powders within the two-phase region can serve as an “infinite” reservoir of Li_2O which can be used to bring the composition of crystals lying within the single phase existence region, as congruent composition crystals do, to the boundary of the single phase LiTaO_3 existence region which is very close to the stoichiometric composition. The resultant near-stoichiometric composition crystal is in phase equilibrium with the two-phase powder so that mass transport of Li_2O stops at this point without the formation of Li_3TaO_4 on the surface. This process is self-terminating. The approach to the stoichiometric composition can require extended processing at high temperatures. However, as long as the composition of the powder remains in the two-phase region, i.e. lithium-rich, this process results in a vapor-transport-equilibrated, near-stoichiometric lithium tantalate (VLT) crystal whose composition closely approaches the phase boundary of the single phase LiTaO_3 existence region. The speed of the process and final composition of the crystal depend

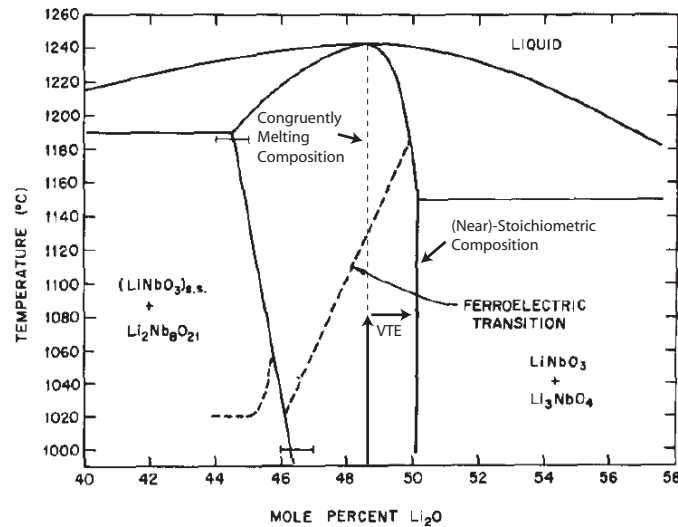


Figure 2.1: A phase diagram of lithium niobate and a depiction of how the VTE process transforms congruent-composition crystals into near-stoichiometric crystals.[67]

only on the temperature and duration of the VTE process and the thickness of the crystal. Using this method, coercive fields of as low as 100 V/mm have been achieved, which suggests that the crystal reached a composition of > 49.99 mol % Li₂O.[62]

Figure 2.1 shows how the VTE process transforms congruent-composition lithium niobate into near-stoichiometric lithium niobate. In a VTE crucible, a constant activity multi-phase (CAMP) powder and a congruent lithium niobate crystal are brought to an appropriate processing temperature to allow for significant evaporation of Li₂O from the CAMP powder and Li diffusivity in lithium niobate. This process continues until enough Li₂O has been exchanged and Li has had adequate time to diffuse through the crystal. Although the phase diagram taken from Ref. [67] shown is for lithium niobate, the phase diagram and VTE process is similar for lithium tantalate. A phase diagram for lithium tantalate is not shown because of difficulties of accurately measuring phase equilibria have prevented its accurate characterization.[19] It is important to note that the final composition of the VTE process crystal is dependent on the VTE process temperature and time.

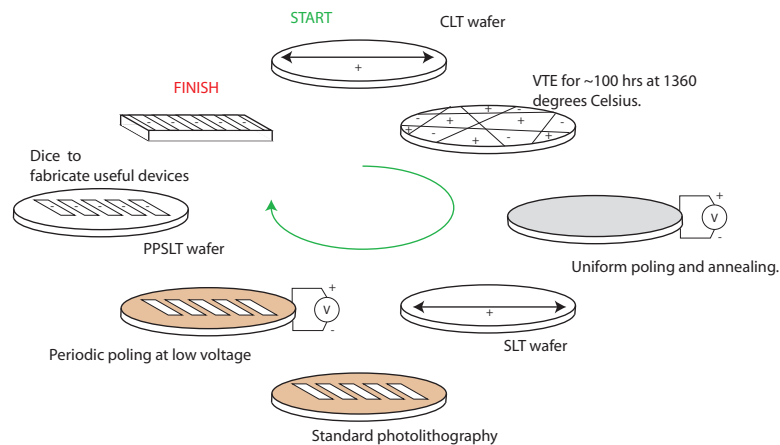


Figure 2.2: Process flow chart to fabricate VTE'd, periodically poled devices.

2.2 Experimental Apparatus for VTE

Optical-grade, z-cut, congruent lithium tantalate wafers from Yamaju Ceramics, Inc were used as the substrate for our VTE experiments. Full 2", one-quarter and one-sixth wafers with thicknesses of 0.5 mm and 1 mm were processed. A process flow chart (Figure 2.2) illustrates all the steps required to fabricate periodically poled devices.

A pre-reacted mixture of Li_2O (60 mol %) and Ta_2O_5 (40 mol %) powder was produced from appropriate amounts of Li_2CO_3 and Ta_2O_5 to form a two-phase mixture of LiTaO_3 and Li_3TaO_4 which served as the source of Li_2O for the VTE process. The congruent-composition wafers were placed in a platinum crucible, standing vertically in a simple platinum wafer holder. A second platinum crucible with a slightly smaller diameter than the first was then placed over the wafer assembly with the rim resting on the pre-sintered powder. The crucible arrangement is shown in Figure 2.3 The size of the cover crucible was chosen to minimize the area of the pre-synthesized powder that was exposed to the air. Since Li_2O is slowly volatilized during the VTE process and lost to the environment the use of a large cover is thought to provide a loose seal by which the vapor pressure of Li_2O can be controlled by the Li_2O equilibrium partial pressure over the two-phase powder. The entire assembly was then heated in a two temperature process, first to 1360 °C and then 1100 °C in a tube furnace

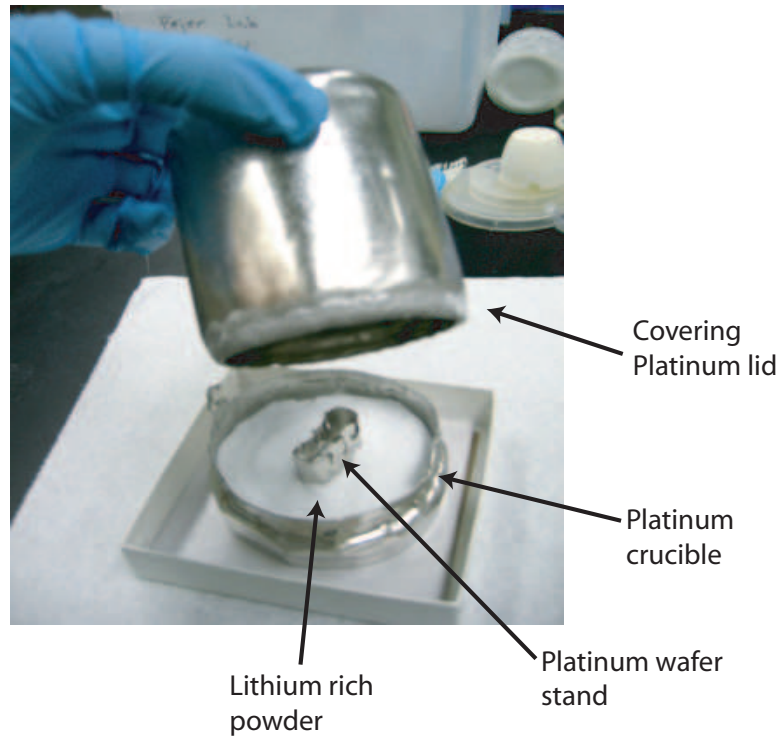


Figure 2.3: Photograph of crucible, cover, two-phase powder and platinum foil vertical stand.

purged with dry nitrogen, but not carefully sealed, for various lengths of time. After processing, the crucible and the wafers were weighed to determine Li_2O loss and the powder was replaced when the excess Li_2O was depleted, as determined by the weight loss measurements.

Since the VTE process is carried out above the Curie temperature, the VLT crystals had to be uniformly poled before reproducible periodic poling was possible. The uniform poling process was performed at $185\text{ }^\circ\text{C}$ with graphite electrodes and applied fields as high as 1000 V/mm to remove the head-to-head domains that result from the VTE process. To ensure complete poling, the applied field was reversed several times. Afterwards, the crystals were annealed in air at $620\text{ }^\circ\text{C}$ for 10 hours. We refer to these processed crystals as virgin samples. In reference to the ferroelectric properties of these crystals, forward poling will refer to the first domain reversal after uniform poling and backward poling will refer to domain reversal back to the original

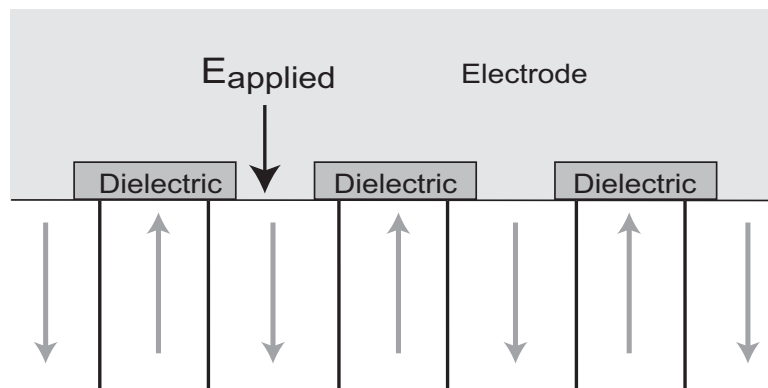


Figure 2.4: Diagram of the patterned electrodes and dielectric on the ferroelectric poled for QPM, along with the domain pattern after poling.

state.

2.3 Electric-field poling

Although the particular ferroelectric properties will be discussed in Chapter 3, it will be important to discuss the methods and tools to perform both the ferroelectric characterization and the periodic poling in this section.

There are several techniques to perform the necessary ferroelectric patterning of lithium tantalate. As stated in Section 1.2, the electric-field poling methods have dominated the development of periodically poled materials and will be used in this work. In this method, electrical contact is made to thin strips of the ferroelectric. An electric field larger than the coercive field is applied to these electrical contacts. Consequently, the regions of ferroelectric located underneath the electrodes are reversed. Figure 2.4 shows a typical patterned dielectric which serves as a blocking layer to prevent overgrowth of the reversed domain.[68]

For most devices and for characterization purposes, liquid-electrolyte electrodes will be used at room temperature. For most periodically poled devices, patterned photoresist (1- μm -thick Shipley 3612, hard baked at 140 °C for 2 hrs) was used as the dielectric layer. Fixtures made from acrylic for use with liquid-electrolyte contacts are shown in Figure 2.5. One fixture is specially designed for two-inch-diameter wafer

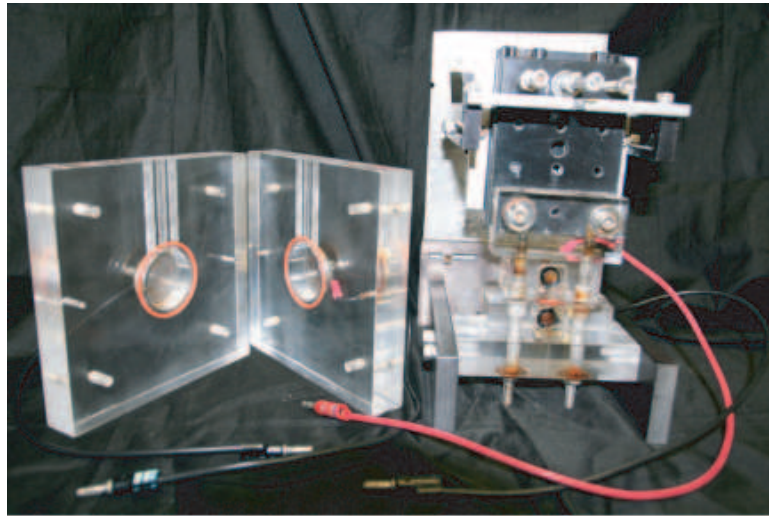


Figure 2.5: Periodic poling and ferroelectric characterization takes place with liquid-electrolyte electrodes using fixtures shown here. (Left) A clam-shell fixture for periodic poling of 2" wafers. (Right) A spring-loaded fixture which allows the use of a wide variety of O-ring sizes.

periodic poling experiments and the other fixture designed to accommodate a wide variety of O-ring sizes.

Metal electrodes such as aluminum (with patterned photoresist as the dielectric layer) or ni-chrome (with 1800-Å-thick sputtered SiO_2 as the dielectric layer) are used in a few periodic poling experiments to enhance the nucleation when liquid-electrolyte electrodes are inadequate.[68]

2.3.1 Domain Visualization

After periodic poling, domains are imaged using classical techniques. In LN, domains can be easily imaged when viewed through crossed polarizers.[19] Unfortunately in lithium tantalate, the field-induced birefringence is not large enough to use this simple technique. Chemical etching techniques are preferred but can cause rearrangement of domain walls.[69] In this work, short etches of ~ 10 min in 50% hydrofluoric acid in water have been performed to minimize domain rearrangement. Figure 2.6 shows two periodically poled samples that have been processed with different etch times. These

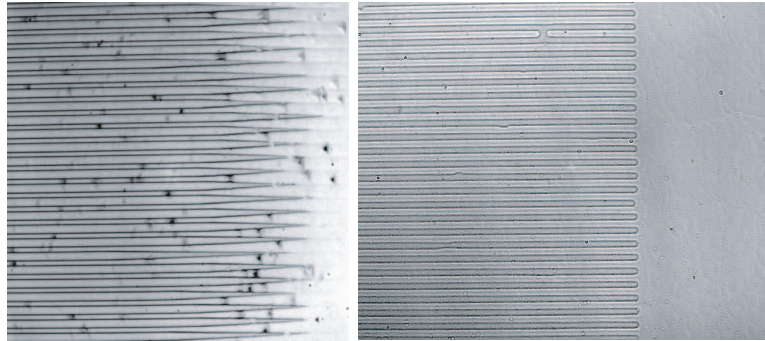


Figure 2.6: (Left) A periodically poled device with an $8\text{-}\mu\text{m}$ -period was etched for 40 min in hydrofluoric acid. Here we see the domains have shrunk inwards from the domain ends. (Right) A periodically poled device with an $8\text{-}\mu\text{m}$ -period was etched for 10 min in hydrofluoric acid. Here we see no domain shrinkage because of the short etch time.

two pictures illustrate the effect of domain rearrangement. Long etch times cause a minimization of surface wall energy and the periodic domains shrink inwards from the two ends. Short etch times prevent domain rearrangement, but produce only shallow features that require more sensitive imaging.

Chapter 3

Properties of VLT

3.1 Ferroelectric Properties

The ferroelectric properties of VLT are distinctly different from SLT fabricated by melt-growth methods. For example, Gopalan et al. show that the coercive field has a linear relationship with the deviation from stoichiometry.[60, 62] Thus, a careful study of how VTE affects the ferroelectric properties of the resulting VLT is useful. In particular, we will examine the homogeneity and the deviation from stoichiometry. To engineer an appropriate periodic structure for optical frequency converters, accurate measurements of the coercive field, spontaneous polarization, and domain wall velocity and nucleation as a function of applied electric field are extremely important.[68, 70]

3.1.1 Coercive Field

Measurements of coercive field and spontaneous polarization were performed on various virgin VLT crystals. Using liquid-electrolyte electrodes contacting a 9.5-mm-diameter area, simple hysteresis loops were used to measure these characteristics. A triangle wave with peak-to-peak amplitude of 200 V (or 400 V for samples with coercive fields greater than 200 V) was applied to the crystal with a Trek 623B High Voltage Amplifier; the current delivered to the sample was measured with a 1

k Ω resistor placed in series as a current monitor. The delivered charge, obtained by integrating the current (measured as the voltage drop across the series resistor), is proportional to the reversed spontaneous polarization over the poled area. If the material being poled is homogeneous in composition, and the magnitude of the spontaneous polarization is uniform, the delivered charge is twice the product of the spontaneous polarization and the poled area, $q(t) = 2P_s A(t)$, allowing the spontaneous polarization to be calculated from the charge delivered and the area of the electrode. Note that we have neglected the displacement charge which is proportional to the rate of change of the applied voltage since it is small in comparison to the spontaneous polarization. The spontaneous polarization can be calculated by taking the maximum delivered charge divided by twice the area of the electrode. One can then construct a hysteresis loop of the displacement as a function of applied field. A typical hysteresis loop measurement with a period of 500 s on a 1-mm-thick sample is shown in Figure 3.1.

In this work the “apparent” coercive field for both forward and reverse poling is defined as the applied field where the displacement crosses through zero. However, difficulties arise when measuring coercive field, due to the time-dependent nature of poling. To clarify this point, measurements of “apparent” coercive field as a function of triangle wave frequency are shown in Figure 3.2. These measurements were performed on the same sample area. Since nucleation and domain-wall velocity are both field and time dependent, long poling periods result in small coercive fields. However, as the measurement time approaches 1000 s the coercive field approaches an asymptotic value. For convenience, a period of 500 s was selected as a standard measurement time.

To explore the effect of VTE on coercive field and spontaneous polarization, hysteresis loops were measured on several samples, as well as on different locations on some of the samples. Figure 3.3 shows the measured coercive field as a function of VTE processing time at 1360 °C on samples of two thicknesses, 0.5 mm and 1.0 mm. Samples treated at 1360 °C and subsequently processed for varying times at 1100 °C showed no significant change in coercive field. It is important to note a few key characteristics appearing in Figure 3.3. First, with increasing VTE time the coercive

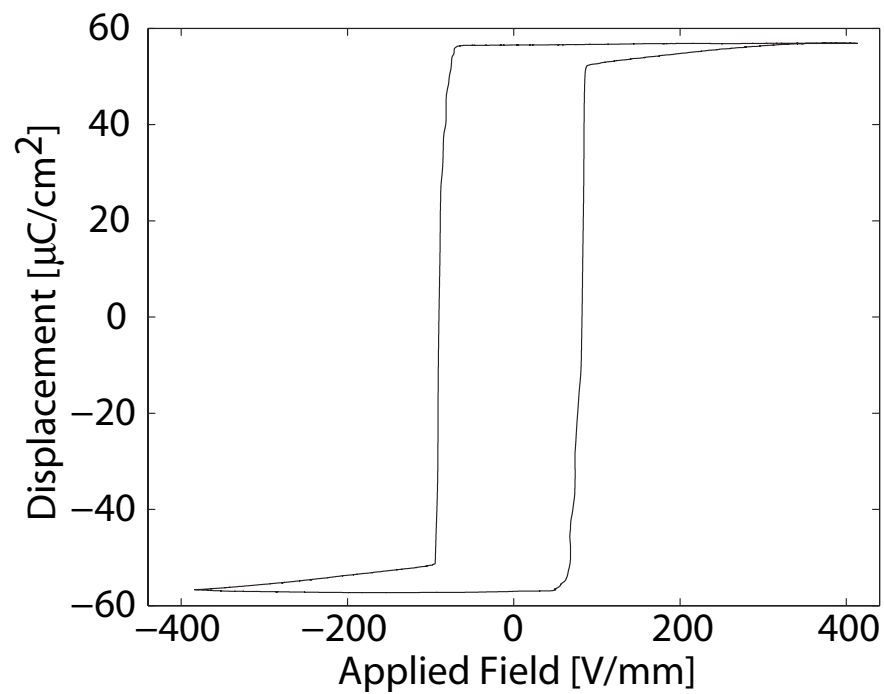


Figure 3.1: A typical hysteresis loop for VLT. A typical hysteresis loop for a 9.5-mm-diameter area on a 1-mm-thick VLT sample with a loop period of 500 s. The widening of the loop at large applied fields result from expansion of the inverted region beyond the 9.5-mm-diameter o-ring.

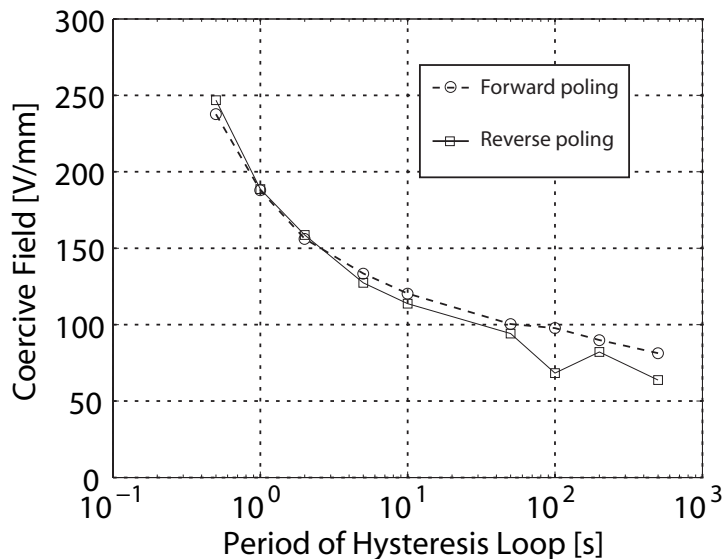


Figure 3.2: A typical dependence of coercive field for a single area (9.5-mm-diameter) on a 1-mm-thick VLT sample as a function of loop period for both forward (circles) and reverse (squares) coercive fields.

field drops to as low as 60 V/mm. Second, the required VTE time to reach 60 V/mm does not scale with the square of the material thickness, which suggests that the VTE process is not diffusion limited but rather either surface-reaction-rate limited or evaporation-rate limited. Material-loss measurements suggest that the two-phase powder, used as the source of Li_2O , sources more than three times the required Li_2O to exchange the original CLT substrates to the stoichiometric composition. Since the covering platinum crucible covers most of the powder area, surface reaction rate is most likely the limiting rate for the VTE process. This surface reaction rate may be important for designing a process to scale to thicker substrates. Assuming that the linear relation between coercive field and deviation from stoichiometry can be extrapolated to these low fields,[60] the reduction in coercive field to 60 V/mm suggests that the VLT crystals are 350 times closer to stoichiometry than their congruently melting counterparts. Given the 48.39 mol % composition of CLT crystals, the VLT crystals correspond to a lithium deficiency of approximately 50 ppm. The asymptotic behavior of the coercive field for long processing times suggests that the LiTaO_3

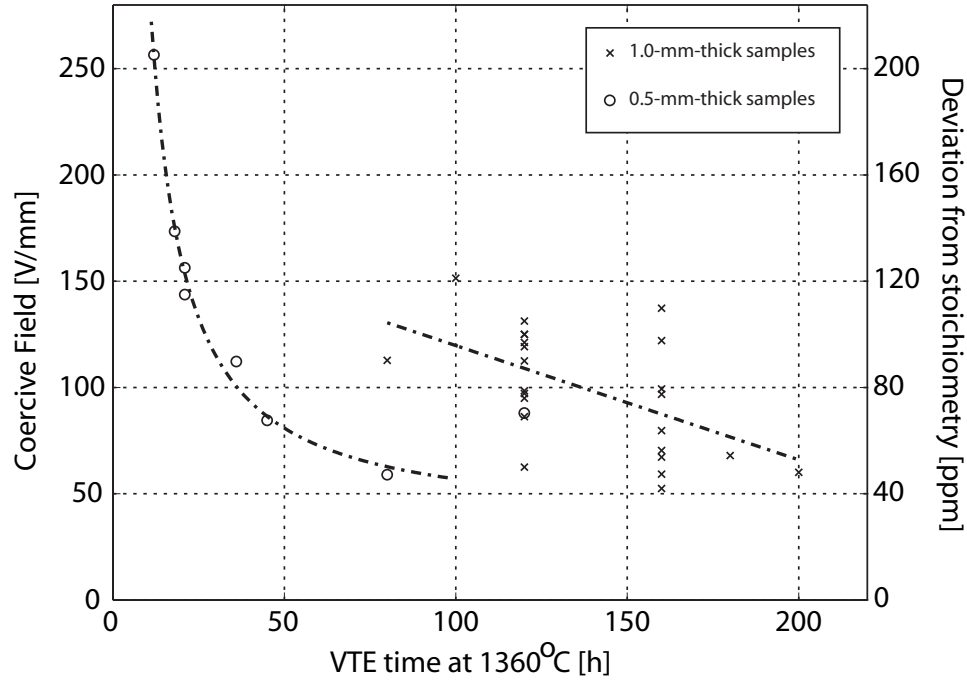


Figure 3.3: Coercive field as a function VTE time at 1360 °C. Circles indicate 0.5-mm-thick samples and crosses indicate 1-mm-thick samples.

phase boundary is extremely close to 49.996 mol %, corresponding to approximately 50 V/mm. Hence, it may not be beneficial to VTE for much longer than the time used here.

It is also important to measure the uniformity of 2" wafer substrates as domain engineering and any nonlinear devices will depend critically on the homogeneity of the sample across such a large area.[71] A 9.5-mm-diameter O-ring was used to sample five spots on the wafer to test the uniformity of the coercive field. Figure 3.4 shows results in a typical wafer. There is approximately a 15 V/mm difference from one side of the wafer to another. This difference correlates with the orientation of the wafer inside the platinum crucible, with the side of the wafer closest to the powder having a higher coercive field than the side farthest from the powder. Most wafers have been processed with the major flat, i.e. the +Y axis, closest to the powder for ease of mounting the crystals in the crucible. We have not seen any dependence of periodic-poling quality or nonlinear optical performance that could be related to this

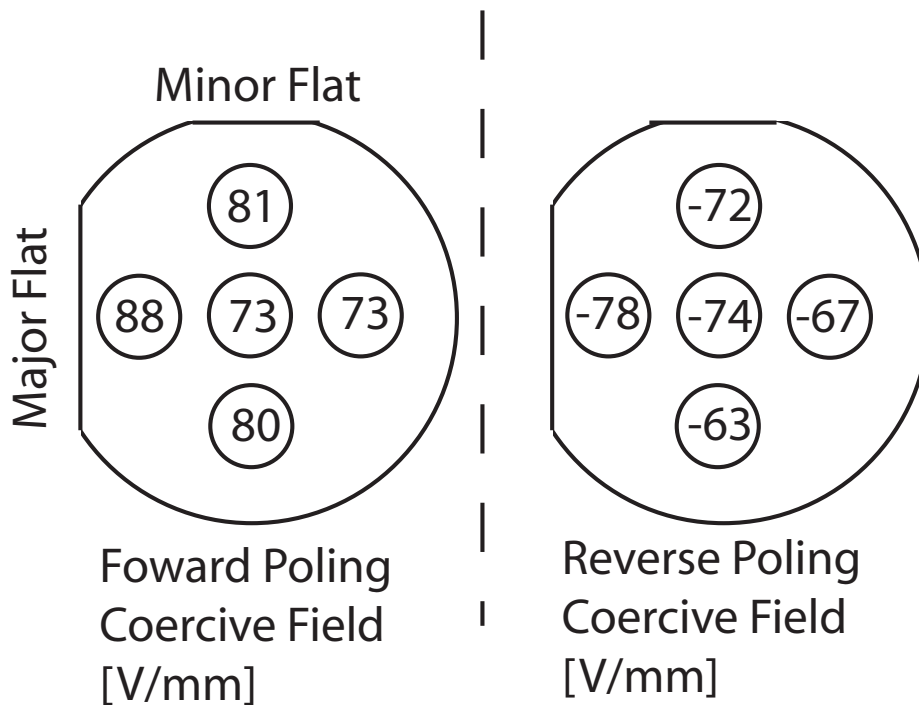


Figure 3.4: Coercive field uniformity over a typical wafer. The observed 15 V/mm variation corresponds to a difference in $[\text{Li}]/([\text{Li}]+[\text{Ta}])$ of approximately 15 ppm.

level of nonuniformity.

3.1.2 Domain Wall Velocity

To understand how the VTE process affects the poling dynamics, attempts to characterize the domain wall velocity versus applied field were performed. Using uniform LiCl electrodes, a poling pulse was applied to the VLT sample. A typical voltage waveform for this pulse is shown in Figure 3.5. Using uniform LiCl electrodes, a poling pulse as shown in Figure 3.5 was applied to several samples. A 100- μs nucleation pulse (with magnitude corresponding to approximately twice the coercive field) followed by a field of varying durations, at a value for which the velocity was to be characterized, was applied to each sample, and the current delivered to the sample was measured using a series resistor. During the application of the field, the current rises linearly if the domain wall velocity is constant, assuming isotropic 2-dimensional

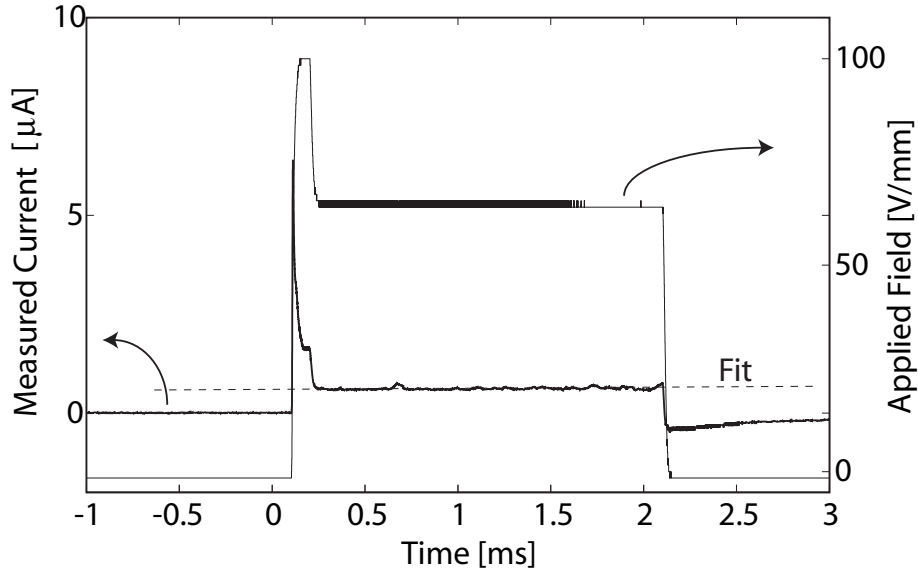


Figure 3.5: Voltage and current traces for a typical domain wall velocity measurement.

growth. Here, the relative domain wall velocity has been calculated by assuming that the best fit to the rate of change of the measured current at a fixed applied voltage was proportional to the domain wall velocity. It has been shown that the domain wall velocity can increase by orders of magnitude during domain merging.[60] Effects of merging were avoided as only a small fraction of each sample was poled. Figure 3.6 shows measurements of the relative domain wall velocity for several samples. Since samples of varying coercive fields (E_c , ranging from 70 V/mm to 115 V/mm, approximately 0.7-1.3 times the mean coercive field) were measured we have plotted the domain wall velocity against difference of the applied field (E_{app}) and the measured coercive field of the sample.

The relative domain-wall-velocity measurements show agreement from sample-to-sample. It is clear that absolute domain wall velocity measurements must be done by measuring real domains inside the poled area. Previous studies have used chemical etching to reveal the domains.[70] This visualization method can alter the domain pattern after poling, especially for low coercivity materials like VLT.[69] From these measurements, a fit to these data points shows the following dependence of velocity

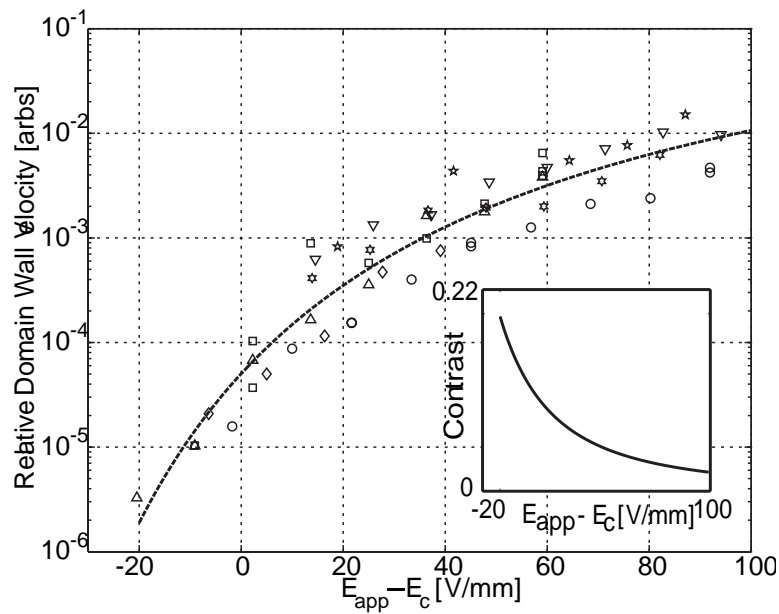


Figure 3.6: Relative domain wall velocity measurements as a function of the difference between the applied and the coercive field. Measurements were performed on several samples with varying coercive fields. (Inset) Contrast (derivative of the log of the domain wall velocity with respect to field) versus the difference between the applied field and the coercive field.

versus field given in V/mm.

$$v \propto \exp\left(\frac{-750 \pm 130}{E_{\text{app}} - E_c + 78 \pm 9}\right) \quad (3.1)$$

The bulk of the uncertainty of this fit stems from the sample-to-sample variation of the measured coercive field. This velocity-field curve provides insight into the optimal poling conditions for the material. A contrast curve (the derivative of the log of the velocity with respect to applied field, inset in Figure 3.6) quantitatively shows the sensitivity of the domain wall velocity to applied field.[72, 70] For periodic poling, one would like to operate at the maximum contrast point since it provides the maximum control over the size of poled domains. These measurements suggest using smaller poling fields for maximum contrast. From Refs. [72] and [70], a 1 kV/mm of electric field change provided a contrast value of 5 and this contrast value was required for good periodic poling in magnesium-oxide-doped lithium niobate and congruent niobate, respectively. The charge required to screen the 1 kV/mm electric field results in micron-scale growth of domains underneath the patterned dielectric layer (e.g. patterned photoresist, or patterned spin-on-glass). In VLT, at fields which result in good nucleation (approximately 80 V/mm above E_c), for a contrast value of 5, approximately 100 V/mm of electric field is required. Thus, the growth of domains underneath the patterned dielectric layer should be reduced from the order of microns in congruent lithium niobate to tenths of microns in VLT.

3.1.3 Domain Stability and Backswitching

In both lithium niobate and lithium tantalate, after domain reversal one can observe a spontaneous relaxation back to the initial domain state.[73] This phenomenon of spontaneous relaxation is commonly referred to as backswitching and can depend on the ferroelectric, material composition and temperature. Backswitching can be hindered or enhanced by appropriate choice of the applied poling field. For example, application of a stabilization field of 18 kV/mm after poling congruent lithium niobate for only 50 milliseconds will prevent backswitching. A measurement of the

necessary stabilization field can be performed by appropriately manipulating the applied voltage.[74] The applied voltage waveform is shown in Figure 3.7. Here, we apply a forward poling pulse and then apply a holding voltage for various times. By measuring the field required to backswitch the poled area as a function of a holding voltage and holding time after poling, one can estimate the hold voltage and time necessary to prevent significant backswitching. A small 9.5-mm-diameter area of virgin substrate was forward poled. After a short poling time, a holding voltage was applied for varying times. Once the prescribed hold time was completed, the applied field was ramped towards the reverse coercive field. The backswitching field was measured as the field where the backswitching current rises above the noise floor (here referred to as the backswitching current threshold). A plot of the dependence backswitching field on hold time and hold voltage is shown in Figure 3.8.

The picture drawn from the data is as follows. Immediately after poling, there is a time constant on the order of 100 ms during which the sample is likely to backswitch without a holding voltage. After this time, the backswitching voltage saturates at a value of approximately -11 V/mm. If the applied field reaches this value, domain walls can move, causing the existing domains to shrink. If the applied field is too great during this holding period, the sample can completely overpole at which point the backswitching field becomes the reverse coercive field of the sample. These two levels for backswitching suggest that there is an inherent difference between the field required for domain motion and the field required for domain nucleation. Clearly, with the appropriate choice of holding field and holding time one would hope to find an operating point to prevent backswitching, stabilize the domains and not overpole the sample. For samples of different coercive fields, the domain wall velocity will be different for the same stabilization field and thus there is no simple formula for the appropriate choice of stabilization field and time as a function of coercive field. However, we have found for coercive fields close to 100 V/mm, a stabilization field of 55 V/mm for 1 hour is sufficient to stabilize the domains without significant growth of periodically poled domains.

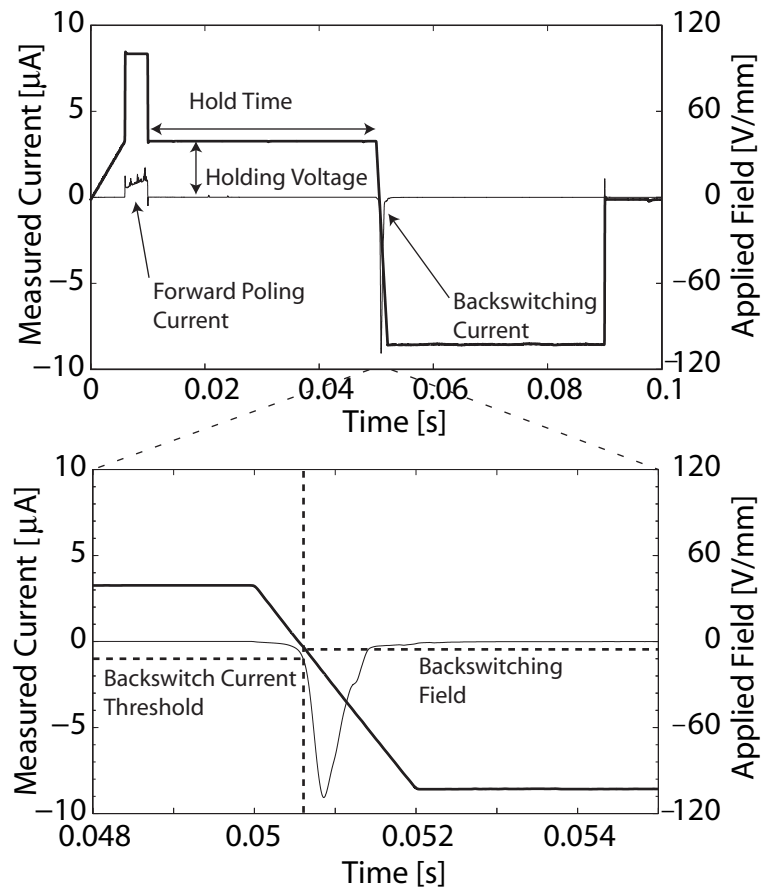


Figure 3.7: Voltage and current versus time for a typical backswitching measurement.

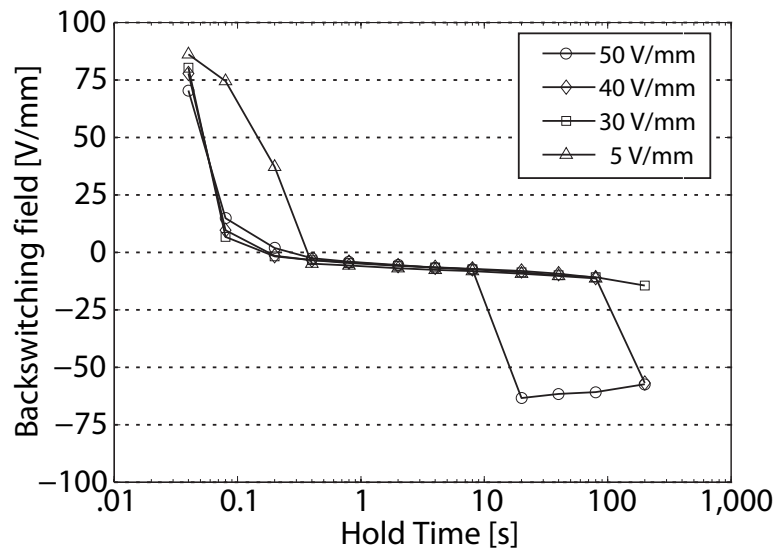


Figure 3.8: Backswitching field as a function of hold time for various hold voltages applied to a 1-mm-thick sample. Backswitching field is pinned to a level of -11 V/mm until the area fully poles and becomes the coercive field. This suggests a difference between domain motion and nucleation fields for long holding times.

3.1.4 Domain Patterning and Domain Instabilities

Recently, it has been shown that domains in near-stoichiometric lithium tantalate can rearrange during chemical etching.[69] This domain rearrangement remains a difficult problem to solve in the development of a periodic poling process. Periodically-poled domains collapse and merge with other nearby domains during the etching with hydrofluoric acid (HF) usually used to reveal the domain structure. This step is not necessary, however, since alternative methods for visualizing the domains can be used to monitor the results of this process but these are often extremely convenient. Moreover, polishing before periodic poling, which may be important for adequate lithography, increases this instability. It was found that chemical etching with HF before periodic poling reduces the sensitivity to chemical etching after poling. However, etching prior to periodic poling also alters the poling characteristics of the sample, e.g. too long an etch results in samples susceptible to overpoling. This result suggests that a thin layer at the surface of the as-VTE'd or as-single-domain-poled sample

Table 3.1: Effects of pre-poling and post-poling etching using 50 % HF on attempts to pole an 8 - μm period.

Pre-poling etch time	Post-poling etch time		
	10 min	20 min	40 min
0 min	good periodic pattern / unstable	good periodic pattern / unstable	good periodic pattern / unstable
10 min	good periodic pattern / stable	good periodic pattern / shrinking	good periodic pattern / unstable
20 min	poor periodic pattern / stable	poor periodic pattern / stable	poor periodic pattern / shrinking
30 min	no periodic pattern / stable	no periodic pattern / stable	no periodic pattern / stable

stabilizes domains and prevents overpoling. Periodically-poled domains become unpinned when this layer is chemically removed and they become free to collapse and merge. Table 3.1 shows the periodically poled domain (8- μm period) quality and stability effects of pre-poling and post-poling etching using 50% HF as the chemical etchant on unpolished virgin samples.

To clarify the difficulties in the visualization steps, samples that have not been polished before poling but have been etched in 50% HF for a short time, can be etched for a short time after periodic poling without unpinning the domain pattern. These samples give the most reproducible results for periodic poling of bulk samples. For all the attempts, the applied electric field waveforms did not produce periodic patterns with any of the long pre-poling etching times. Although not attempted here, experiments that increase the nucleation may prove to allow fabrication of periodic patterns in samples which have undergone long pre-poling etches. Unfortunately in all these cases, the virgin wafers are not flat. They possess a saddle-shaped bow that can be as large as 40 μm . This bow makes patterning of the dielectric layer by photolithography very difficult for periods less than 8 μm . Periods larger than or equal to 8 μm can be patterned adequately for periodic poling.

In an attempt to improve the wafer flatness, polishing experiments were performed at different points of the process. Process flow charts in Figure 3.9 describe the location of the polishing steps and/or additional hydrofluoric acid etching steps in

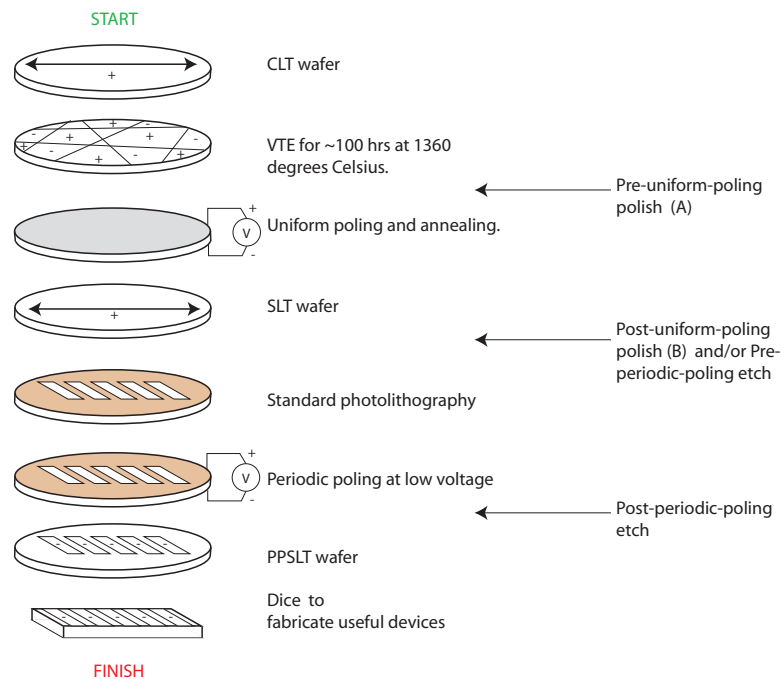


Figure 3.9: Processing flow charts that shows where polishing or etching could occur.

the process flow. Table 3.2 shows the qualitative results from these experiments.

The observations show that polishing the crystals before the uniform poling step can lead to stable domains. In particular, polishing only the eventual $+z$ face of these crystals leads to stable domains and can provide an improved surface for lithography. It should be noted, however, that these tests have been performed with the patterned photoresist on the $+z$ face. It is not clear whether the polishing should occur always on the eventual $+z$ face or on the face that will be patterned. Photolithographic patterning on this surface has allowed periods as small as $5 \mu\text{m}$ to be developed.

Domain backswitching and instabilities during chemical etching have not prevented periodic poling of full 2" wafers of high quality. Taking virgin full wafers and using a short (10 min) etch in 50% HF before lithography enables us to periodically pole wafers using a 200 V/mm, 300-millisecond-long poling pulse. A 55 V/mm holding field was applied for 20 minutes to prevent backswitching. Measured poling current suggests self-termination [70] occurs in VLT under these conditions. The short HF etch before periodic poling enables a short (15 min) HF etch after poling to reveal

Table 3.2: Qualitative observations of the domain stability and periodic poling quality of poled samples after polishing and etching.

Polishing Step ^a	Periodic domain quality	Domain Stability
None	excellent	moderate
(A) +Z face	excellent	moderate
(A) -Z face	moderate	poor
(A) both faces	moderate	poor
(B) +Z face	good	moderate
(B) -Z face	moderate	poor
(B) both faces	good	poor

^a(A) represents polishing before uniform poling and (B) represents polishing after uniform poling as shown in Figure 3.9

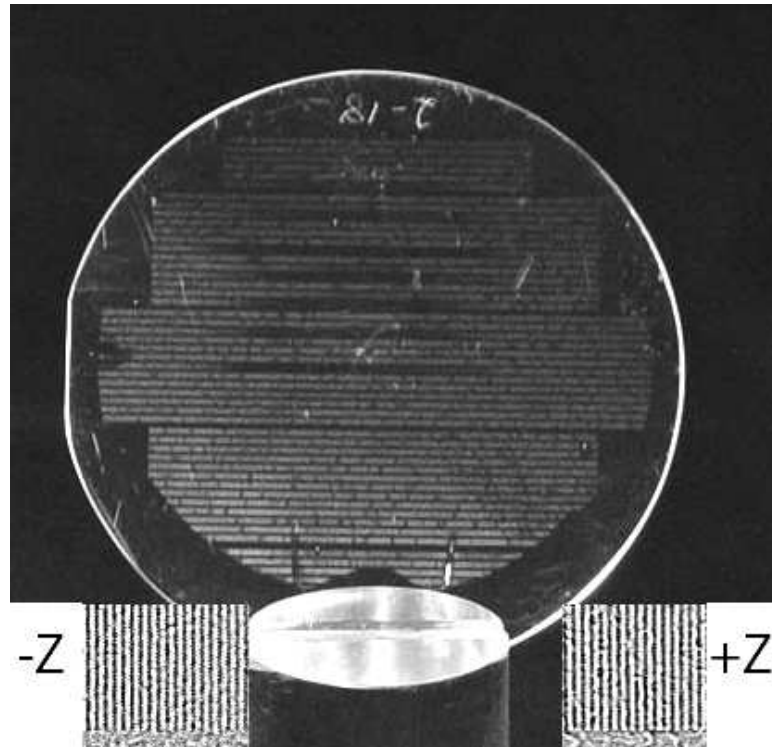


Figure 3.10: A 2" SLT wafer (202-18) poled with an 8 μm period. Etched +Z and -Z faces are shown inset.

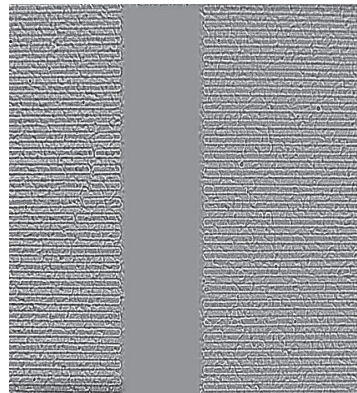
domains without destabilizing them. A full 2" wafer, poled with an 8- μm period for second harmonic generation (SHG) of 532 nm is shown in Figure 3.10 with samples of +z and -z areas shown in inset. Unpoled areas are the result of lithographic defects.

Similar poling methods using liquid-electrolyte electrodes through a photoresist insulator have allowed 1-mm-thick wafers to be poled for various applications, including generation of 589-nm light by both sum frequency generation and second harmonic generation (10.5 μm to 11 μm), generation of 515-nm light (7 μm) by SHG, and generation of 1064 nm light by SHG ($\sim 32 \mu\text{m}$). Photographs of the periodic poling of various samples are displayed in Figure 3.11.

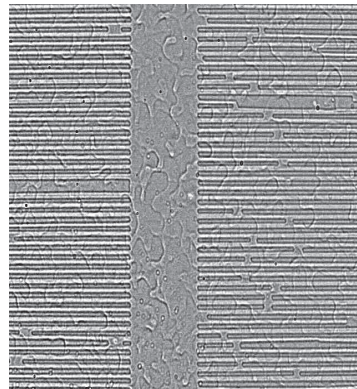
To attain the 5- μm period required for generation of 458-nm radiation by SHG, higher density nucleation was required. To increase nucleation, ni-chrome electrodes were sputtered on top of patterned SiO_2 . The SiO_2 was sputtered on the +z surface of the VLT wafer to a thickness of 1800 Å. A 1-ms-long poling nucleation spike of 300 V/mm was used to further enhance the periodic domain quality. Using these nucleation enhancements, a 1.5-cm-long, 0.5-mm-thick, +z-surface-polished VLT sample was periodically poled for SHG of 458 nm at periods around 5 μm . A picture of the 5- μm -period domains is shown in Figure 3.12.

3.2 Optical Properties

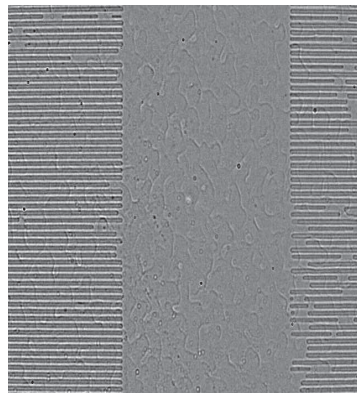
After measuring the ferroelectric properties and ensuring periodic domain patterning could be performed, measurements of the optical properties that influence the utility of VLT were made. In this section, measurements of the nonlinear coefficient, sensitivity to photorefractive damage, linear and nonlinear absorption are discussed. Measurements of the birefringence of VLT at 1 μm and 2 μm wavelengths are also discussed. Since these properties may also be composition dependent, VLT will refer to near-stoichiometric lithium tantalate with a coercive field of approximately 100 V/mm unless otherwise stated.



a)



b)



c)

Figure 3.11: Images of domains. a) a 32- μm -period grating b) a 10- μm -period grating and c) a 7- μm -period grating.

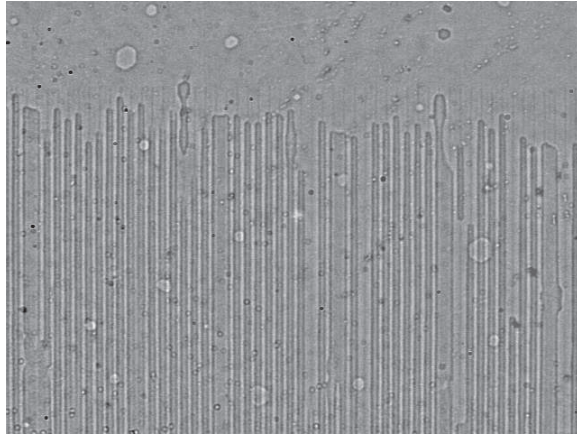


Figure 3.12: Image of 5- μm domains in VLT.

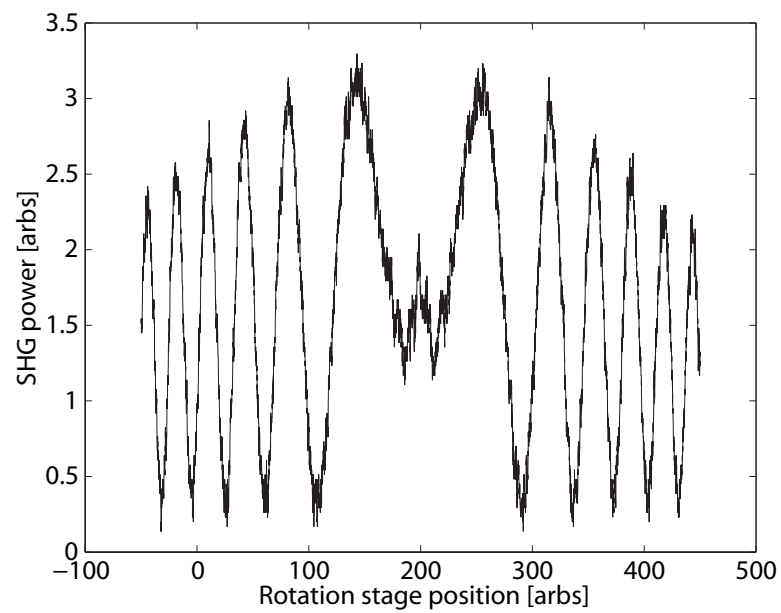


Figure 3.13: A typical Maker fringe measurement of the d_{33} coefficient of VLT.

Table 3.3: Maker fringe measurements of various crystals.

Sample	Nonlinear Coefficient $\frac{d_{33,X}}{d_{33,CLN}}$
Congruent LN	1
Congruent LT	0.67 ± 0.05
Double Crucible Czochralski SLT	0.70 ± 0.05
VLT	0.67 ± 0.05

3.2.1 Nonlinear Coefficient

To measure the nonlinear coefficient of these materials, Maker fringe measurements[75] of the d_{33} coefficient of congruent lithium niobate, CLT, SLT prepared by double-crucible Czochralski growth from Oxide Corporation and VLT were performed. Figure 3.13 shows a typical Maker fringe measurement for a 1-mm-long sample of VLT, using 100 mW of 1064-nm single-frequency radiation and a beam size of $40 \mu\text{m}$ by $30 \mu\text{m}$ ($1/e^2$ -intensity radius) at room temperature. The results are normalized to congruent lithium niobate and are tabulated in Table 3.3.

3.2.2 Photorefraction

Historically, the limiting factors that have prevented high-power visible-light generation at near-room temperatures in ferroelectrics like LN and LT, have been PRD and GRIIRA. These two effects are reduced as the density of intrinsic defects are reduced in stoichiometric and Mg-doped crystals. It has been shown that the coercive field (E_c) is proportional to the deviation of the composition from stoichiometry and thus with the density of intrinsic defects which cause PRD and GRIIRA.[62, 32] As shown in section 1.4.1, the saturated space charge field and hence the light-induced index change can be drastically reduced with near-stoichiometric crystals.

To characterize the transport properties that influence the saturated space charge field in VLT, we measured the photoconductive and photogalvanic currents for a given light intensity and applied voltage. Use of a focused laser beam is necessary to reach optical intensities typical of frequency conversion interactions. To avoid pyroelectric currents resulting from heating due to absorption of the focused pump

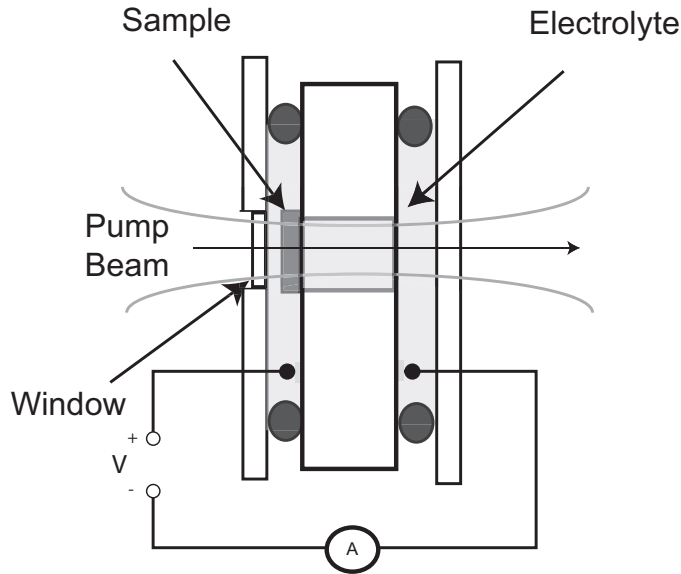


Figure 3.14: Experimental diagram of apparatus for measurement of photoconductivity and photogalvanic coefficients. A probe beam is focused through the sample and the photogalvanic and photoconductive currents are measured in a picoammeter. The sample is mounted on an insulating frame and contacted with liquid electrolyte contacts.

in conventional electrodes, we used a modified liquid-electrolyte, electric-field-poling cell illustrated in Figure 3.14. The probe beam was focused through a quartz window to illuminate the sample. A picoammeter was used to measure the photoconductive and photogalvanic currents from which the respective coefficients could be inferred. The saturated space charge field is the ratio of the photogalvanic coefficient to the photoconductive coefficient.[21, 31, 32]

With 0.5 W of 514.5-nm radiation focused to a 35- μm spot ($1/e^2$ -intensity radius), photogalvanic, and photoconductive currents were measured for VLT at room temperature for samples fabricated with various VTE processing times shown in the Table 3.4.

From these measurements, one can estimate the maximum length useful for frequency conversion as limited by photorefraction. Photorefraction causes a negative lens which in turn causes the interacting beams to fan out, reducing beam quality and limiting nonlinear-device performance. The useful length for frequency conversion can

Table 3.4: Photorefractive Properties of various VLT samples.

Sample Name	VTE time at 1360 °C [h]	Coercive Field [V/mm]	Photogalvanic Coefficient ^a [pA/W]	Photoconductive Coefficient ^a [(pS-cm)/W]
CLT	0	21 000	4.2	0.003
17C	12	260	3.7 ± 0.6	0.13 ± 0.05
18B	18	170	8.6 ± 1.1	0.33 ± 0.19
147D	160	100	2.4 ± 0.2	0.22 ± 0.24

Sample Name	Coercive Field [V/mm]	Saturated Space Charge Field [V/cm]	$L_{\pi/10}$ [cm]
CLT	21 000	1270 ± 300	0.13
17C	260	43 ± 26	4.0
18B	170	32 ± 20	5.3
147D	100	10 ± 8	17

^aThe photogalvanic and photoconductive coefficients are taken for a 35- μ m spot ($1/e^2$ -intensity radius).

be estimated by determining the length where the accumulated photorefractively-induced phase shift reaches approximately $\frac{\pi}{10}$ for extraordinary-polarized radiation and is given by

$$L_{\pi/10} = \frac{\lambda}{10 r_{33} n^3 E_{SC}} \quad (3.2)$$

Here $L_{\pi/10}$ is the useful length, λ is the wavelength, r_{33} is the electro-optic coefficient, n is the refractive index and E_{SC} is the saturated space charge. In lithium tantalate, taking $r_{33} \approx 30$ pm/V and $n \approx 2.2$, this length is approximately given by

$$L_{\pi/10} \approx \frac{1000\lambda}{3E_{SC}}$$

where $L_{\pi/10}$ is given in cm, λ is given in μ m and E_{SC} is given in V/cm. Considering the measured values, it is easy to understand why congruent lithium tantalate does not perform well at room temperature. The measurements of the transport properties

Table 3.5: Photorefractive Properties as a function of wavelength for sample 147D.

Wavelength [nm]	Photogalvanic Coefficient ^a [pA/W]	Photoconductive Coefficient ^a [(pS-cm)/W]	Saturated Space Charge Field [V/cm]	$L_{\pi/10}$ [cm]
514.5	2.4 ± 0.2	0.22 ± 0.24	10 ± 8	17
488	4.9 ± 3	0.61 ± 0.31	12 ± 10	14
457.9	14 ± 1.4	0.96 ± 0.40	14 ± 11	11

^aThe photogalvanic and photoconductive coefficients are taken for a 35- μm spot ($1/e^2$ -intensity radius).

listed in Table 3.4 show a 100-fold reduction of the saturated space charge field in VLT compared to its congruent-composition counterpart. Photorefraction should not impose a limitation on conversion efficiency, since $L_{\pi/10}$ exceeds typical crystal lengths used in practical systems.

Measurements using other argon-ion laser wavelengths were also taken and are tabulated in Table 3.5. For this particular sample, the 100-fold improvement of E_{SC} over congruent-composition crystals is retained for the measured argon wavelengths. It is important to note, that as the photogalvanism increases, the photoconductivity increases nearly commensurately. The saturated space charge field rises only slightly (by a factor of 1.4) as the wavelength is reduced from 514.5 nm to 457.9 nm.

To explore the dependence of the sensitivity to photorefractive damage at larger peak intensities, a 1.064- μm , 6-ps, 78-MHz, 9.5-W-average-power modelocked laser was used to generate up to 2 watts (average-power) of 532-nm radiation by SHG using a 9.5-mm-long VLT sample. The 2 watts of 532-nm light was focused to a spot size of 30 μm ($1/e^2$ -intensity-radius) in a second VLT crystal in the measurement apparatus. Samples measured using this apparatus showed an increase of a factor of 2 of the saturated space-charge field compared to the original low-peak-power saturated space-charge field measured at 514.5-nm.

It is important to note that for more accurate measurements of the saturated space-charge field, improvements in the experimental setup must be made. The dominant source of noise in these experiments was pyroelectric in origin. Pyroelectric

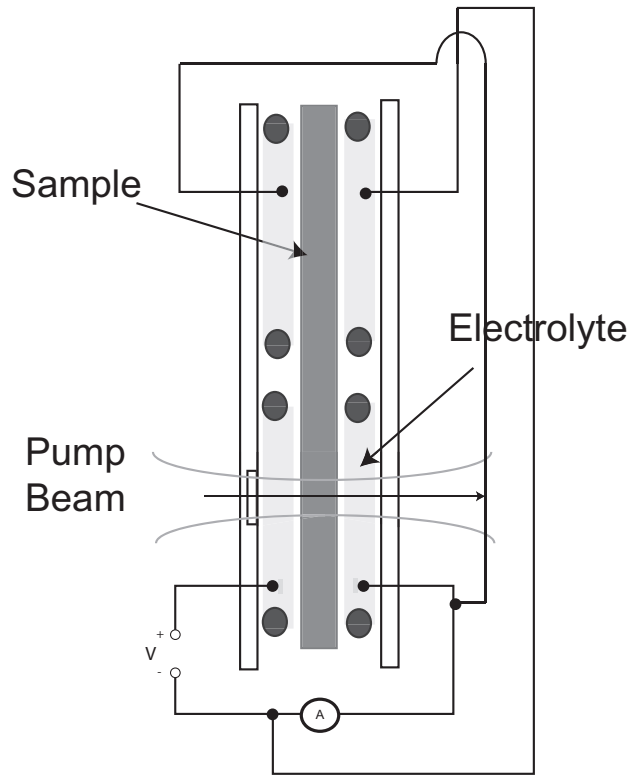


Figure 3.15: Experimental diagram of the improved apparatus for measurement of photoconductivity and photogalvanic coefficients.

currents can fluctuate with the variation in room temperature. Further, a pyroelectric response of the temperature of the whole experimental fixture must attain equilibrium after the laser is turned on and off. The time required to reach equilibrium is quite long (~ 40 minutes) and thus the pyroelectric currents can fluctuate significantly during that time. To reduce the effect of these currents, the fixture in Figure 3.14 was slightly modified. Figure 3.15 shows a fixture with two nearly equal area electrode contacts on the sample. When the electrodes of each area are connected in anti-parallel, the pyroelectric currents cancel. Since the probe beam only interrogates one of these two areas, the photogalvanic and photoconductive currents are still available.

With this improved fixture, one can measure the pyroelectric current fluctuation as a function of time with and without the anti-parallel connection; the results are shown

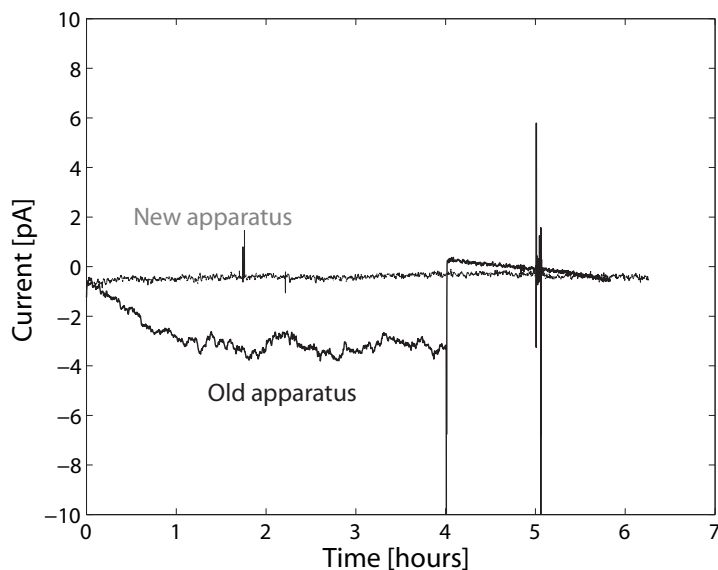


Figure 3.16: Current fluctuations caused by the pyroelectric effect are greatly reduced when the improved fixture is used.

in Figure 3.16. One can clearly see the several-fold decrease of the fluctuation as a function of time. This fixture should improve the accuracy of future measurements.

3.2.3 Absorption

In the absence of photorefraction, absorption in nonlinear materials ultimately sets the average-power-handling limit.[76, 77] This absorption can arise either from extrinsic impurities, native defects or intrinsic interband or multi-phonon absorption. To measure the absorption in VLT, several measurement tools and experimental techniques were employed. Near the ultraviolet band edge, a Cary 500 Spectrophotometer and a SOPRA spectroscopic ellipsometer (in transmission mode) were used to characterize the absorption for both the ordinary and extraordinary waves. In the visible and near-infrared, photothermal common-path interferometry[78] was used to measure the both the absorption and any induced infrared absorption for various wavelengths. We define an induced infrared absorption as the increase of the infrared absorption caused by the presence of another wavelength. A Fourier-transform infrared (FTIR)

spectrometer was used to probe the absorption of the ordinary wave in the mid-infrared. Finally, a z-scan measurement using a picosecond 532-nm source was used to measure the two-photon absorption of VLT.

Ultraviolet Absorption

A Cary 500 Spectrophotometer was used to measure the ordinary polarized transmission of both CLT and VLT samples of thickness 0.2 mm, 0.5 mm and 1 mm. The ultraviolet absorption was calculated from the transmission spectra, where the results for different lengths can be used to eliminate the effects of Fresnel reflection at the two surfaces of the sample. The maximum thickness of VTE samples together with the 0.5% transmission resolution of the spectrophotometer limited the sensitivity of the absorption to $\sim 0.1 \text{ cm}^{-1}$. To measure the extraordinary wave, a SOPRA spectroscopic ellipsometer aligned in transmission mode was used to measure transmission spectra of end-face-polished VLT samples of thickness 1 mm and lengths 7 mm, 10 mm and 20 mm. The maximum length of measured VTE samples and transmission uncertainty limited the sensitivity to approximately 0.05 cm^{-1} . Ordinary wave absorption was also measured with the spectroscopic ellipsometer and was in good agreement with Cary 500 spectrophotometric data.

Absorption of both VLT and CLT are shown in Figure 3.17. These measurements agree with previous measurements on similar VLT and CLT of varying Fe^{2+} and Cr^{2+} concentrations.[57] It is important to note that these measurements were performed at low intensities and may not be fully representative of what one would measure at laser intensities seen in frequency conversion experiments. It should also be noted that Ref. [79] characterized the composition of similar VLT samples via UV absorption edge to an accuracy of $\pm 0.05 \text{ mol } \%$. Using the wavelengths where the sample exhibits 20 cm^{-1} and 50 cm^{-1} of ordinary-wave absorption, one can estimate the sample has a composition of 49.97 mol % and 49.96 mol % respectively. This estimation agrees with the estimation of the composition via the ferroelectric coercive field method within the measurement error. Note that this measurement error originates from the uncertainty of the composition of the original reference samples in Ref. [79].

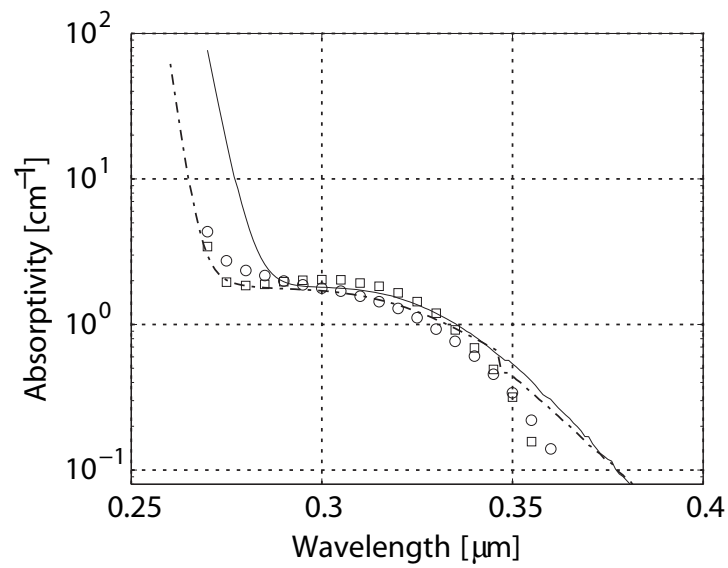


Figure 3.17: Ordinary and extraordinary absorptivity for both CLT and VLT. CLT ordinary-wave absorptivity measured on the Cary 500 Spectrophotometer is shown as the solid curve. VLT ordinary-wave absorptivity measured on the Cary 500 Spectrophotometer is shown as the dashed curve. Circles and squares represent extraordinary-wave and ordinary-wave VLT absorptivity, respectively, measured on the ellipsometer.

Visible and Near-Infrared Absorption

In the visible and near-infrared, absorption in VLT and in CLT is too small to be measured by simple spectrophotometry. Photothermal common-path interferometry[78] is a very sensitive technique which can measure absorptions as low as 10^{-6} cm⁻¹. Using 457-nm, 488-nm, 514.5-nm, 532-nm, 808-nm and 1064-nm radiation, the absorption of VLT was probed as a function of polarization and position. Each beam was focussed to a 40- μ m spot ($1/e^2$ -intensity radius) inside the crystal. The absorption was measured by detecting the thermo-optic phase shift induced on a 633-nm probe beam by a modulated pump at the wavelength of interest. This same apparatus allows us to measure green-induced infrared absorption (GRIIRA).[57] Using a beam of 532-nm radiation coaligned to the 1064-nm pump beam, we can simultaneously illuminate the same volume of crystal with the 1064-nm and 532-nm radiation. This arrangement allows us to measure the change in absorption of the 1064-nm radiation with and without the 532-nm radiation. This change in absorption is the green-induced infrared absorption (GRIIRA). The sensitivity to GRIIRA has been correlated with the number of anti-site tantalum defects and thus the crystal stoichiometry. Previously, GRIIRA measurements using 514.5-nm radiation showed a 100-fold reduction in similarly fabricated VLT when compared to CLT.[32] Here, the induced 1064-nm extraordinary-wave absorption caused by the presence of extraordinary-polarized and coaligned 488-nm, 514.5-nm, and 532-nm radiation has been measured. Table 3.6 shows results of these measurements. CLT was also measured at 1064 nm and 532 nm and had absorptivities from 0.05-0.1 %/cm and 0.28-0.4 %/cm, respectively.

Absorption in VLT varied in the plane of the sample but these variations were smaller than the sample-to-sample variations listed in Table 3.6. Variations could arise from either inhomogeneous distribution of defects or an inhomogeneous distribution of oxidation states of homogeneously distributed defects. Chemical reduction during either VTE or uniform poling that was not removed during the post-uniform-poling anneal could have introduced this inhomogeneity. Transient behavior similar to effects discussed in Ref. [57] were observed, however, only steady-state, CW absorption measurements are listed. The wavelength and polarization dependence of the absorption is consistent with absorption by Fe²⁺ impurities.[54, 80]

Table 3.6: Absorptivity of VLT samples at various wavelengths. Variations in the absorptivity listed are sample-to-sample variations.

Wavelength [nm]	O-wave Absorption [%/cm]	E-wave Absorption [%/cm]	Induced 1064-nm Absorption ^a [%/(Wcm)]
457	1.0-1.7	0.15-0.35	N/A
488	0.12-0.22	0.10-0.20	0.015-0.06
514.5	0.04-0.08	0.06-0.12	0.007-0.035
532	0.04-0.12	0.04-0.12	(0.05)-0 ^b
808	0.01-0.02	0.00-0.01	N/A
1064	0.02-0.07	0.01-0.04	N/A

^aThe induced 1064-nm absorption is the measured increase in 1064-nm absorption due to the simultaneous illumination of the same volume with 488 nm, 514 nm and 532 nm radiation.

^bBrackets indicate induced bleaching effect was measured.

Mid-Infrared Absorption

To measure the mid-infrared absorption, a BioRad FTS-40 FTIR spectrometer was used. CLT and VLT samples of 0.2-mm, 0.5-mm and 1-mm thicknesses were measured along the ordinary axis. Transmission of each sample was measured and the absorption was calculated. Figure 3.18 shows both these spectra. It can be seen that there is little difference between CLT and SLT, suggesting that the phonon spectrum is not significantly affected by the composition difference.

Change in the ordinary-wave absorption near the 2.9- μm absorption band of OH^- was also measured. The absorption peak of VLT is shifted and is substantially narrower for VLT than CLT as shown in Figure 3.19, which is consistent with past measurements.[81] The height of this peak varies with the atmosphere used for the VTE process. In lithium niobate, the OH^- absorption of both congruent and near-stoichiometric compositions have been measured and are similar to those in CLT and SLT respectively. The narrowing of the OH^- absorption spectrum has been attributed to the removal of lithium vacancies and niobium anti-site defects which modify the stretch-mode vibrational frequency of nearby hydrogen-oxygen bonds.[82] Thus, protons close to different defects will have slightly different absorption center frequencies causing a large spread in the absorption as a function of wavelength. Removal of

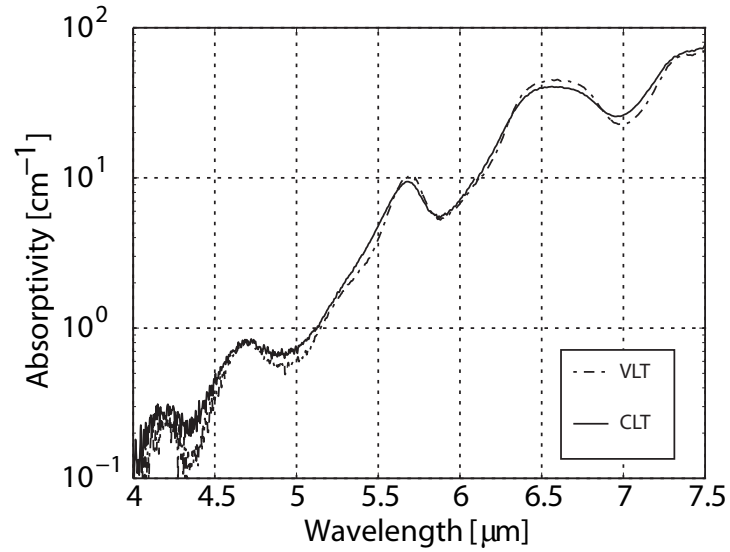


Figure 3.18: Ordinary-wave absorptions for both congruent LT (solid) and VLT (dashed) in the mid-infrared.

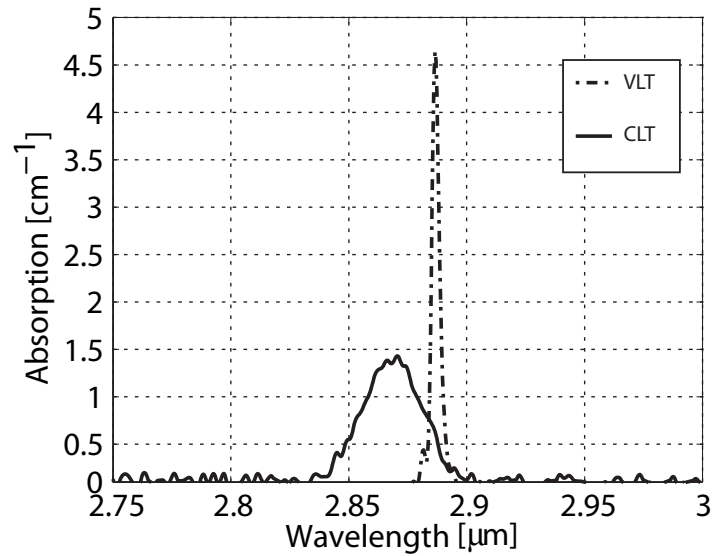


Figure 3.19: Ordinary-wave OH^- absorptions of congruent LT (solid) and VLT (dashed).

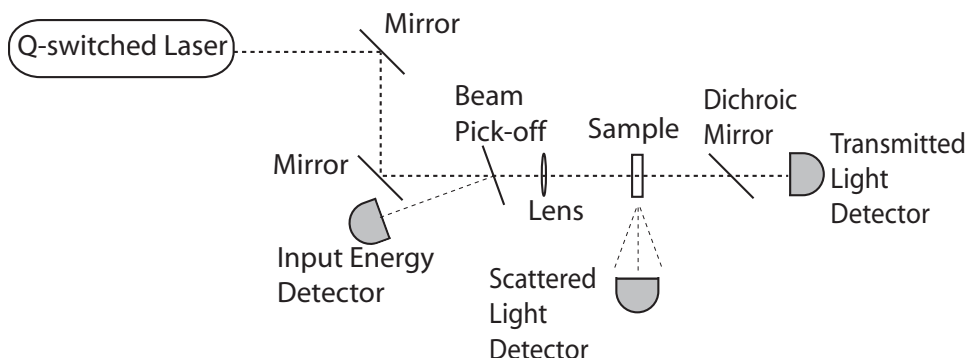


Figure 3.20: Diagram of damage threshold measurement setup.

lithium vacancies and niobium anti-site defects in near-stoichiometric LN reduces the number of different sites for protons and causes a narrowing of the observed absorption. Similar arguments would also explain the change in the OH^- absorption in VLT.

3.2.4 Optical Damage Threshold

For high energy pulses, surface or bulk optical damage will often set the limit for high peak power operation. To measure this effect, 3-mm-long, uncoated samples of CLN, CLT, and VLT were polished and cleaned. It should be noted that the laser-induced damage threshold is greatly affected by improper preparation. For example, if the samples have dust or dirt stuck to the input facet, the diffraction or heat from these imperfections can create intensity or thermal variations that may cause damage before the material would normally suffer damage. Improper surface polishing can affect the laser-induced damage threshold in a similar way. Thus, it was critically important to prepare and handle samples reproducibly to ensure that surface contamination or surface roughness did not affect our measurement.

A 12-ns-pulsewidth, Q-switched, 2.4-mJ, 10-Hz-repetition-rate, multi-longitudinal mode, single-transverse mode, 1064-nm Nd:YAG laser was loosely focused to a $55\text{-}\mu\text{m}$ spot ($1/e^2$ -intensity radius) in the crystal. The length of 3 mm was chosen to avoid damage arising from self-focussing effects. Detectors were placed to monitor the input energy, the crystal transmission and the scattered radiation. The experimental setup

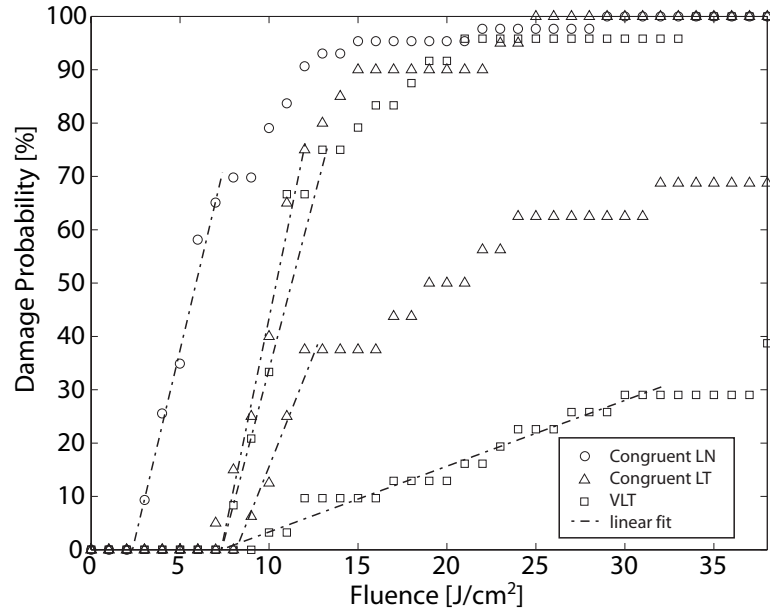


Figure 3.21: Damage probabilities for congruent lithium niobate (circles, $N=43$) and two samples of both CLT (triangles, $N=20,16$) and VLT (squares, $N=31,24$).

is shown in Figure 3.20. The dichroic mirror was used to reject any stray second harmonic generation that could corrupt the measurement. By slowly increasing the input energy and monitoring the correlation of damage to crystal transmission and scattered radiation, statistics about multi-shot, laser-annealed damage probabilities as a function of input energy were collected. We defined the damage fluence as the largest fluence before crystal transmission began to decline within approximately 400 pulses, at a resolution of 1%. This definition was generally correlated with a step-like increase in scattering. The typical number of pulses at a given power incident on one location before damage occurred was approximately 200. We rarely saw damage for extended numbers (up to 4000) of pulses if none was observed after the first 200, for those fluences where damage was observed. Damage statistics are plotted in Figure 3.21 with the number of test spots (N) for each sample indicated.

Measured damage fluence thresholds for congruent lithium niobate, CLT and VLT are 2.3 J/cm^2 , 7.3 J/cm^2 , 7.3 J/cm^2 respectively for a $55\text{-}\mu\text{m}$ radius. The damage

threshold was measured by extrapolating the Weibull distribution back to zero probability. For all congruent lithium niobate samples surface damage was the predominant damage mechanism, however, for both CLT and VLT all samples damaged in the bulk before the surface. The CLT and VLT samples were all taken from different substrates. It is interesting to note that the two samples of CLT and VLT had widely different defect densities, and some volumes of LT did not damage at even the highest input energies. This suggests that both the concentration of bulk damaging defects in LT and the defects themselves are introduced during the growth of the original LT substrates. The statistical distribution also suggests that the worst-case defects are similar in all the CLT and VLT samples, but that their density varies significantly from sample to sample. It is interesting to note that since the surface did not damage in any of the samples which attained the largest fluence ($\sim 30 \text{ J/cm}^2$), one would expect the laser-induced surface damage threshold of CLT and VLT to be larger than this value. With improved growth conditions, the laser-induced damage threshold of LT should vastly improve by perhaps a factor of 4, greatly exceeding the damage threshold of even coated LN crystals ($\sim 10 \text{ J/cm}^2$).

3.2.5 Two-photon absorption of 532-nm radiation

If all extrinsic impurities and native defects were removed from VLT, two-photon absorption at wavelengths less than twice the UV band-edge would still cause a limitation to VLT in pulsed frequency conversion applications. Using the popular z-scan method,[83] simple two-photon absorption measurements can be made by translating a sample through the focus of an intense laser beam. Here, we examine the two-photon absorption of 532-nm radiation in VLT. The 532-nm radiation was generated by SHG from a 1.064- μm , 6-ps, 78 MHz, 9.5 W, modelocked laser using 9.5-mm-long and 20-mm-long VLT samples. Since the group-velocity walk-off for this process is approximately 0.7 ps/mm, the two different length gratings generate two different length SH pulses.[84] The two different pulse lengths allow us to distinguish whether the absorption measured is intensity or fluence dependent. A purely intensity-dependent absorption would indicate a true instantaneous two-photon absorption or a two-step

absorption with a time constant faster than the shortest pulse. However, if the absorption was a two-step absorption and had a time constant for the intermediate state that was larger than the time scale of the longest pulse, the absorption would be fluence dependent. Figure 3.22 shows the measured and theoretical absorption for the focussing and temporal pulse conditions. Note that for all experimental conditions the measured absorption is close to the theoretical expectations given a true, instantaneous, two-photon absorption cross-section, β_{TPA} , of 0.55 cm/GW. The absorptivity at 532 nm, α , at an intensity of I can be estimated by

$$\alpha = \beta_{\text{TPA}} I \quad (3.3)$$

Measurements of the two-photon absorption cross-section in lithium niobate have been previously measured as 0.38 cm/GW.[85] Although these values are on the same order as those of LT, it is expected that the two-photon absorption cross-section of LT should be smaller than LN because of the larger bandgap of LT compared to LN. It is unclear where the discrepancy between measured and literature values arises.

3.2.6 Ordinary-wave birefringence at 1- and 2- μm wavelengths

Since the largest nonlinear coefficient of LT is d_{33} (pertinent when all waves are polarized along the extraordinary-axis), the ordinary-wave refractive index is often ignored in measurements of the dispersion of LT. For the extraordinary-wave, Bruner et al. (Ref. [86]) have accurately measured the refractive index for near-stoichiometric LT. Bruner et al. have provided an accurate extraordinary-wave dispersion relation in the Sellmeier form (though slightly corrected in the 5-6 μm range by Ref. [87]). The ordinary-wave and extraordinary-wave refractive indices given by Nakamura et al. (Ref. [88]) are slightly inaccurate in the infrared as they do not include an infrared pole.

For certain applications, for example, an experiment in our laboratory with intracavity terahertz generation using a near-degenerate, type-II, synchronously pumped, picosecond optical parametric oscillator, use of the other nonlinear coefficients such as d_{24} or d_{31} is desired. For these interactions, an accurate wavelength-dependent

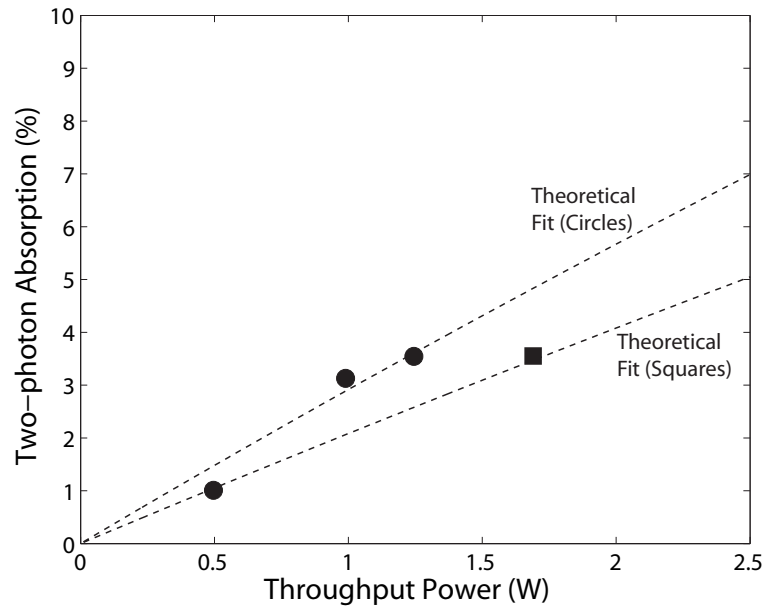


Figure 3.22: Two-photon absorption of a 532-nm wavelength beam focused to a spot of $10 \mu\text{m}$ in a VLT crystal of length 2 mm, as a function of the 532-nm average power. Peak intensity in the 78 MHz, 7-ps pulses can be calculated by multiplying the abscissa by $1.2 \times 10^9 \text{ 1/cm}^2$. The circles indicate data points using the 9.5-mm-long crystal that produces a 5-ps pulse of 532-nm light. The square indicates a two-photon absorption data point using the 20-mm-long crystal which produces a 10-ps pulse. The dashed lines indicate the theoretical expectations given a cross-section of 0.55 cm/GW .

Table 3.7: Birefringence and temperature coefficient at 1 and 2 μm

Wavelength [μm]	Birefringence ($n_o - n_e$)	$\frac{dn_o}{dT}$ [$1/(\text{°C})$]
1.064	2.55×10^{-3}	-3.27×10^{-5}
2.128	1.81×10^{-3}	-3.36×10^{-5}

ordinary-wave refractive index is required. To measure the birefringence at 1 and 2 μm , second harmonic generation using a near-degenerate, 1.064- μm pump was performed. By measuring the quasi-phaseshifting wavelengths of the d_{33} , d_{24} (the fundamental polarized along the ordinary and extraordinary axes and the second harmonic polarized along the ordinary axis) and d_{22} interactions as a function of temperature and quasi-phaseshifting period (as shown in Figure 3.23), the birefringence at the two wavelengths as a function of temperature could be estimated and is tabulated in Table 3.7.

3.3 Thermal Conductivity

As shown in Ref. [89], many of the limiting processes will be dependent on thermal dephasing. Since the steady-state temperature rise for a given absorbed power is inversely proportional to the thermal conductivity, and measurements indicate an increase in the thermal conductivity of melt-grown, near-stoichiometric LT compared to CLT,[28] it was important to measure the thermal conductivity of VLT as well.

In the laboratory of Prof. Takanori Taira from the Institute for Molecular Science, Laser Research Center in Okazaki, Japan, the thermal conductivity of different compositions of both LN and LT were measured by the quasi-1-D flash method.[90] A pulsed xenon lamp illuminates a metallized side of the sample under test. By measuring the temperature change at the opposite side as a function of time the thermal diffusivity can be obtained, and the thermal conductivity calculated according to

$$\kappa_{th} = \alpha_{th} \rho C_p \quad (3.4)$$

where κ_{th} is thermal conductivity, α_{th} is thermal diffusivity, ρ is the density and

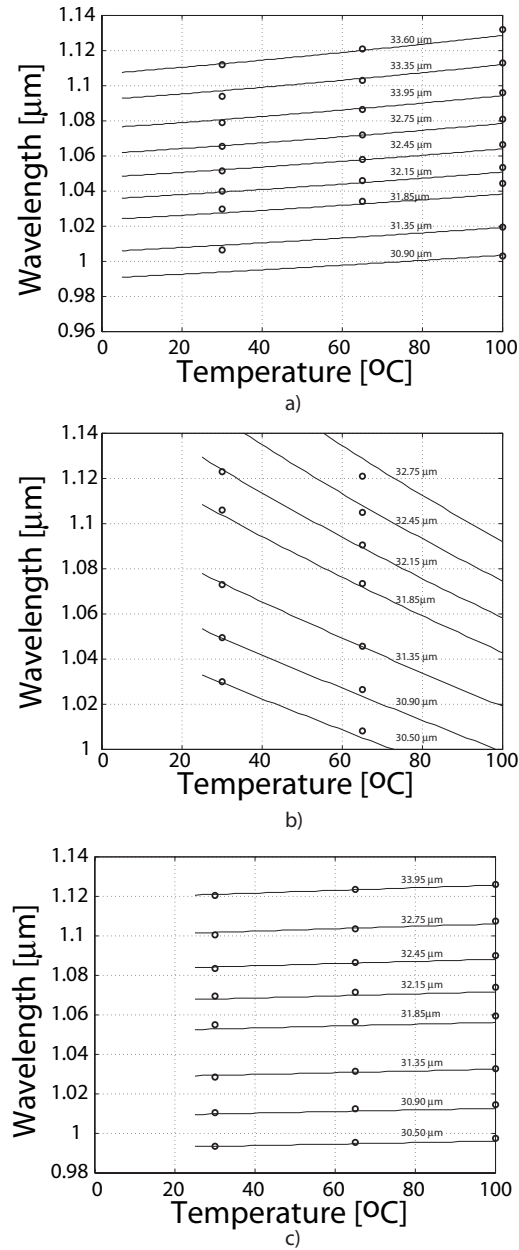


Figure 3.23: Quasi-phases matching wavelengths for interactions using the a) d_{33} , b) d_{24} and c) d_{22} nonlinear tensor components for quasi-phases matching periods from 29 to 32 μm in steps of 0.5 μm . The data points are shown by open circles and the solid lines are the theoretical quasi-phases matching wavelengths using the calculated birefringence. The extraordinary refractive index was taken from Ref. [86] and the birefringence and temperature dependence was fitted to the measured data.

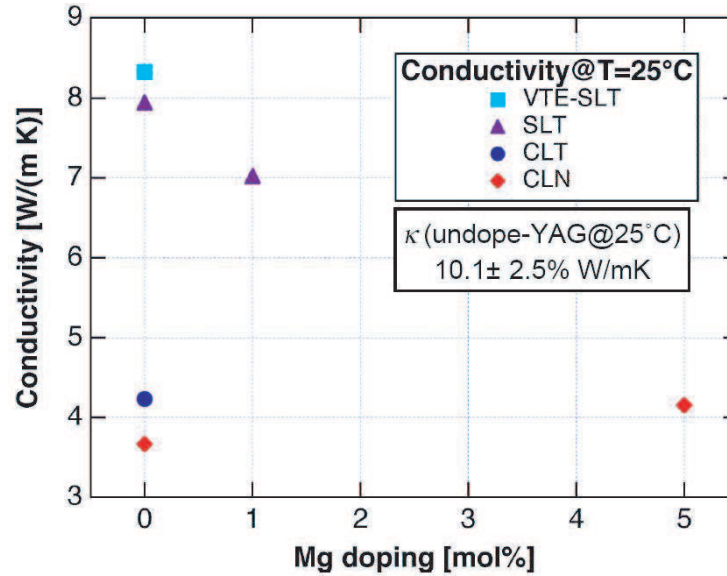


Figure 3.24: Room temperature thermal conductivities for various compositions of LN and LT.

C_p is the heat capacity. In this experiment, 10 mm \times 10 mm \times 1 mm samples of z-cut wafers were prepared for thermal conductivity measurement. Two layers are deposited, a thin gold layer followed by a thin carbon layer, on both sides of the transparent material to enable accurate measurement of the thermal conductivity via the flash method. The carbon layers provide both a uniform absorbing layer for the xenon lamp and a uniform black body radiator for the measuring pyrometer. The gold layers prevent direct black body radiation through the transparent material from carbon layer to carbon layer. Using this technique, accurate measurements of the thermal conductivity along the extraordinary-axis were performed as a function of temperature. Figure 3.24 shows the thermal conductivity of congruent-composition LN (Yamaju Ceramics), 5% magnesium-doped LN (Yamaju Ceramics), undoped double-crucible Czochralski-grown near-stoichiometric LT (Oxide Corporation), 1% magnesium-doped double-crucible Czochralski-grown near-stoichiometric LT (Oxide Corporation), congruent-composition LT (Yamaju Ceramics) and VLT. It is clear to see that VLT has nearly a 2-fold increase in thermal conductivity compared to its congruent-composition counterpart, 8.3 W/(mK) versus 4.2 W/(mK).

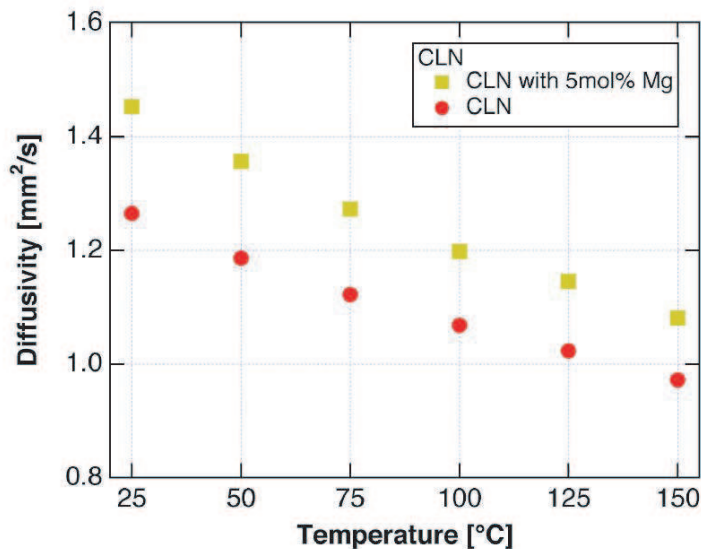


Figure 3.25: Temperature dependence of the thermal diffusivity of LN.

Melt-grown near-stoichiometric LT also shows significant enhancement of the thermal conductivity for both magnesium-doped and undoped crystals. These measurements are consistent with previous measurements in Ref. [28]. Figures 3.25 and 3.26 show the temperature dependence of the thermal diffusivity of the LN compositions and LT compositions, respectively. For all compositions tested, at 150 °C, the thermal diffusivity falls to approximately 60 % of the measured room-temperature value.

To ensure the accuracy of this measurement, the result of which was somewhat surprising, a second method was employed to measure the thermal conductivity. Using the common-path photothermal interferometer apparatus used to measure absorption coefficients in Section 3.2.3, one can estimate the relative thermal conductivity along the axis that is normal to the plane of crossing of the pump and probe beams by monitoring the phase of the modulation induced on the probe signal relative to the modulation on the pump intensity. The phase (ϕ) depends on the time it takes the thermal wave to diffuse across the beam and is approximately given by

$$\phi = \arctan(\omega\tau_{\text{therm}}) \quad (3.5)$$

where ω is the measurement chopper frequency and $\tau_{\text{therm}} \propto 1/\kappa_{th}$ is the thermal

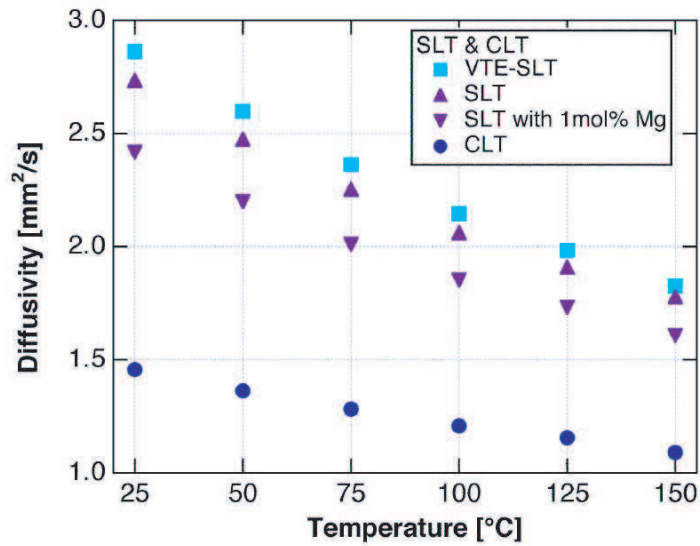


Figure 3.26: Temperature dependence of the thermal diffusivity of LT.

diffusion time. By this method, the thermal conductivity of VLT was compared to the thermal conductivity of CLT for both the extraordinary axis and the ordinary axis at room temperature. For both axes, the thermal conductivity was greater in VLT than in CLT. The extraordinary-axis thermal conductivity increased by a factor of $2 \pm 20\%$ and the ordinary-axis thermal conductivity increased by a factor of $1.3 \pm 10\%$. The excess noise along the extraordinary axis stems from pyroelectric contributions which are integrated out during the ordinary axis measurement. These measurements are, however, consistent with the measurements taken using the quasi-1D flash method and confirm the 2-fold increase in thermal conductivity.

Chapter 4

Conventional z-cut Bulk Devices

After characterization of the material properties, it is necessary to verify the utility of VLT for frequency conversion applications. Since visible generation at watt-level average powers at near room temperature is nearly impossible with congruently melting composition crystals, the focus of these experiments will be to show that efficient, practical and stable visible generation is possible at near room temperatures in VLT.

4.1 Generation of 532-nm radiation by SHG

The widespread use of diode-pumped solid-state lasers has enabled practical and efficient nonlinear optical devices. Neodymium-doped yttrium aluminium garnet ($\text{Nd:Y}_3\text{Al}_5\text{O}_{12}$, Nd:YAG) has been perhaps the most studied of all the solid-state gain media and is used in laser sources that are convenient pumps for visible generation by nonlinear optics. With the peak laser emission at $1.064 \mu\text{m}$, a second harmonic generation experiment will produce 532-nm radiation, a green near the peak of the sensitivity of the human eye.

Preliminary tests of the nonlinear optical performance of VLT were performed with a 17-mm-long, 8-mm-period, VLT crystal designed for SHG of 532-nm radiation. Focusing 18 W of single-frequency 1064-nm CW radiation to a spot of $34\text{-}\mu\text{m}$ ($1/e^2$ -intensity radius) into the crystal, 1.6 W of 532-nm radiation was produced at a

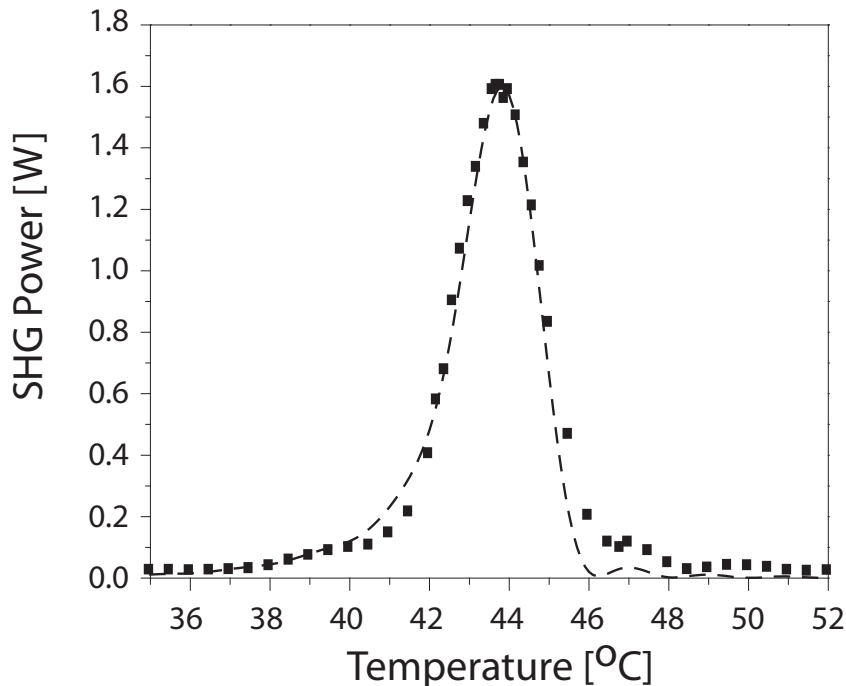


Figure 4.1: Temperature tuning curve for SHG of 532-nm radiation in a 17-mm-long, 8- μ m-period VLT. Here, 18 W of 1064-nm radiation was used to generate 1.6 W of 532-nm radiation. Experimental points and theoretical predictions are plotted.

temperature of 43.3 °C, corresponding to a normalized efficiency of 0.3%/W-cm, compared to a theoretical value of approximately 1%/W-cm, with the difference consistent with the non-ideal duty cycle of the QPM grating. Figure 4.1 shows experimental and theoretical tuning curves for the SH power as a function of temperature. The asymmetry of the curve is a results of the near-confocal focussing of the pump beam. The near-ideal tuning behavior indicates homogeneity of the refractive index of the crystal over the 17-mm-length of the sample.

To explore the limits of the lifetime of this material a long-term test has been performed. To explore long-term aging effects, we measured the SH power over a 1000-hour interval using a pulsed 1064-nm pump laser which delivers 150-ns pulses

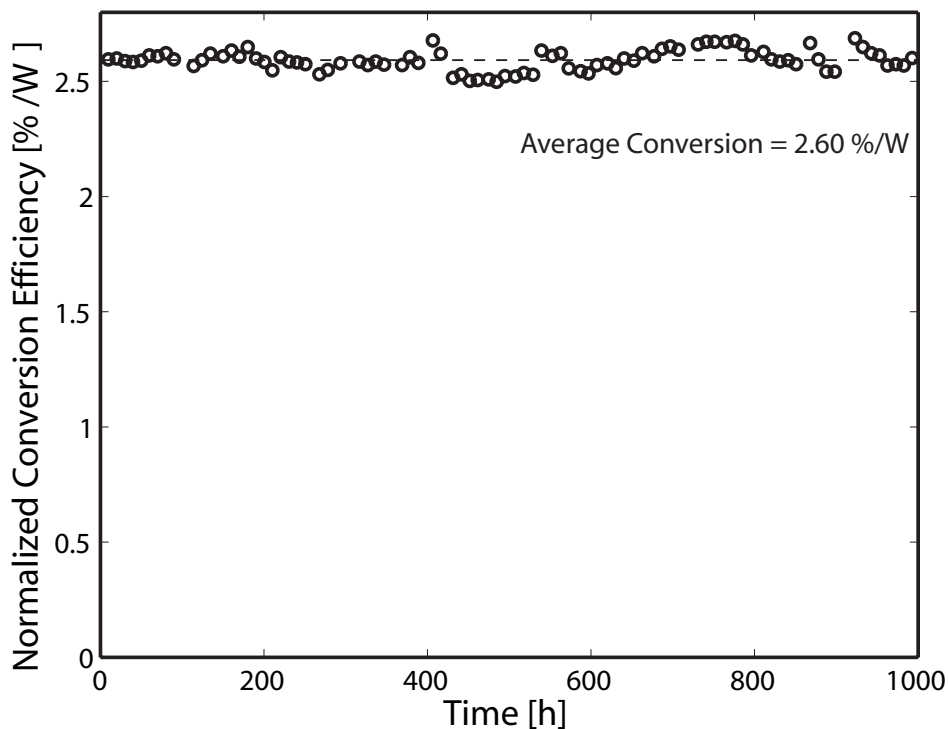


Figure 4.2: Conversion efficiency as a function of time for the 1000-hr test of the generation of 532-nm radiation by SHG. In this experiment, a 17-mm-long VLT crystal generated 5 W of average power at 532 nm with approximately 15 W of 1064-nm radiation. The 1064-nm laser had a repetition rate of 100 kHz and the pulses generated were 150 ns long. No degradation was observed over the life time of this test.

at a repetition rate of 100 kHz with an average power of 15 W. The pump laser was focused to a $120\text{-}\mu\text{m}$ spot size ($1/e^2$ -intensity radius) and produced 5 W of SH. Figure 4.2 shows the efficiency of the SH process; this efficiency does not change measurably over the 1000-hr test period, indicating that aging is negligible. This test verifies the resistance to photorefractive damage near room temperature as characterized in Section 1.4.1. Moreover, the high peak intensities ($\sim 4.5\text{ MW/cm}^2$) showed that GRIIRA was not a limiting characteristic for this experiment

After the verifying the photorefractive damage resistance, a high-power CW experiment was performed to verify the average-power handling of VLT. An uncoated, 4-cm-long, $8\text{-}\mu\text{m}$ -period device was used to generate the second harmonic of the output

of a CW, 36-W, 4-stage master-oscillator power-amplifier 1064-nm Nd:YAG source. The source had an M-squared value of 1.2 at 36 W and was focussed to a 40- μm spot ($1/e^2$ -intensity radius) into the crystal. The 4-cm-long crystal generated 10.5 W of 532-nm SHG internally at the maximum pump power of 29 W internal and shows no signs of photorefractive damage or absorption limitations as shown in Figure 4.3. Also shown in Figure 4.3 is the optimum set point of the temperature controller. The linear decrease in optimal set point as a function of pump power suggests that linear absorption of the fundamental dominates this change. A temperature tuning curve at maximum pump power was measured and is in good agreement with theoretical expectations as shown in Figure 4.4. The M-squared value of the SHG radiation was measured to be 1.13 at 10.5 W of 532-nm radiation. The low-power, normalized efficiency of 0.4 $\%/(W\text{cm})$ is approximately a factor of 2 smaller than ideal for the focussing conditions. Poling duty-cycle can account for the discrepancy. Non-uniformity of the crystal composition across the wafer (as measured in Section 3.1.1) does not seem to be the limiting factor in the device performance. Further improvements in periodic poling and lithography will improve overall nonlinear device performance.

From the SHG measurements, it is likely that the maximum CW SHG power will be limited by the thermal dephasing which results from absorption of the 1064 nm radiation. Using a value of 6.7 W/(mK), the geometric mean of the values measured for the thermal conductivity along the z-axis and the normal to it in Section 3.3, as an approximate value for the thermal conductivity one can estimate the maximum CW power for a given crystal length and absorption losses as in Ref. [76]. A 0.5-cm-long crystal with linear and induced 1064-nm absorptions of 0.1 $\%/cm$ and 0.02 $\%/(W\text{cm})$, the maximum CW power is 165 W limited by thermal dephasing. This maximum could be increased by reducing the absorption in VLT crystals. Reducing the absorption would require either reducing the extrinsic impurity concentration during the growth process or improving the VTE or poling process to change the charge state of the existing defects so they absorb less in the wavelength band of interest.

To test the efficiency of these devices with short pulses and higher peak intensities,

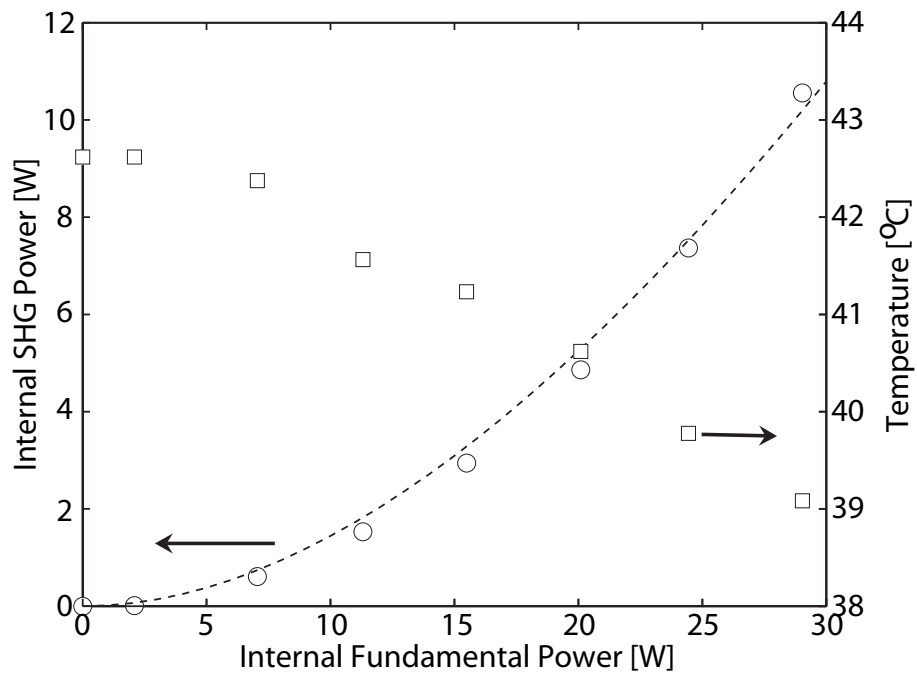


Figure 4.3: Internal 532-nm SHG power (circles) and optimum controller set point temperature (squares) versus internal 1064-nm power. The VLT device used in this experiment was 4 cm long. The dotted line is a \tanh^2 fit to the internal SHG power as a function of input fundamental power.

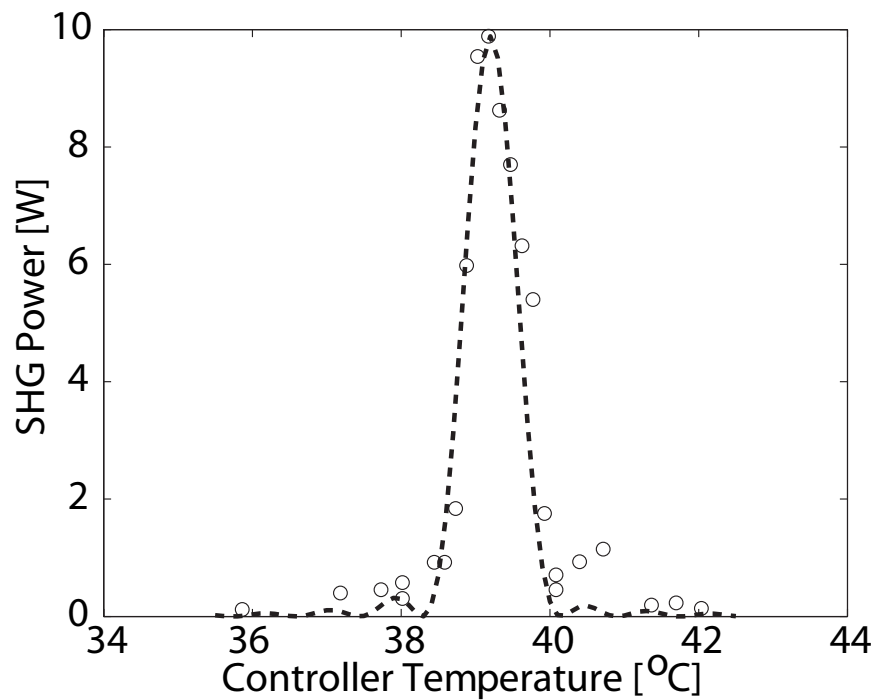


Figure 4.4: 532-nm SHG power versus temperature controller set point. The dotted line is the theoretical temperature tuning curve for the experimental focussing conditions. The 4-cm-long device generated approximately 10 W of 532-nm radiation from approximately 28 W of 1064-nm radiation.

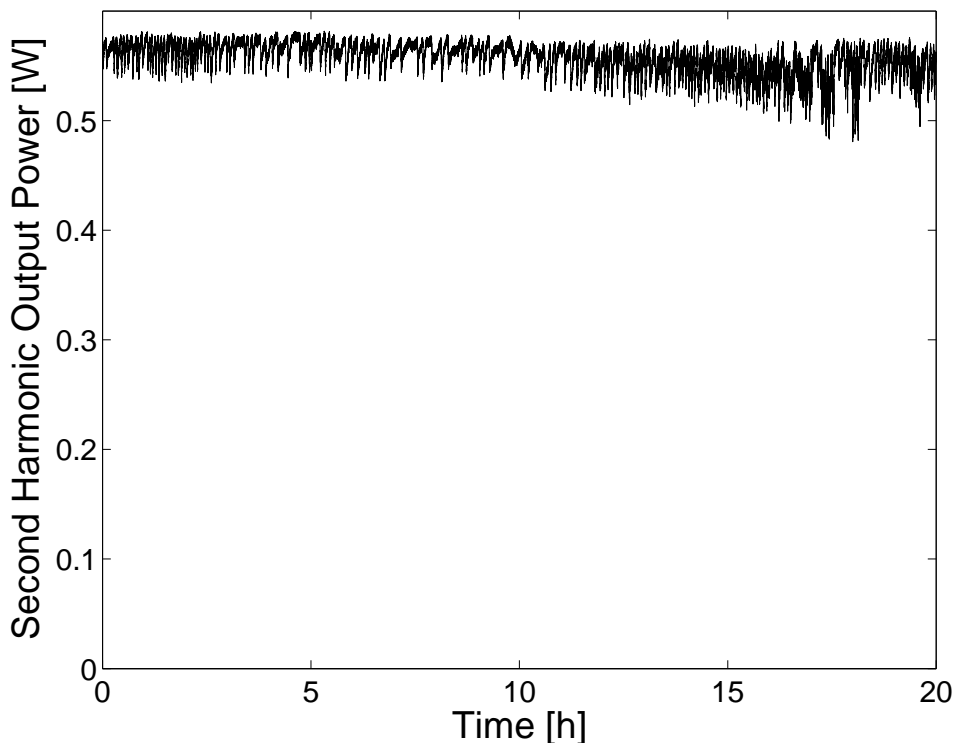


Figure 4.5: 532-nm SHG output power as a function of time for the high peak intensity experiment. Over 20 hours, peak output power did not significantly change. The output power noise is consistent with the observed input laser noise. The pump laser used was a 1.8-W average-power, 24-ps, passively modelocked, ceramic Nd:YAG laser.

a 1.8 W, passively modelocked, ceramic Nd:YAG laser was used. This laser had a repetition rate of 78 MHz and generated pulses had a pulse width of 24 ps. Using a 12-mm-long grating with an $13\text{-}\mu\text{m}$ spot size ($1/e^2$ -intensity radius), 550 mW of 532-nm radiation was produced with good stability over 24 hrs with tuning curve characteristics as shown in Figures 4.5 and 4.6. The peak intensities at $1.064\text{-}\mu\text{m}$ for this experimental setup exceeded 350 MW/cm^2 and still the SHG output power showed no roll-off due to photorefraction or GRIIRA.

Finally, a 9.5-W, 6-ps, modelocked, $1.064\text{-}\mu\text{m}$ laser was used to generate 2.7 watts and 4.2 watts of SHG using a 9.5-mm-long grating and a 20-mm-long grating respectively. The repetition rate of the pump laser was 75 MHz and was focussed to

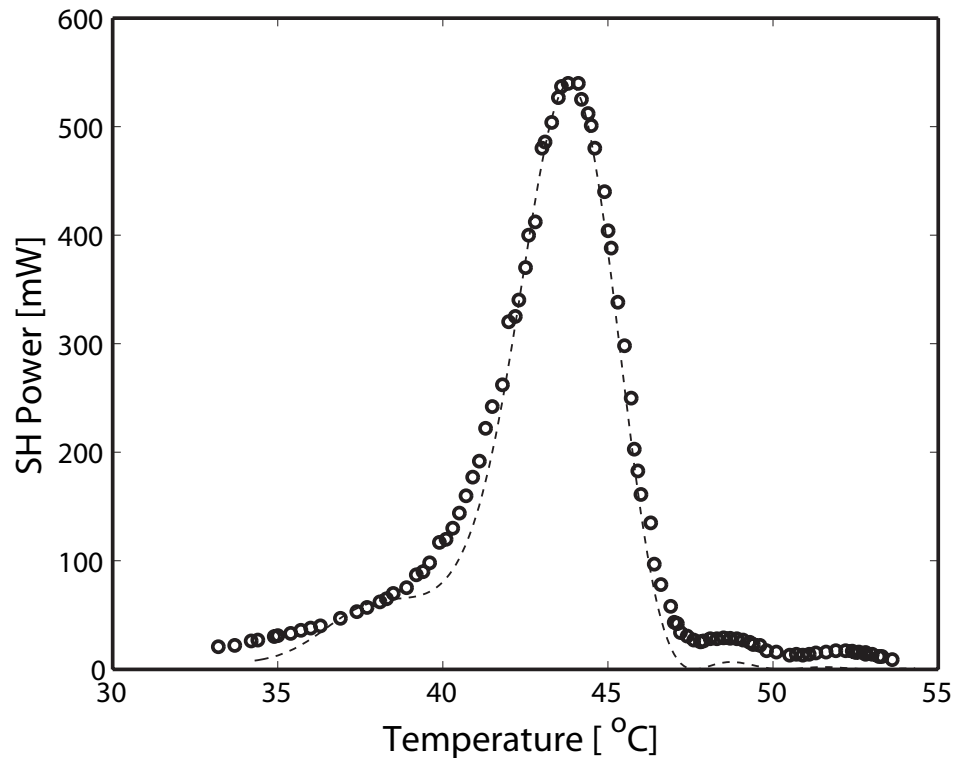


Figure 4.6: Temperature tuning curve for the generation of 532-nm radiation by SHG using a 12-mm-long grating with extremely tight focussing ($11\text{-}\mu\text{m}$ $1/e^2$ -intensity radius). The pump laser used was a 1.8-W average-power, 24-ps, passively modelocked, ceramic Nd:YAG laser.

a 120- μm spot size ($1/e^2$ -intensity radius). Here the peak intensities of the 532-nm radiation exceeded 50 MW/cm² and no apparent photorefractive, thermal, or laser-induced damage was observed.

It is clear from the experiments of generation of 532-nm radiation, That VLT is a suitable, efficient, frequency conversion material for multi-watt generation of green light.

4.2 Generation of 589-nm radiation

Recently, interest in generation of 589-nm radiation for adaptive optic and medical applications has increased.[91] Astronomers using ground-based telescopes at visible and near-infrared wavelengths wish to use adaptive optic techniques to remove the atmospheric aberrations during observation. To correct for these aberrations, a reference star positioned close to the observation star must provide enough light to a wavefront sensor. To provide a suitable reference, a laser can be used to excite a particular fluorescent species that sits atop the turbulent atmosphere. The wavefront distortion of the return radiation from the fluorescent species is then detected and corrected using a deformable mirror.

One of these techniques involves exciting the sodium layer which sits 90 km above the earth using 589-nm radiation. This laser guide star (LGS) system requires approximately 5 W of 589-nm radiation within a laser linewidth of 1 GHz (matched to the doppler broadened bandwidth of the sodium layer) to provide enough return light to the wavefront sensor for adequate performance.

To meet these requirements, there are several possible sources at 589 nm. The most well-developed solution is a simple dye laser which is pumped at 532 nm. Dye lasers are usually undesirable because the lasers are quite expensive to build and maintain and the dyes themselves are often carcinogenic. Furthermore, the dyes are extremely flammable and require expensive fire-proof enclosures.

Nonlinear optics may provide less expensive and more practical solutions to the LGS problem. Recently several schemes to produce 589-nm radiation from available solid-state and fiber sources have been proposed. Sum frequency generation from two

Nd:YAG emission lines, 1.064 μm and 1.319 μm , has been used by Denman et al to produce 50 W of 589-nm radiation in a doubly resonant cavity using lithium triborate (LBO).[92] Sum frequency generation from two fiber sources, the 938-nm line of Nd-doped silica glass and 1583-nm radiation from a Er-doped silica fiber have been summed by Dawson and co-workers at Lawrence Livermore using KTP and LT.[93] Second harmonic generation from an 1178-nm Raman-amplified laser has produced 3 W of 589-nm radiation in melt-grown MgO-doped LT.[94] Finally, second harmonic generation using a 1178-nm bismuth doped fiber laser has been proposed.[95] No matter what nonlinear interaction becomes the most efficient and inexpensive alternative, the nonlinear optical material can be chosen independently.

To explore the practicality of VLT for these interactions, different sets of grating periods were produced to provide all the different proposals the correct quasi-phasematching.

First, generation of 589-nm radiation was performed by SFG of 938 nm and 1583 nm. Low power characterization of a 4.5-cm-long, 11.2- μm -period device was performed using a long-band, CW Ti:sapphire lasing at 938-nm and a tunable, amplified, external-cavity diode laser (ECDL). The ECDL was tuned over a range limited to 1566-1570 nm to stay within the amplification bandwidth of Er:silica, to be consistent with future systems experiments. The Ti:sapphire laser was focussed to 65- μm spot size ($1/e^2$ -intensity radius) and the ECDL was focused to a 110- μm spot size ($1/e^2$ -intensity radius). Measured low power conversion efficiency was 3 %/W, a factor of 3 from the ideal efficiency. Figure 4.7 shows the measured low power tuning curve at 31 °C.

This same device was characterized in an experiment carried out in conjunction with Lawrence Livermore National Laboratory for testing with higher powers. Using a 938-nm Nd-doped fiber laser and an amplified 1583-nm Er-doped fiber laser, generation of 1.38 watts of 589-nm radiation was achieved with an efficiency of 3 %/W. The results are shown in Figure 4.8. Again, no photorefractive or thermal limitations were observed.

A second set of quasi-phasematching periods were periodically poled for SHG of 589-nm. A 3.5-cm-long, 10.65- μm -period device was used in conjunction with

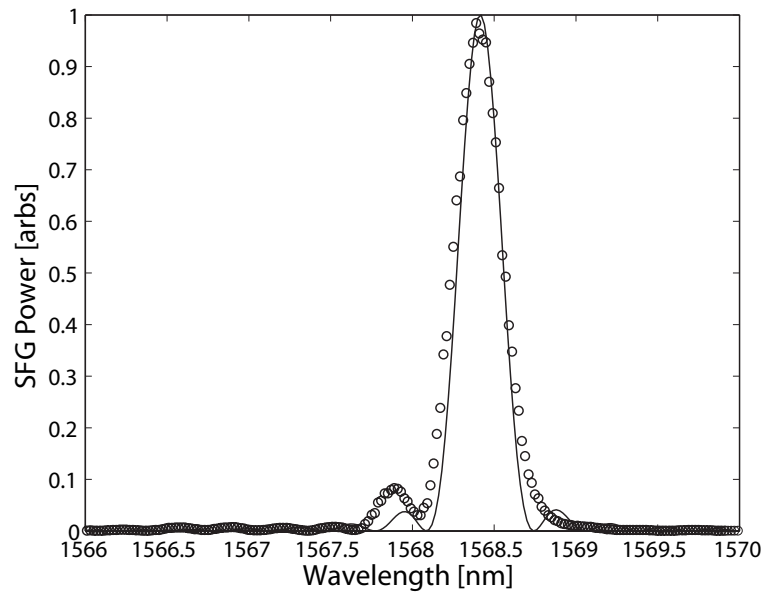


Figure 4.7: Wavelength tuning curve for the generation of ~ 589 -nm radiation by SFG of 938-nm and 1566-nm radiation using a 4.5-cm-long, $11.2\text{-}\mu\text{m}$ grating. The open circles are measured data points and the solid curve is the theoretically expected tuning curve.

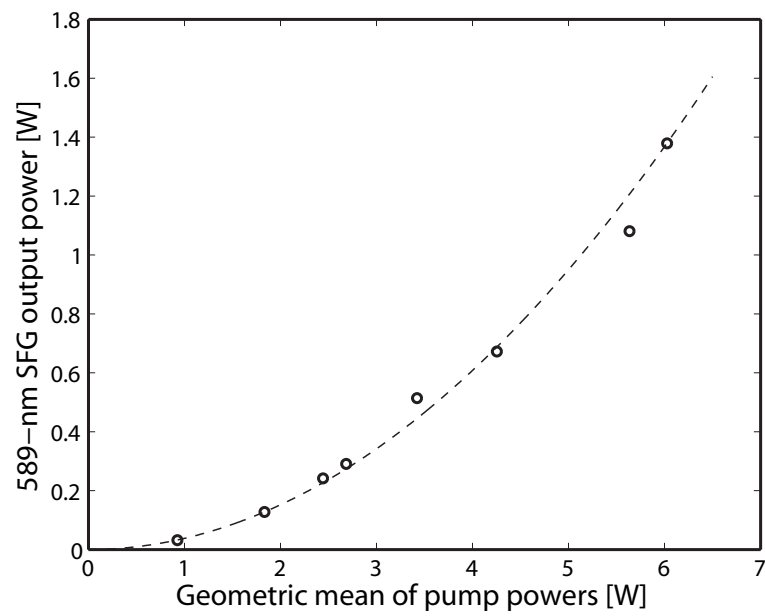


Figure 4.8: Generated 589-nm power as a function of input powers. The 589-nm radiation was generated by summing a 7-W, CW, 1583-nm, Er-doped fiber laser and a 7-W, CW, 938-nm, Nd-doped fiber laser in a 4.5-cm-long, 11.2- μm -period VLT device.

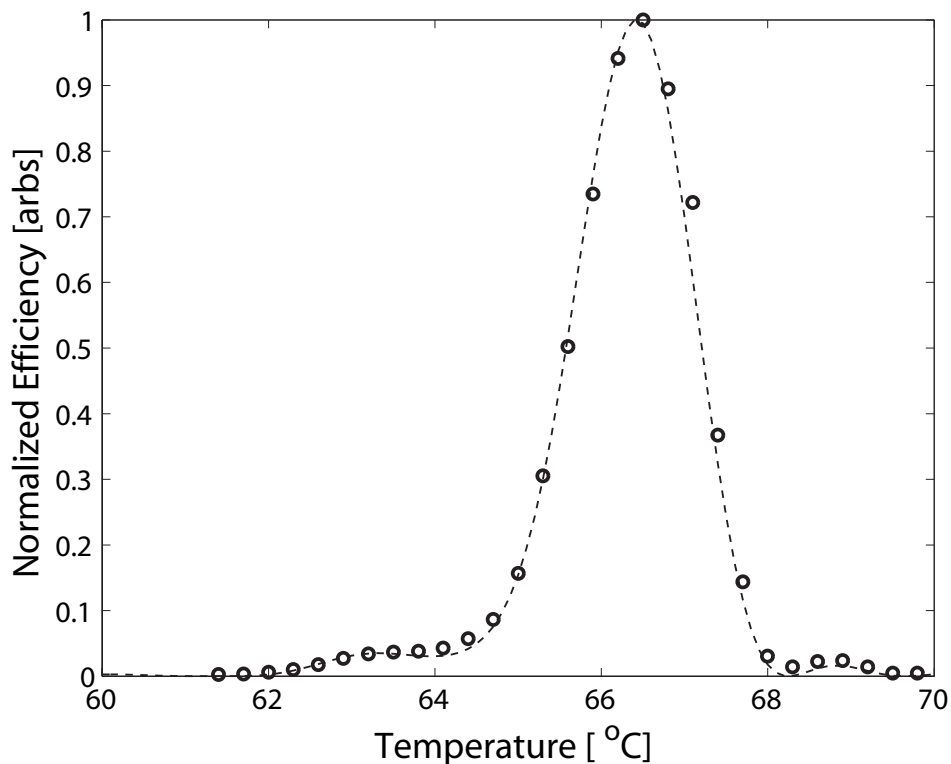


Figure 4.9: Temperature tuning curve for the generation of 589-nm radiation by SHG of a 1178-nm fiber laser using a 3.5-cm-long, $10.65\text{-}\mu\text{m}$ grating. The open circles are measured data points and the solid curve is the theoretically expected tuning curve for a grating of only 3.0 cm long.

an 1178-nm, Raman-amplified, master-oscillator power-amplifier system. Low power characterization of the device resulted in the temperature tuning curve that is shown in Figure 4.9. The tuning curve was not ideal for the nominal 3.5-cm-length grating, but fit well with a grating that was only 3.0 cm long. Merged domains toward the ends of the device can account for the discrepancy. The measured low-power conversion efficiency was $2\ \%/W$, and is less than a factor of 2 below the theoretical efficiency of a 3.5-cm-long device, and within a factor of 1.5 for a 3-cm effective length device.

At higher powers, the Raman-amplified source broadened in linewidth and reduced the measured efficiency. As shown in Figure 4.10, the maximum output power reached 3.25 watts of 589-nm radiation from 20 W of 1178-nm radiation. The expected output for a source with the required 1-GHz-linewidth source would have been greater than

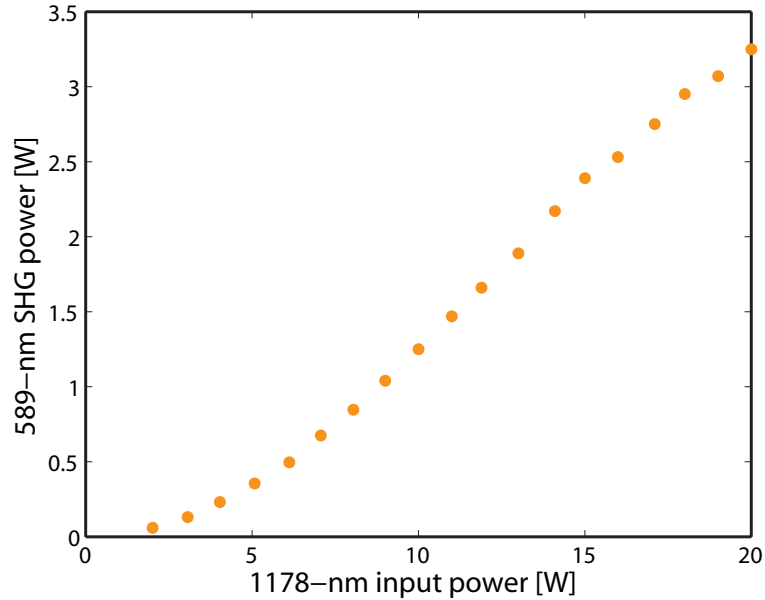


Figure 4.10: SHG power at 589 nm as a function of 1178-nm input power generated in a 3.5-cm-long, 10.64- μm grating. The roll-off in efficiency is attributed to the dramatic increase in pump linewidth as a function of pump power, exceeding the QPM bandwidth of the crystal.

6 watts from 20 W of 1178-nm radiation. Unfortunately, the self-convolution of the electric field of the Raman-amplified source attained a linewidth in excess of 55 GHz which reduced the efficiency by a factor of 2. At the observed 3.25 W of 589-nm radiation, photorefraction and thermal limitations were not observed in the nonlinear device.

Finally, in collaboration with Lockheed Martin - Coherent Technologies, Inc., generation of 589-nm radiation by SFG was performed with a 36-mm-long sample. Using two 77-MHz-repetition-rate, modelocked Nd:YAG lasers, 8.7 W of 589-nm radiation was produced with 16 W of 1064-nm radiation and 9.1 W of 1319-nm radiation. The pulse width of the 1064-nm laser was 0.6 ns and was focussed to a 43- μm spot ($1/e^2$ -intensity-radius). The pulse width of the 1319-nm laser was 0.4 ns and was focussed to a 50 μm spot ($1/e^2$ -intensity-radius). The optimum phasematching temperature was 80.9 $^{\circ}\text{C}$ for a quasi-phasematching period of 10.8 μm and showed no photorefractive damage.

In these experiments, a maximum of 8.7 W of 589-nm radiation was generated without photorefractive damage. This power level is suitable for laser guide star applications requiring a single reference star. At this power level, VLT can be an efficient frequency conversion material for the generation of 589-nm radiation.

4.3 Generation of 458.3-nm radiation by SHG

Argon-ion lasers have multiple emission lines including lines located at 457.9 and 488 nm. To replace the argon-ion lasers with compact and efficient solid-state lasers that conveniently lase at wavelengths close to 915 nm (912 nm for Nd:GdVO₄ and 914 nm for Nd:YVO₄), combined with efficient nonlinear devices that have long lifetimes are required. Moreover, blue lasers with wavelengths ranging from 457 nm to 460 nm have garnered interest for application to laser display technology.[96]

To examine the feasibility of generation of shorter wavelengths, quasi-phasematching periods as short as 4.9 μm were poled. A tunable, CW, Ti:sapphire was used to generate wavelengths suitable for SHG devices generating around 455 nm to 458.5 nm at near room temperature. With 90 mW of pump power, a maximum power of 60 μW was produced internally. The conversion efficiency of 0.5 %/(Wcm) is approximately a factor of 2 from ideal for the 1.5-cm-long device for the focussing conditions. The measured temperature tuning curve is shown in Figure 4.11. Photorefractive was not observed at these power levels; these devices should be examined at higher average and peak powers to verify the photorefractive damage resistance and the resistance to blue-induced infrared absorption.

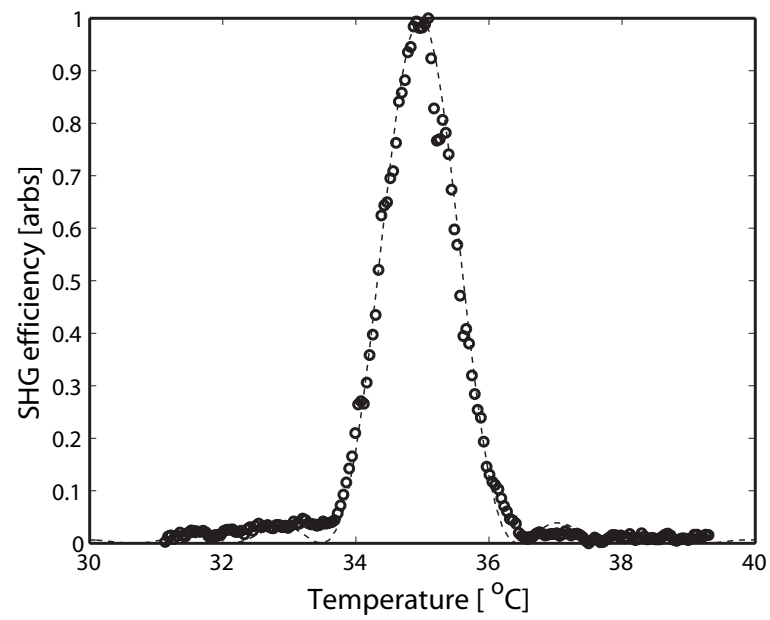


Figure 4.11: Temperature tuning curve of a 1.5-cm-long device generating 458.3 nm by SHG. Measured data (circles) match well with the theoretical curve (dashed line).

Chapter 5

Rotated cut bulk devices

5.1 Motivation

As discussed in Section 1.4, PRD and GRIIRA have been the two most prevalent material limitations for widespread application of frequency conversion using quasi-phasematched lithium tantalate. In comparison, birefringently phasematched nonlinear devices have dominated most of the applications for frequency conversion. However, the measurements of the PRD and GRIIRA properties in Chapter 3 show that these two material limitations can be avoided by appropriate composition control. Practical devices using periodically poled ferroelectrics for frequency conversion applications appear to be achievable.

However, in certain applications, birefringently phasematched materials may still be advantageous. In particular, periodically-poled ferroelectrics have limited apertures compared to birefringently phase-matched crystals. Large-aperture crystals are necessary to avoid surface damage threshold with high peak-power pumps. Crystal thickness of periodically poled CLT is limited to approximately 1 mm because of the high applied electric field required for the periodic poling process. Without focussing optics required to form elliptical pump beams, the thickness limits the available aperture to an area of approximately 1 mm². Previous efforts to increase aperture include PP thick substrates (~ 5 mm) of lower coercive field ferroelectrics such as magnesium-oxide-doped lithium niobate [97] and diffusion bonding unpoled lithium niobate to

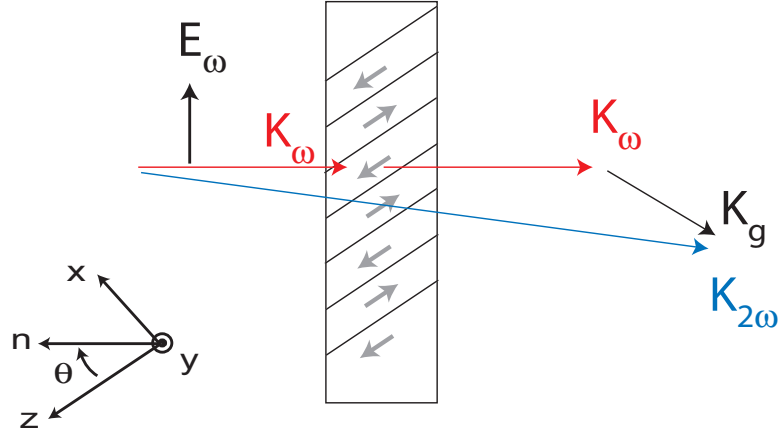


Figure 5.1: Topology for large aperture periodically poled crystals. Light propagates through the large wafer face and has a component of the electric field polarized along the z-axis enabling efficient second harmonic generation (SHG) among other nonlinear interactions.

PP lithium niobate.[98]

As an alternative, a topology based upon rotated-cut ferroelectrics may provide scalable apertures as depicted in Figure 5.1. The key to this approach is to pole a rotated-cut crystal, so that the domain walls are not perpendicular to the surface of the crystal. Light incident on the large wafer surface can be polarized with a component along the extraordinary-axis to use the largest nonlinear coefficient and make use of a geometrical projection of the grating k-vector for QPM. In this chapter, we will discuss the theoretical expectations for rotated-cut devices, fabrication details, and experimental results for generation of 532-nm radiation by SHG using devices based on 25-degree-rotated, X-cut VLT.

5.2 Theory of rotated-cut bulk devices

The discussion of the theoretical expectations for rotated-cut devices will start with the angular behavior of the fundamental wave inside the QPM medium with a period Λ . We assume an input wave with intensity I_{FH} is **p**-polarized to enable a component of the electric field to be polarized along the extraordinary-axis of the ferroelectric, as

well as to take advantage of the lower reflectivities for angles of incidence approaching Brewster's angle. We also assume that the birefringence of the ferroelectric is such that only the extraordinary waves are sufficiently close to phasematching to participate in the conversion process. Finally, we examine the situation where the fundamental wave refracts toward the QPM grating wavevector. Figure 5.2 shows the input face of a rotated-cut QPM device.

The fundamental wave is incident on the crystal at an angle θ_i and propagates at an angle θ_{FH} inside the crystal (with a refractive index of n_{FH} and a power transmission of T_{FH} given by electromagnetic wave theory).

$$\sin \theta_{\text{FH}} = \frac{\sin \theta_i}{n_{\text{FH}}} \quad (5.1)$$

$$T_{\text{FH}} = 1 - \left(\frac{n_{\text{FH}} \cos \theta_i - \cos \theta_{\text{FH}}}{n_{\text{FH}} \cos \theta_i + \cos \theta_{\text{FH}}} \right)^2 \quad (5.2)$$

The crystal rotation indicated by θ_R is the rotation of the ordinary axis of the crystal with respect to the surface normal. Thus, the extraordinary axis is rotated by an angle $\theta_z = 90 - \theta_R$. If the ferroelectric is periodically poled for first-order QPM, the SH will propagate at an angle θ_{SH} given by the sum of the wavevectors as shown in Figure 5.3 and the wavevector mismatch Δk .

To satisfy the required boundary conditions at the interfaces (similar to the considerations leading to Snell's law in linear optics), [75, 34] the transverse wave-vectors must follow

$$\begin{aligned} K_{2\omega, u} &= 2K_{\omega, u} + K_{g, u} \\ \frac{4\pi}{\lambda_{\text{FH}}} n_{\text{SH}} \sin \theta_{\text{SH}} &= \frac{4\pi}{\lambda_{\text{FH}}} n_{\text{FH}} \sin \theta_{\text{FH}} + \frac{2\pi}{\Lambda} \sin \theta_R \end{aligned} \quad (5.3)$$

where coordinates u and v are defined in Figure 5.3, and the second form follows from the first by the geometry in the figure and trigonometry. The phasemismatch is then given by the difference in wave-vectors along v , so that

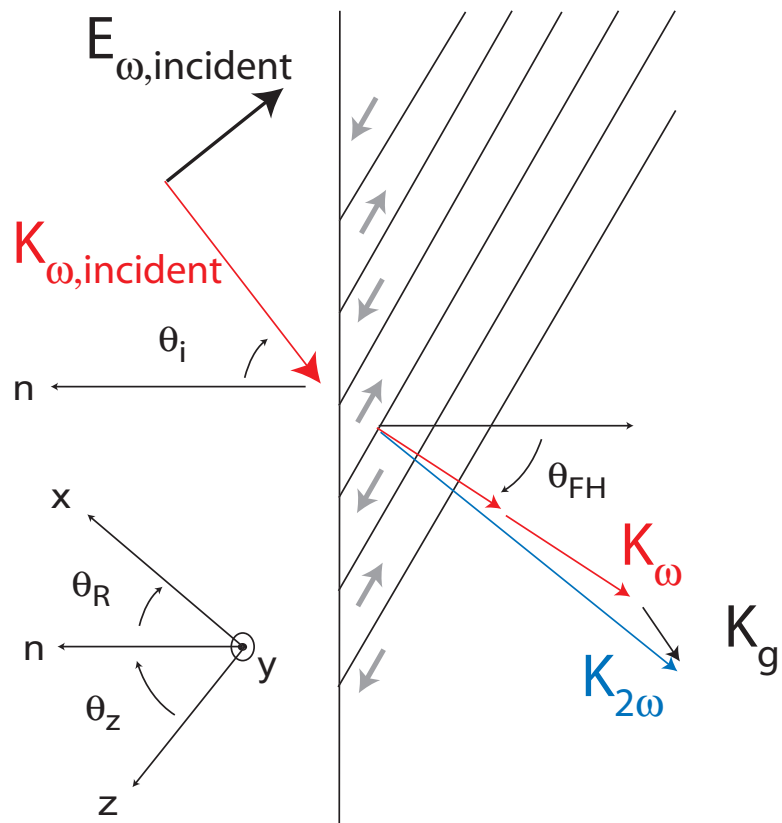


Figure 5.2: Schematic of SHG in rotated-cut, periodically poled ferroelectric

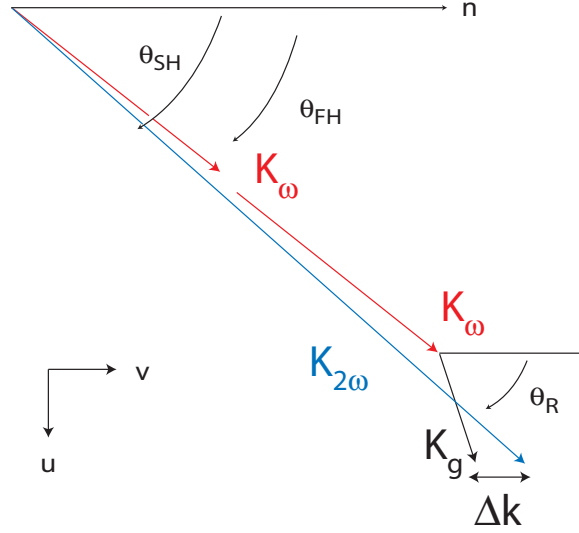


Figure 5.3: Wave-vector diagram of the SHG process with a noncollinear QPM process.

$$\begin{aligned}
 \Delta k &= K_{2\omega,v} - (2K_{\omega,v} + K_{g,v}) \\
 &= \frac{4\pi}{\lambda_{\text{FH}}} n_{\text{SH}} \cos \theta_{\text{SH}} - \left(\frac{4\pi}{\lambda_{\text{FH}}} n_{\text{FH}} \cos \theta_{\text{FH}} + \frac{2\pi}{\Lambda} \cos \theta_{\text{R}} \right) \quad (5.4)
 \end{aligned}$$

For a rotated-cut device of thickness L , the undepleted-pump, external efficiency of SHG, η_{rot} , can be calculated similarly to Ref. [75] and is given by

$$\begin{aligned}
 \eta_{\text{rot}} &= \eta_{\text{nor}} T_{\text{FH}} T_{\text{SH}} \cos^2 (\theta_{\text{R}} - \theta_{\text{FH}}) I_1 \frac{L^2}{\cos^2 \theta_{\text{SH}}} \text{sinc}^2 \left(\frac{\Delta k L}{2} \right) \\
 &= \eta_{\text{nor}} T_{\text{FH}} T_{\text{SH}} \cos^2 (\theta_{\text{R}} - \theta_{\text{FH}}) I_1 \frac{L^2}{\cos^2 \theta_{\text{SH}}} \text{sinc}^2 (\Psi) \quad (5.5)
 \end{aligned}$$

where T_{SH} is the power transmission of the second harmonic and Ψ is the total wave-vector mismatch given by

$$\sin \theta_{\text{SH}} = \frac{\sin \theta_{\text{exit}}}{n_{\text{SH}}} \quad (5.6)$$

$$T_{\text{SH}} = 1 - \left(\frac{n_{\text{SH}} \cos \theta_{\text{exit}} - \cos \theta_{\text{SH}}}{n_{\text{SH}} \cos \theta_{\text{exit}} + \cos \theta_{\text{SH}}} \right)^2 \quad (5.7)$$

$$\Psi = \frac{2\pi L}{\lambda_{\text{FH}}} \left(n_{\text{SH}} \cos \theta_{\text{SH}} - n_{\text{FH}} \cos \theta_{\text{FH}} - \frac{\lambda_{\text{FH}}}{2\Lambda} \cos \theta_{\text{R}} \right) \quad (5.8)$$

With focussed gaussian beams, the efficiency is nearly the same. For this situation, we parameterize the input fundamental as being focussed to spot size of w ($1/e^2$ -intensity radius), having a pulse width of τ ($1/e^2$ -intensity radius), and a peak fluence per pulse F . The conversion efficiency for the undepleted-pump case given the above parameters is given by

$$\eta_{\text{rot}} = \eta_{\text{nor}} T_{\text{FH}} T_{\text{SH}} \cos^2(\theta_{\text{R}} - \theta_{\text{FH}}) \frac{F}{C\tau} \cos^2(\theta_i) \frac{L^2}{\cos^2 \theta_{\text{SH}}} \text{sinc}^2(\Psi) \quad (5.9)$$

where C is pulse shape factor equaling 1 for a flat-top intensity profile in space and time and $2\sqrt{2\pi}$ for a gaussian in space and time. Figure 5.4 shows a few different angle tuning curves for 532-nm SHG in 25-degree-rotated, X-cut VLT for the QPM periods of 7.65, 7.78, 7.9, and 8.03 μm .

Although rotated-cut devices could be used for CW applications, they are most effective when used in pulsed applications. Thus, the maximum efficiency is limited by the laser-induced damage threshold as a function of pulse width.

To explore the utility of 25-degree-rotated devices, we examine two different applications. The first application is optical parametric amplification (OPA) of 2128-nm radiation with 1064-nm radiation and the second application is generation of 532-nm radiation by SHG. With a flat-top intensity profile in space and time, we can write down the analytical formula for the SHG efficiency, η_{SHG} , and the parametric gain, G_{OPA} , neglecting Fresnel reflections.

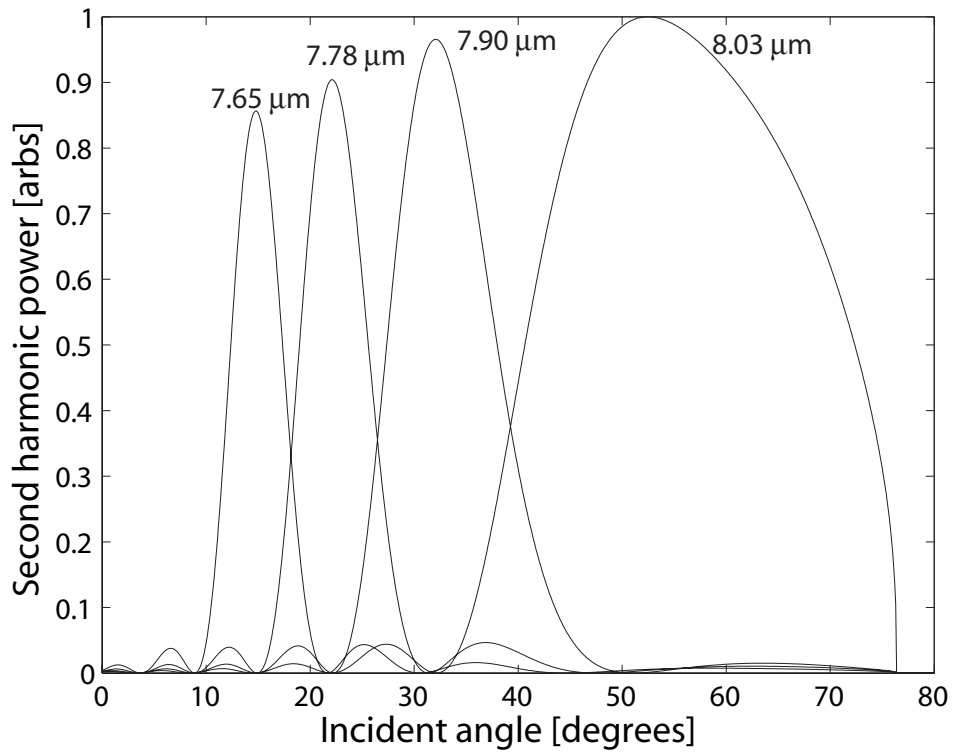


Figure 5.4: Theoretical angular tuning curves for SHG of 1064-nm radiation to generate 532-nm radiation in a 1-mm-thick 25-degree-rotated, X-cut VLT crystal for poling periods of 7.65, 7.78, 7.9, and 8.03 μm .

$$\eta_{\text{SHG}} = \tanh^2 \left(\sqrt{\frac{2\omega^2 d^2}{n_1^2 n_2 c_0^3 \epsilon_0} \frac{F}{\tau} \frac{L^2}{\cos^2 \theta_{\text{SH}}}} \right)$$

$$G_{\text{OPA}} = \cosh^2 \left(\sqrt{\frac{2\omega_i \omega_s d^2}{n_s n_p n_i c_0^3 \epsilon_0} \frac{F}{\tau} \frac{L^2}{\cos^2 \theta_{\text{SH}}}} \right)$$

Here the ω_s and ω_i are the signal and idler frequencies of the OPA process (here both equal at the frequency of 2128 nm) with refractive indexes n_s and n_i , respectively. The pump frequency (the 1064-nm radiation) has a refractive index of n_p .

If we assume that the damage threshold measured in Section 3.2.4 (7.3 J/cm² at 12 ns) scales like $\sqrt{\tau}$, then we can plot the parametric gain and SHG efficiency. Figure 5.5 shows the parametric gain of 2128-nm radiation and 532-nm SHG efficiency as a function of pulse width for a 1-mm-thick device. Alternatively, Figure 5.6 shows the parametric gain of 2128-nm radiation and 532-nm SHG efficiency as a function of crystal thickness for a 50-ps pulse. For both these graphs, we assume a fluence, F , that is $\frac{1}{2}$ the damage fluence.

From both these graphs two important values are needed. A typical power-amplifier OPA device will become useful when it can achieve approximately 10 dB of parametric gain, while a typical SHG device will be come extremely useful at approximately 50 % efficiency. For both these conditions, we can calculate the required pulse width for a fixed thickness or the required thickness for a fixed pulse width. With a 1-mm-thick device, it will be possible to achieve 10 dB of parametric gain for pulses shorter than 0.25 ns and 50 % SHG efficiency with pulses less than 14 ns. These pulse widths are very reasonable for typical laser sources available today for those particular applications. With a 50-ps pulse width, a crystal thicker than 0.74 mm will be required for 10 dB of parametric gain and a crystal thicker than 0.25 mm will be required for 50 % SHG efficiency. With current fabrication techniques, 0.74 mm thick material should be well within the process parameters.

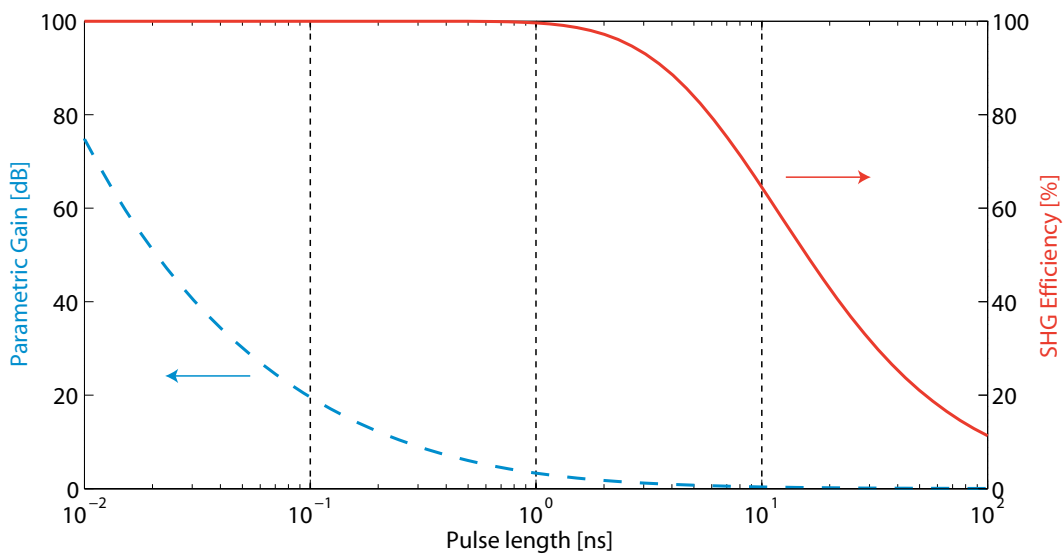


Figure 5.5: Theoretical parametric gain at 2128 nm (dashed line) and 532-nm SHG conversion efficiency (solid line) for various pulse widths using $\frac{1}{2}$ the damage threshold. This chart assumes that the measured damage threshold of 7.3 J/cm^2 from Section 3.2.4 is proportional to $\sqrt{\tau}$ and a flat-top intensity profile in space and time and a 1-mm-thick device.

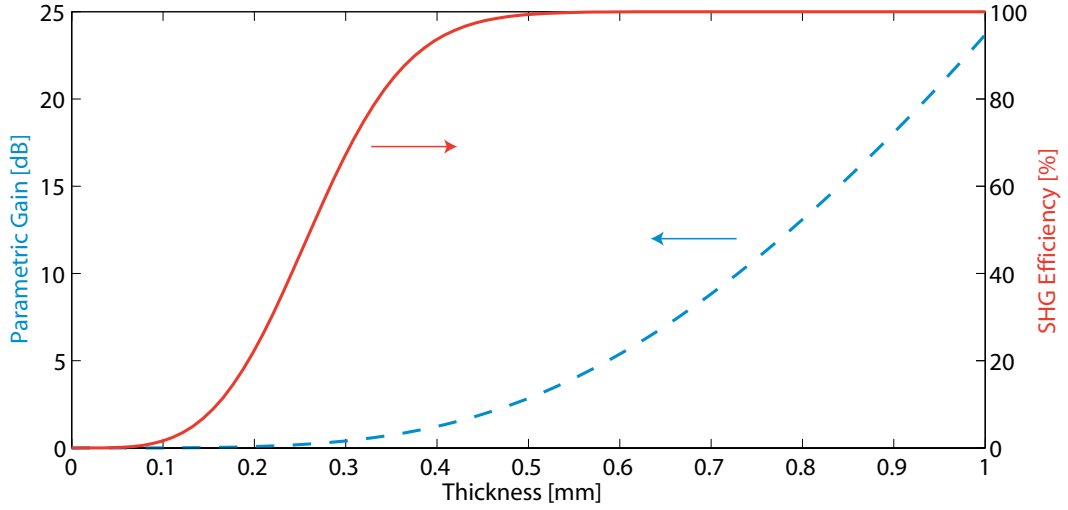


Figure 5.6: Theoretical parametric gain at 2128 nm (dashed line) and 532-nm SHG conversion efficiency (solid line) for various thicknesses using $\frac{1}{2}$ the damage threshold. This chart assumes that the measured damage threshold of 7.3 J/cm^2 from Section 3.2.4 is proportional to $\sqrt{\tau}$ and a flat-top intensity profile in space and time and a 50-ps pulse width.

5.3 Ferroelectric Properties of rotated-cut LT

Some of the “apparent” ferroelectric properties change when periodic poling rotated-cut LT. Figure 5.7 shows the relevant diagram when poling rotated-cut LT. Here, the applied field E_{app} is parallel to the surface normal while the coercive field and the spontaneous polarization are aligned with the ferroelectric axis.

Since the surface normal and the ferroelectric axis are not parallel, the “apparent” coercive field, $E_{c,\text{rot}}$ is magnified by a factor of $1/\cos\theta_R$ while the “apparent” spontaneous polarization, $P_{s,\text{rot}}$, is reduced by $\cos\theta_R$. The geometry also affects the surface pattern period. The patterned period, Λ_{surf} is magnified from the desired QPM period Λ by the factor $\frac{1}{\cos\theta_R}$. Equations 5.10 to 5.12 summarize these modifications.

$$E_{c,\text{rot}} = \frac{E_c}{\cos\theta_R} \quad (5.10)$$

$$P_{s,\text{rot}} = P_s \cos\theta_R \quad (5.11)$$

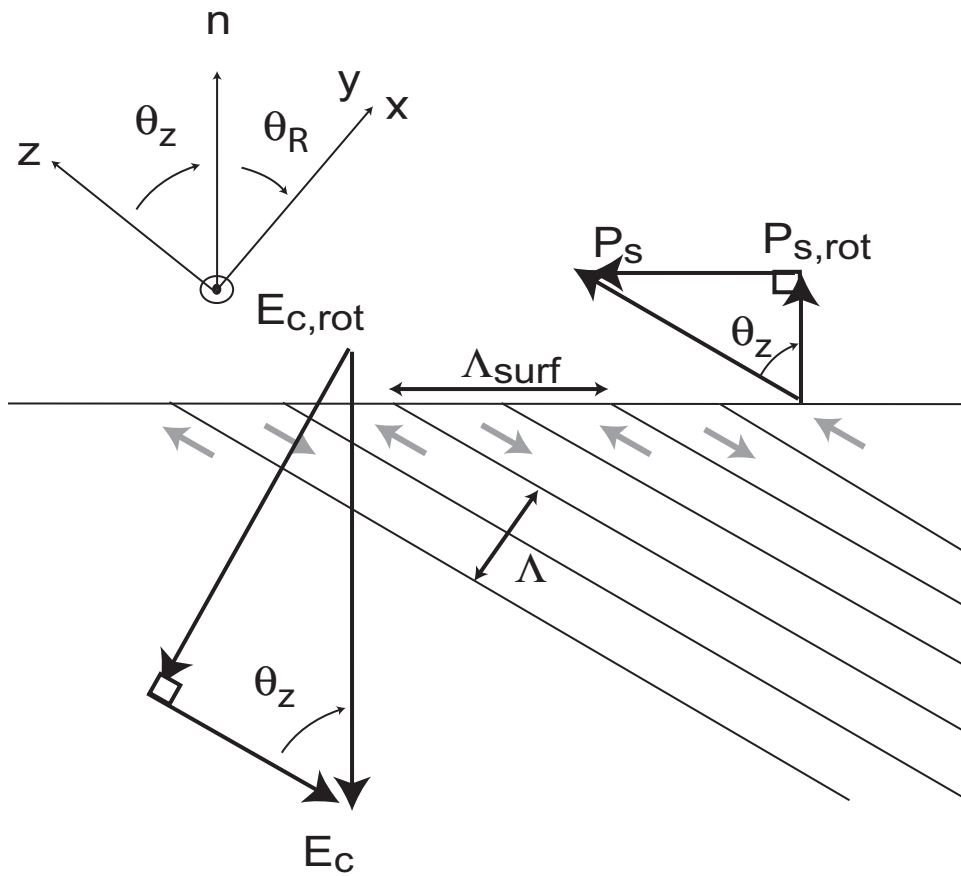


Figure 5.7: Ferroelectric properties of a rotated-cut crystal.



Figure 5.8: Applied fields crack rotated-cut LN (128-degree-rotated, X-cut) before domain inversion.

$$\Lambda_{\text{surf}} = \frac{\Lambda}{\cos \theta_R} \quad (5.12)$$

5.4 25-degree-rotated, X-cut VLT

The first attempts to periodically pole for QPM nonlinear devices were made on congruent-composition lithium niobate. These substrates would crack, as shown in Figure 5.8, before domain inversion because the piezoelectric strain (estimated to be on the order of 10^{-3}) would exceed the fracture strain.

With the lowered coercive field of vapor-transport-equilibrated LN and VLT, it was apparent that domain inversion could be achieved in rotated-cut substrates without fracture. However, it remained important to show that the ferroelectric domain walls would follow the ferroelectric axis. Figure 5.9 shows that the bulk inversion of a rotated-cut, vapor-transport-equilibrated LN crystal and confirms that the domain walls do follow the ferroelectric axis. Figure 5.10 shows 42-degree-rotated, Y-cut near-stoichiometric LT fabricated by VTE was periodically poled at a period of 42 μm . This periodically poled device was used for quasi-phasematched SHG of 532-nm radiation.[99] Periodic poling of rotated-cut, congruent-composition LT substrates

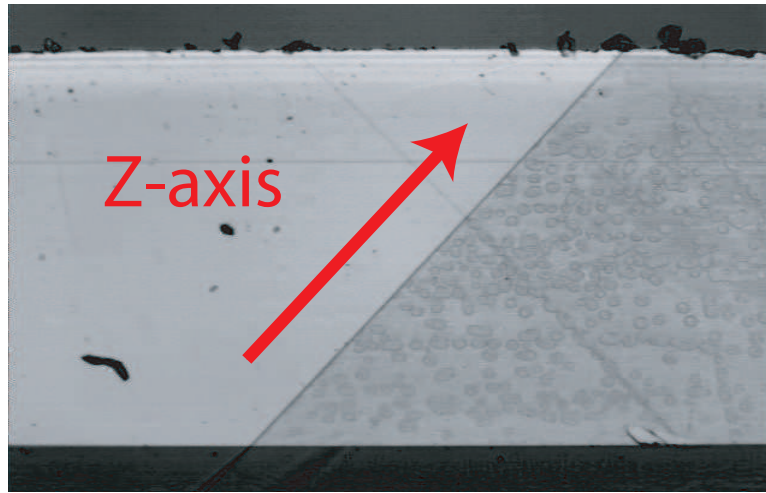


Figure 5.9: Side etching of a 0.4-mm-thick, 64-degree-rotated, vapor-transport-equilibrated LN sample. The domain wall of the inverted region follows the ferroelectric axis.

has also been shown for surface acoustic wave applications.[100]

For nonlinear optics purposes, we have chosen to develop periodic poling of 25-degree-rotated, X-cut, near-stoichiometric lithium tantalate fabricated by vapor transport equilibration (VTE). Figure 5.11 shows a diagram of SHG of 532-nm radiation in 25-degree-rotated VLT. Each characteristic is important for either the nonlinear optics or the fabrication properties. We shall discuss each characteristic briefly. The 25-degree angle of rotation allows collinear nonlinear optic interactions to be performed with light incident at nearly Brewster's angle. The collinear interaction also maximizes the component of the electric field that is polarized along the extraordinary axis for maximum efficiency. In a SHG experiment, the fundamental is incident on the crystal face at Brewster's angle. The fundamental will then propagate perpendicular to the domain walls and phase match collinearly with its second harmonic for the proper choice of QPM period. Since Brewster's angle changes very little over a wide wavelength range, the second harmonic exits the crystal near Brewster's angle.

With the angle of rotation selected, the cut of the crystal indicates which crystal axis is in the plane of the wafer. We have chosen the y-axis to be in-plane since +y and -y domains have a differential etch rate. This differential etch rate permits

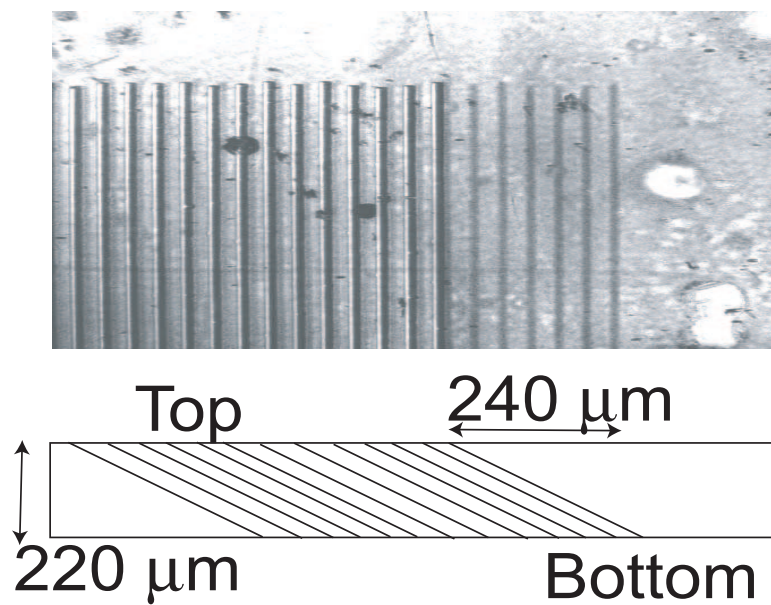


Figure 5.10: Periodic poling of 42-degree-rotated, Y-cut VLT. On the left side of the image the domains are revealed on the top surface of the crystal. Dark regions on the right result from scattering of the etched domains on the back surface of the 220- μm -thick sample. Domains are made visible by chemical etching with hydrofluoric acid.

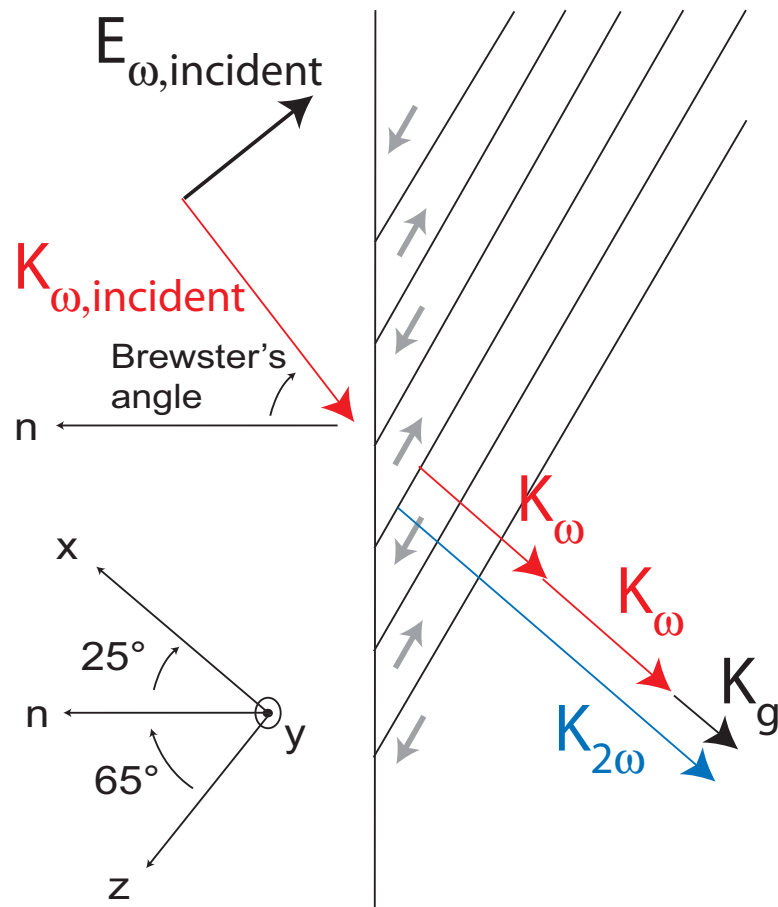


Figure 5.11: Diagram of SHG of 532-nm radiation in 25-degree-rotated, VLT.

visualization of the domains by side etching after patterning. Moreover, the domains will be oriented in the same configuration as conventional, z-cut substrates. These properties are important to develop reproducible, high-quality domain patterns.

Finally, we have chosen to develop periodic poling in VLT. As shown in previous chapters, VLT has reduced sensitivity to PRD and GRIIRA which allow for operation at visible and near infrared wavelengths and has lower coercive field, allowing thicker substrates to be poled.

5.5 Generation of 532-nm radiation by SHG

The substrates for the VTE process were 50-mm-diameter, 1-mm-thick, 25-degree-rotated, X-cut, congruent lithium tantalate (CLT) wafers from Sawyer Technical Materials, LLC. The VTE process was carried out at 1360 °C over a period of 120 hours. After the VTE processing, it was necessary to uniformly pole the samples in order to enable periodic poling. The uniform poling process was performed at 185 °C with graphite electrodes and applied fields as high as 1000 V/mm to remove the head-to-head domains that result from the VTE process. To ensure complete poling, the applied field was reversed several times. Afterwards, the crystals were annealed in air at 620 °C for 10 hours. These crystals were then ground and polished on both sides to a final dimension of 0.5 mm in thickness before periodic poling. Unlike conventional z-cut devices, periodic domains have not been shown to propagate through substrates that are not polished or etched.

The “apparent” coercive field and spontaneous polarization at room temperature were 315 V/mm and 27 $\mu\text{C}/\text{cm}^2$, respectively, as shown in Figure 5.12. For this rotation angle, the equivalent z-cut coercive field is 133 V/mm and the equivalent z-cut spontaneous polarization is 63 $\mu\text{C}/\text{cm}^2$. These values are consistent with similarly processed optical-grade, z-cut substrates.

Before periodic poling, the crystals were ground and polished on both sides to a final dimension of 0.5 mm in thickness. Periodic poling was carried out at 120 °C with aluminum electrodes evaporated over a 1- μm -thick photoresist (Shipley 3612). The

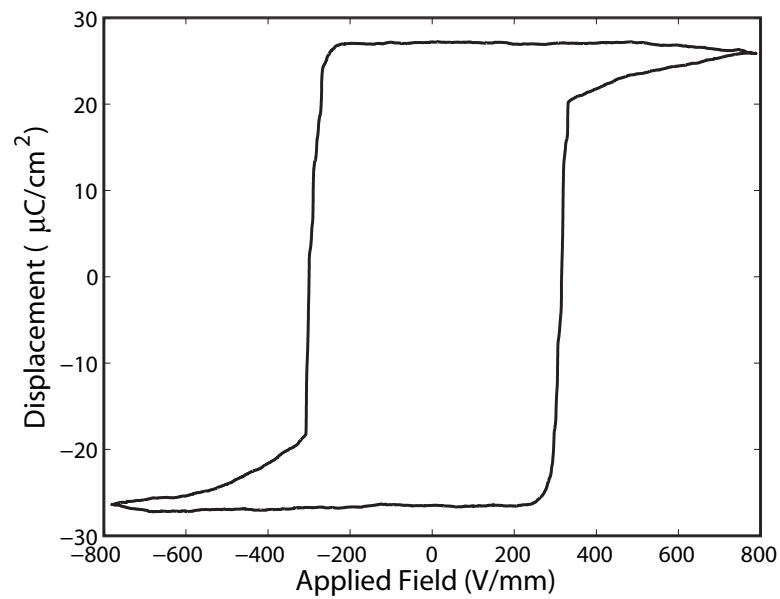


Figure 5.12: A measured hysteresis loop of a 25-degree-rotated, X-cut VLT sample. The loop time was 500 s and the peak-to-peak voltage was 800 V. Conduction observed at high applied electric field is consistent with leakage under the liquid-electrode-constraining O-ring.

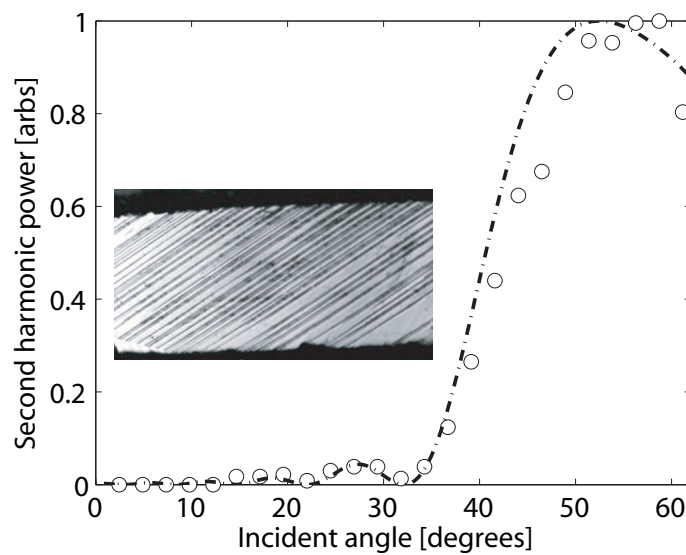


Figure 5.13: An angular tuning curve of generated 532-nm SHG power as a function of incident fundamental angle. The source used in this experiment was a modelocked, 9.2-W-average-power, 7-ps, 50-MHz-repetition-rate, 1064-nm laser. The dotted curve represents the theoretical angular tuning curve. (Inset) Photograph of 25-degree-rotated domains (+y surface) revealed by chemical etching in hydrofluoric acid. The domain period is $8 \mu\text{m}$.

reduced thickness and elevated periodic poling temperature served to increase nucleation and improve overall domain quality. Poling was performed with a single poling pulse for a duration of 15 ms at 540 V/mm for an 8- μm period grating for first-order QPM SHG of 532-nm radiation. Samples were then polished along the +y surface and chemically etched for 20 minutes to reveal domain patterns. A photograph of a chemically etched sample is shown in the inset of Figure 5.13. After periodic poling and etching, the aluminum electrodes and photoresist were removed in preparation for SHG measurements.

To examine the local efficiency and the high energy operation of the substrates two separate SHG measurements were performed. A modelocked, 9.2-W-average-power, 7-ps, 50-MHz-repetition-rate, 1064-nm laser was loosely focussed to a 135- μm spot ($1/e^2$ -intensity-radius, excluding the foreshortening due to non-normal incidence on the sample). An angle-tuning curve was measured and fits well with the theoretical calculations. The generated SHG power was then measured as a function of position over a 6 mm by 7 mm area. The results from this experiment are shown in Figure 5.14. The maximum SHG power generated was 30 mW and is a factor of 3.5 below theoretical for this loose focus (assuming $d_{\text{eff}} = 11 \text{ pm/V}$).^[52] The discrepancy can be explained by poling errors (mostly merged domains) and domains that did not propagate the full thickness of the wafer. The laser was then focussed to a 30- μm spot ($1/e^2$ -intensity radius, excluding the foreshortening) and generated a maximum of 540 mW of 532-nm radiation. The experimental conversion efficiency is again a factor of 3.5 below theoretical. Although the uniformity of the sample was poor, further improvements in periodic poling will enable scaling of the useable area for future devices.

To examine the high-energy capacity of a rotated cut sample, we focussed a 1-J-per-pulse, 7-ns, Q-switched, 1064-nm laser on a 0.26 cm^2 area of the crystal (including the foreshortening). The damage threshold in z-cut near-stoichiometric lithium tantalate fabricated by vapor-transport equilibration was measured to be 7.3 J/cm^2 for 12-ns pulses (Section 3.2.4). At the input energy of 1 J, no laser-induced damage was observed and the SHG energy was measured to be 21 mJ, a factor of 4.2 below theoretical.

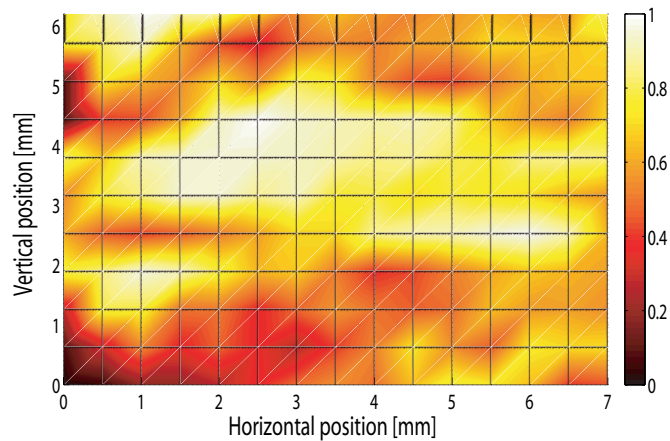


Figure 5.14: A spatial map of the generated 532-nm power as a function of position for a 6 mm by 7 mm sample area. The source used in this experiment was a modelocked, 9.2-W-average-power, 7-ps, 50-MHz-repetition-rate, 1064-nm laser.

It is clear that large-aperture (nearly wafer size), efficient nonlinear devices can be fabricated using this topology. With improved poling and thicker substrates, rotated-cut QPM ferroelectrics seem promising alternatives to birefringently phasematched materials. Efficient interactions can occur in a 1-mm-thick wafer. With improved crystal growth, larger substrates and higher laser-induced damage thresholds may be possible, further expanding the useful range of application of these materials. In particular, these substrates may be useful for the next generation of laser-fusion facilities as an alternative to potassium dihydrogen phosphate (KDP) crystals. Further material development could allow for exploration of spatial engineering of the QPM properties. For example, by engineering either the local duty cycle or deleting reversals, the local conversion efficiency can be modulated to compensate for the gaussian intensity profile, removing the requirement for flat-top beams. This has been shown earlier in a 1-D format by Imeshev et al.[101] Furthermore, fan-like poling [7] can be used for either tunability or as a replacement for noncollinear interactions.

Chapter 6

Summary and Future Directions

6.1 Summary of Contributions

The primary goal of this work was to fabricate and characterize periodically poled ferroelectrics resistant to the aging effects that previously limited the application of these materials at room temperature. Periodically poled, vapor-transport-equilibrated, near-stoichiometric lithium tantalate (VLT) meets these requirements.

First, process development for the fabrication of near-stoichiometric lithium tantalate was performed. In particular, the ferroelectric properties were measured and the development of a reproducible periodic poling process was achieved. The coercive field (and hence the stoichiometry) of VLT was measured as a function of VTE process time. Coercive fields as low as 60 V/mm were measured implying a lithium deficiency as low as 50 ppm. The processing time for even the lowest coercive fields was approximately 160 hours for 1-mm-thick substrates. The coercive field of VLT samples varied by 15 V/mm across a 2" wafer, however, this nonuniformity did not affect periodic poling or device performance. The domain wall velocity was measured as a function of applied field for characterization of the optimal poling field. Effects of backswitching and domain rearrangement were observed and process steps were implemented to allow stable, reproducible, periodic domains. Domain patterns with periods as low as 8 μm were poled on 1-mm-thick, 2" wafer substrates. A period of 5 μm was achieved on a 0.5-mm-thick sample with an interaction length of 1.5 cm.

Measurements of various material properties as a function of the VTE process were made. The nonlinear coefficient was measured to be the same as that of congruent-composition material. The photorefractive damage resistance was improved significantly. A saturated space charge field of 10 V/cm at 514.5 nm was measured indicating that a length of approximately 17 cm could be used without significant photorefractive damage, a 100-fold improvement over CLT. The low-intensity, saturated space charge increased by a factor of 2 at a wavelength of 457.9 nm. The saturated space charge increased by a factor of 2 at a peak intensity of 300 MW at 532 nm. Characterization of the absorption showed the ordinary-wave absorption of VLT is less than 1 cm^{-1} for wavelengths from 320 nm to $5.1 \mu\text{m}$. Extraordinary-wave absorption in the visible and near-infrared ranged from 0.01-0.4 %/cm and the induced 1064-nm absorption was less than 0.06 %/(W-cm). Two-photon absorption of 532-nm radiation was measured to be 0.55 cm/GW. Bulk, laser-induced damage threshold was measured to be 7.3 J/cm^2 at 12 ns, though measurements suggest that with improved growth conditions the laser-induced damage threshold could increase by a factor of 4. Thermal conductivity of VLT was shown to increase compared to its congruently melting counterpart. The thermal conductivity along the extraordinary axis and ordinary axis increased by nearly factors of 2 and 1.2 respectively.

To show the utility of VLT in frequency conversion experiments, visible generation near room temperature was performed. SHG of 532-nm radiation was performed under various conditions which stressed the limits of conventional materials. A nanosecond pulsed laser was doubled to produce 5 W of 532-nm radiation in a VLT crystal that maintained efficient generation for more than 1000 hrs. A CW source was frequency doubled to produce 10 W of 532-nm radiation. Efficient SHG with no apparent degradation was demonstrated with peak intensities as high as 450 MW/cm^2 in the infrared and 100 MW/cm^2 in the visible. 3.25 W of 589-nm radiation was generated by SHG. 1.38 W of 589-nm radiation was generated by SFG using fiber MOPA systems. 8.7 W of 589-nm was produced by SFG using modelocked 1319-nm and 1064-nm lasers. In all 589-nm generation experiments, no signs of PRD or photochromism were observed. VLT may provide an efficient, low-cost alternative for the generation of 589-nm radiation for laser guide star applications. Periodic poling of

5- μm -period devices allowed for the generation of 458.3-nm radiation by SHG.

Finally, VLT was shown to enable a new topology for scalable apertures in rotated-cut substrates. Processes to fabricate periodically poled 25-degree-rotated, X-cut VLT were developed. Periodic domain patterns as short as 8 μm have been demonstrated. A 6 mm by 7 mm area on a large sample was characterized using SHG of 532-nm radiation. A maximum of 540 mW from 10 W of average power was generated with 7-ps pulses, a factor of 3.5 from theoretical calculations. The sample was then used for SHG using a 1 J source and generated 21 mJ.

6.2 Future Directions

After development of bulk VLT devices which are able to operate with watt-level beams of visible light there are many possible avenues for future research. In the opinion of the author, the major directions are: a) further measurements of absorption and laser-induced damage threshold and further steps to reduce them may expand the utility of VLT at very high average powers, b) devices to further show the utility of VLT with watt-level visible light, c) development of waveguide devices and measurement of their susceptibility to photorefractive damage, and d) further development of rotated-cut devices.

6.2.1 Material improvements and characterization

To further enhance the practicality of the material, two major questions must be addressed. First, what is the origin of the UV and visible absorption and can the absorption be reduced? Second, what is the origin of the bulk, laser-induced damage threshold and can it be increased?

As shown in the absorption measurements, the UV absorption is attributed to either transition or noble metals incorporated during growth. The visible absorption has been attributed to the tail of the UV absorption and may also be reduced if the transition or noble metals are either eliminated or their oxidation states are controlled.

Bulk, laser-induced damage was observed in Section 3.2.4, however, it is extremely

uncommon for the bulk of these devices to damage before the surface. This implies that there are damageable centers incorporated during the growth process that initiate damage before the defects on the surface caused by polishing. If these damageable sites could be eliminated, the laser-induced damage threshold would be increased. This damage threshold should also be characterized at longer and shorter pulse lengths to understand the scaling of the damage as a function of pulse length.

Beyond these material improvements, further measurements of extraordinary-wave mid-infrared absorption, nonlinear refractive index and two-photon absorption at various wavelengths should be performed.

6.2.2 Bulk Nonlinear Devices

There are many new bulk devices that can take advantage of VLT as an efficient nonlinear material.

Experiments using 100 W of 1064-nm radiation for the generation of 532-nm radiation will push the limits of PP ferroelectrics and may provide better understanding about the limiting material characteristics at these power levels.

Optical parametric amplification and oscillation using visible pump wavelengths may provide tunable, efficient and engineerable optical sources. In particular high-energy, chirped-pulse optical parametric amplification with 532-nm radiation as the pump wavelength could be practical. Although 532-nm-pumped, optical parametric oscillators (OPO) have been demonstrated in the pulsed and quasi-CW regime at elevated temperatures ($\sim 90^\circ\text{C}$), [102, 103, 104] demonstration of a true CW, optical parametric oscillator pumped at 532 nm, operating at room temperature could be an extremely useful device.

Experiments using a high-average-power, Nd:GdVO₄ or Nd:Y₂O₃ laser operating at approximately 915 nm could provide a high-power blue source for display applications.

6.2.3 Waveguide Nonlinear Devices

It has been shown that saw-cut or etched ridge waveguide devices in melt-grown near-stoichiometric LT provide enhanced efficiency and can support watt-level visible light.[105] However, measurements of the properties of well-developed proton-exchanged (annealed and reverse-exchanged) waveguide devices may also provide some important information. Reverse-proton-exchanged devices in melt-grown near-stoichiometric LT have shown to be more resistant to photorefractive damage than their congruently melting counterparts.[106, 107] Although the development of periodic poling, proton-exchange, annealing and reverse exchange processes is very important, an accurate method to quantify the susceptibility to photorefractive damage must be developed. Process development of post-exchange periodic poling will be challenging. Matthews et al. has already characterized the initial proton exchange and the soft-anneal process in CLT.[108] To measure the photorefractive damage in waveguides, a few techniques have already been developed.[109] Alternatively, appropriately patterned electrodes may provide direct measurement of the photogalvanic and photoconductive currents for calculation of a saturated space charge field.

6.2.4 Rotated-cut devices

Rotated-cut devices provide a whole new realm of development. Improvement of the periodic poling process will provide more uniform devices and improved efficiency. The ultimate application of these devices may be toward high-energy, chirped-pulse optical parametric amplification and will require development of periodic poling at slightly larger periods on thicker substrates. Moreover, engineering of the spatial characteristics of the quasi-phasematched interaction could provide both tunability and beam shaping.

6.3 Conclusion and Forward Outlook

It is apparent that practical QPM devices may soon be used for various applications in the visible. VLT provides improved resistance to photorefractive damage, reduced induced

infrared absorption and increased thermal conductivity. These improved characteristics widen the window of utility for QPM materials.

In particular, devices engineered around VLT could enable a multitude of low-cost visible sources. VLT used in focussed interactions can provide multi-watt CW sources which were previously unavailable. The efficiencies provided by devices based on VLT are well matched with the output powers available from current fiber laser technology. This combination may allow for lower-cost, compact and efficient lasers to a multitude of new applications.

The development of ridge waveguides in VLT is rapidly progressing. Single-pass nonlinear interactions in a VLT waveguide are efficient with only 1-2 watts of input power. In combination with laser-diode single emitters that have shown as much as 5 W of output power, these waveguide devices will provide low-cost visible sources for various applications.

Devices based on rotated-cut VLT may supplant KDP and LBO for nonlinear interactions with pulsed lasers. Improvement in the crystal growth may allow large areas, perhaps 150-mm-diameter wafers. SHG using only 1-mm-thick wafers could be efficient and economical for future laser-fusion experimental facilities. Chirped-pulse optical parametric amplification in devices based on rotated-cut VLT may provide sources with larger pulse energies to explore the realm of atomic and molecular dynamics in strong laser fields.

Bibliography

- [1] C. V. Raman and K. S. Krishnan. New class of spectra due to secondary radiation. *Indian Journal of Physics*, 2:399 – 419, 1928.
- [2] J. A. Armstrong, N. Bloembergen, J. Ducuing, and P. S. Pershan. Interactions between light waves in a nonlinear dielectric. *Physical Review*, 127(6):1918 – &, 1962.
- [3] G. D. Boyd and D. A. Kleinman. Parametric interaction of focused gaussian light beams. *Journal of Applied Physics*, 39(8):3597 – 3639, 1968.
- [4] D. A. Kleinman, A. Ashkin, and G. D. Boyd. The second harmonic generation of light by focused laser beams. *IEEE Journal of Quantum Electronics*, QE-2(9):425 – 429, 1966.
- [5] P. A. Franken and J. F. Ward. Optical harmonics and nonlinear phenomena. *Reviews of Modern Physics*, 35(1):23 – 39, 1963.
- [6] L. E. Myers, R. C. Eckardt, M. M. Fejer, R. L. Byer, and W. R. Bosenberg. Multigrating quasi-phase-matched optical parametric oscillator in periodically poled LiNbO₃. *Optics Letters*, 21(8):591 – 3, 1996.
- [7] A. M. Schober, G. Imeshev, and M. M. Fejer. Tunable-chirp pulse compression in quasi-phase-matched second-harmonic generation. *Optics Letters*, 27(13):1129 – 31, 2002.
- [8] G. Imeshev, A. Galvanauskas, M. A. Aboore, D. Harter, and M. M. Fejer. Femtosecond pulse-shaping using fourier synthetic quasi-phase-matching gratings.

- Proceedings of the SPIE - The International Society for Optical Engineering*, 3616:26 – 31, 1999.
- [9] A. G. Getman, S. V. Popov, and J. R. Taylor. 7 W average power, high-beam-quality green generation in MgO-doped stoichiometric periodically poled lithium tantalate. *Applied Physics Letters*, 85(15):3026 – 8, 2004.
- [10] L. A. Eyres, P. J. Turreau, T. J. Pinguet, C. B. Ebert, J. S. Harris, M. M. Fejer, L. Becouarn, B. Gerard, and E. Lallier. All-epitaxial fabrication of thick, orientation-patterned GaAs films for nonlinear optical frequency conversion. *Applied Physics Letters*, 79(7):904 – 6, 2001.
- [11] M. Harada, K. Muramatsu, Y. Iwasaki, S. Kurimura, and T. Taira. Periodic twinning in crystal quartz for optical quasi-phase matched secondary harmonic conversion. *Journal of Materials Research*, 19(4):969 – 72, 2004.
- [12] R. C. Miller. Optical harmonic generation in single crystal BaTiO₃. *Physical review A - General Physics*, 134(5A):1313 – &, 1964.
- [13] Y.H. Xue, N. B. Min, J. S. Zhu, and D. Feng. The 2nd harmonic-generation in LiNbO₃ crystals with periodic laminar ferroelectric domains. *Chinese Physics*, 4(3):554 – 564, 1984.
- [14] A. Feisst and P. Koidl. Current induced periodic ferroelectric domain structures in LiNbO₃ applied for efficient nonlinear optical frequency mixing. *Applied Physics Letters*, 47(11):1125 – 7, 1985.
- [15] E. J. Lim, M. M. Fejer, and R. L. Byer. 2nd-harmonic generation of green light in periodically poled planar lithium niobate waveguide. *Electronics Letters*, 25(3):174 – 175, 1989.
- [16] C. J. Van Der Poel, J. D. Bierlein, J. B. Brown, and S. Colak. Efficient Type-I blue 2nd-harmonic generation in periodically segmented KTiOPO₄ wave-guides. *Applied Physics Letters*, 57(20):2074 – 2076, 1990.

- [17] M. Yamada, N. Nada, M. Saitoh, and K. Watanabe. 1st-order quasi-phase matched LiNbO_3 wave-guide periodically poled by applying an external-field for efficient blue 2nd-harmonic generation. *Applied Physics Letters*, 62(5):435 – 436, 1993.
- [18] S. Matsumoto, E. J. Lim, H. M. Hertz, and M. M. Fejer. Quasiphase-matched 2nd harmonic generation of blue-light in electrically periodically poled lithium tantalate wave-guides. *Electronics letters*, 27(22):2040 – 2042, 1991.
- [19] M.E Lines and A.M. Glass. *Principles and Applications of Ferroelectrics and Related Materials*. Oxford University Press, 2001.
- [20] P. F. Bordui, R. G. Norwood, C. D. Bird, and G. D. Calvert. Compositional uniformity in growth and poling of large-diameter lithium niobate crystals. *Journal of Crystal Growth*, 113(1/2):61 – 8, 1991.
- [21] M. Jazbinsek, M. Zgonik, S. Takekawa, M. Nakamura, K. Kitamura, and H. Hatano. Reduced space-charge fields in near-stoichiometric LiTaO_3 for blue, violet, and near-ultraviolet light beams. *Applied Physics B: Lasers and Optics*, 75(8):891 – 894, 2002.
- [22] Y. Furukawa, K. Kitamura, A. Alexandrovski, R. K. Route, M. M. Fejer, and G. Foulon. Green-induced infrared absorption in MgO doped LiNbO_3 . *Applied Physics Letters*, 78(14):1970 – 2, 2001.
- [23] Y. Furukawa, K. Kitamura, S. Takekawa, A. Miyamoto, M. Terao, and N. Suda. Photorefraction in LiNbO_3 as a function of $[\text{Li}]/[\text{Nb}]$ and MgO concentrations. *Applied Physics Letters*, 77(16):2494 – 6, 2000.
- [24] Rostislav V. Roussev, Roger Route, Joseph Schaar, Karel Urbanek, Martin M. Fejer, Dieter Jundt, and Claudia Kajiyama. Periodically poled vapor transport equilibrated lithium niobate for visible light generation. *Proceedings of SPIE - The International Society for Optical Engineering*, 6103, 2006.

- [25] L. Huang, D. Hui, D. J. Bamford, S. J. Field, I. Mnushkina, L. E. Myers, and J. V. Kayser. Periodic poling of magnesium-oxide-doped stoichiometric lithium niobate grown by the top-seeded solution method. *Applied Physics B: Lasers and Optics*, 72(3):301 – 306, 2001.
- [26] I. Shoji, T. Kondo, A. Kitamoto, M. Shirane, and R. Ito. Absolute scale of second-order nonlinear-optical coefficients. *Journal of the Optical Society of America B*, 14(9):2268–2294, 1997.
- [27] Y. Furukawa, K. Kitamura, S. Takekawa, K. Niwa, and H. Hatano. Stoichiometric Mg:LiNbO₃ as an effective material for nonlinear optics. *Optics Letters*, 23(24):1892 – 4, 1998.
- [28] N. E. Yu, S. Kurimura, Y. Nomura, and K. Kitamura. Stable high-power green light generation with thermally conductive periodically poled stoichiometric lithium tantalate. *Japanese Journal of Applied Physics, Part 2 (Letters)*, 43(10A):L1265 – 7, 2004.
- [29] Y. Furukawah, K. Kitamura, E. Suzuki, and K. Niwa. Stoichiometric LiTaO₃ single crystal growth by double crucible czochralski method using automatic powder supply system. *Journal of Crystal Growth*, 197(4):889 – 95, 1999.
- [30] J.F. Shackelford and R. L. Holman. Nonstoichiometry in ABO₃ compounds similar to PbTiO₃. *Journal of Applied Physics*, 46(4):1429 – 34, 1975.
- [31] F. Holtmann, J. Imbrock, C. Baumer, H. Hesse, E. Kratzig, and D. Kip. Photorefractive properties of undoped lithium tantalate crystals for various composition. *Journal of Applied Physics*, 96(12):7455 – 7459, 2004.
- [32] M. Katz, R. K. Route, D. S. Hum, K. R. Parameswaran, G. D. Miller, and M. M. Fejer. Vapor-transport equilibrated near-stoichiometric lithium tantalate for frequency-conversion applications. *Optics Letters*, 29(15):1775 – 7, 2004.
- [33] D. A. Roberts. Simplified characterization of uniaxial and biaxial nonlinear optical crystals: a plea for standardization of nomenclature and conventions. *IEEE Journal of Quantum Electronics*, 28(10):2057 – 74, 1992.

- [34] M. M. Fejer, G. A. Magel, D. H. Jundt, and R. L. Byer. Quasi-phase-matched second harmonic generation: Tuning and tolerances. *IEEE Journal of Quantum Electronics*, 28(11):2631–2654, 1992.
- [35] G. D. Boyd and D. A. Kleinman. Parametric interaction of focused gaussian light beams. *Journal of Applied Physics*, 39(8):3597–3639, 1968.
- [36] D. R. White, E. L. Dawes, and J. H. Marburger. Theory of second-harmonic generation with high-conversion efficiency. *IEEE Journal of Quantum Electronics*, QE/6(12):793 – 6, 1970.
- [37] S. Guha and J. Falk. The effects of focusing in the three-frequency parametric upconverter. *Journal of Applied Physics*, 51(1):50 – 60, 1980.
- [38] O. F. Schirmer, O. Thiemann, and M. Wohlecke. Defects in LiNbO₃ 1. experimental aspects. *Journal of Physics and Chemistry of Solids*, 52(1):185 – 200, 1991.
- [39] A. Ashkin, G. D. Boyd, J. M. Dziedzic, R. G. Smith, A. A. Ballman, J. J. Levinstein, and K. Nassau. Optically-induced refractive index inhomogeneities in LiNbO₃ and LiTaO₃. *Applied Physics Letters*, 9(1):72 – &, 1966.
- [40] K. Buse. Light-induced charge transport processes in photorefractive crystals .1. models and experimental methods. *Applied Physics B - Lasers and Optics*, 64(3):273 – 291, 1997.
- [41] F. S. Chen. Optically induced change of refractive indices in LiNbO₃ and LiTaO₃. *Journal of Applied Physics*, 40(8):3389 – 96, 1969.
- [42] A. M. Glass, D. van der Linde, and T. J. Negran. High-voltage bulk photovoltaic effect and the photorefractive process in LiNbO₃. *Applied Physics Letters*, 25(4):233 – 5, 1974.
- [43] K. Buse, S. Breer, K. Peithmann, S. Kapphan, M. Gao, and E. Krätzig. Origin of thermal fixing in photorefractive lithium niobate crystals. *Phys. Rev. B*, 56(3):1225–1235, 1997.

- [44] K. Buse, U. vanStevendaal, R. Pankrath, and E. Kratzig. Light-induced charge transport properties of $\text{Sr}_{0.61}\text{Ba}_{0.39}\text{Nb}_2\text{O}_6:\text{Ce}$ crystals. *Journal of the Optical Society of America B (Optical Physics)*, 13(7):1461 – 7, 1996.
- [45] Y. Furukawa, M. Sato, K. Kitamura, Y. Yajima, and M. Minakata. Optical damage resistance and crystal quality of LiNbO_3 single crystals with various (Li)/(Nb) ratios. *Journal of Applied Physics*, 72(8):3250 – 4, 1992.
- [46] O. F. Schirmer, S. Juppe, and J. Koppitz. Electron-spin-resonance, optical and photovoltaic studies of reduced undoped LiNbO_3 . *Crystal Lattice Defects and Amorphous Materials*, 16(1-4):353 – 357, 1987.
- [47] F. Jermann, M. Simon, and E. Kratzig. Photorefractive properties of congruent and stoichiometric lithium niobate at high light intensities. *Journal of the Optical Society of America B (Optical Physics)*, 12(11):2066 – 70, 1995.
- [48] M. Simon, F. Jermann, and E. Kratzig. Light-induced absorption changes in iron-doped LiNbO_3 . *Optical Materials*, 3(4):243 – 50, 1994.
- [49] M. Simon, F. Jermann, and E. Kratzig. Intrinsic photorefractive centers in $\text{LiNbO}_3:\text{Fe}$. *Applied Physics B (Lasers and Optics)*, 61(1):89 – 93, 1995.
- [50] M. D. Feit, F. Y. Genin, A. M. Rubenchik, L. M. Sheehan, S. Schwartz, M. R. Kozlowski, J. Dijon, P. Garrec, and J. Hue. Statistical description of laser damage initiation in NIF and LMJ optics at 355 nm. *Proceedings of the SPIE - The International Society for Optical Engineering*, 3492:188 – 2 [+suppl.], 1999.
- [51] M. D. Feit, A. M. Rubenchik, M. R. Kozlowski, F. Y. Genin, S. Schwartz, and L. M. Sheehan. Extrapolation of damage test data to predict performance of large-area NIF optics at 355 nm. *Proceedings of the SPIE - The International Society for Optical Engineering*, 3578:226 – 34, 1999.
- [52] D. Eimerl. High average power harmonic generation. *IEEE Journal of Quantum Electronics*, QE/23(5):575 – 92, 1987.

- [53] S.A. Akhmanov, A.I. Kovrigin, and A.P. Sukhorukov. *Quantum Electronics: A treatise: Nonlinear Optics, Vol. I, Part B*. Academic Press (New York), 1975.
- [54] S. A. Basun, D. R. Evans, T. J. Bunning, S. Guha, J. O. Barnes, G. Cook, and R. S. Meltzer. Optical absorption spectroscopy of Fe^{2+} and Fe^{3+} ions in LiNbO_3 . *Journal of Applied Physics*, 92(12):7051 – 5, 2002.
- [55] H. Kurz, E. Kratzig, W. Keune, H. Engelmann, U. Gonser, B. Dischler, and A. Rauber. Photorefractive centers in LiNbO_3 , studied by optical-, Mossbauer- and EPR-methods. *Applied Physics*, 12(4):355 – 68, 1977.
- [56] R. Bhatt, S. Kar, K. S. Bartwal, and V. K. Wadhawan. The effect of Cr doping on optical and photoluminescence properties of LiNbO_3 crystals. *Solid State Communications*, 127(6):457 – 62, 2003.
- [57] A. L. Alexandrovski, G. Foulon, L. E. Myers, R. K. Route, and M. M. Fejer. UV and visible absorption in LiTaO_3 . *Proceedings of the SPIE - The International Society for Optical Engineering*, 3610:44 – 51, 1999.
- [58] O. Beyer, D. Maxein, T. Woike, and K. Buse. Generation of small bound polarons in lithium niobate crystals on the subpicosecond time scale. *Applied Physics B: Lasers and Optics*, 83(4):527 – 530, 2006.
- [59] P. F. Bordui, R. G. Norwood, C. D. Bird, and J. T. Carella. Stoichiometry issues in single-crystal lithium tantalate. *Journal of Applied Physics*, 78(7):4647 – 50, 1995.
- [60] S. Kim, V. Gopalan, K. Kitamura, and Y. Furukawa. Domain reversal and nonstoichiometry in lithium tantalate. *Journal of Applied Physics*, 90(6):2949 – 2963, 2001.
- [61] H. Guenther, R. Macfarlane, Y. Furukawa, K. Kitamura, and R. Neurgaonkar. Two-color holography in reduced near-stoichiometric lithium niobate. *Applied Optics*, 37(32):7611 – 23, 1998.

- [62] L. Tian, V. Gopalan, and L. Galambos. Domain reversal in stoichiometric LiTaO_3 prepared by vapor transport equilibration. *Applied Physics Letters*, 85(19):4445 – 7, 2004.
- [63] B. T. Matthias and J.P. Remeika. Ferroelectricity in the ilmenite structure. *Physical Review*, 79:1886–7, 1949.
- [64] R. L. Barns and J. R. Carruthers. Lithium tantalate single crystal stoichiometry. *Journal of Applied Crystallography*, 3:395 –, 1970.
- [65] A. A. Ballman, H.J. Levinstein, C.D. Capio, and H. Brown. Curie temperature and birefringence variation in ferroelectric lithium metatantalate as a function of melt stoichiometry. *Journal of the American Ceramics Society*, 50:657–9, 1967.
- [66] R. L. Holman and R. M. Fulrath. Intrinsic nonstoichiometry in the lead zirconate-lead titanate system determined by Knudsen effusion. *Journal of Applied Physics*, 44(12):5227 – 36, 1973.
- [67] J. R. Carruthers, G. E. Peterson, M. Grasso, and P. M. Bridenbain. Nonstoichiometry and crystal growth of lithium niobate. *Journal of Applied Physics*, 42(5):1846 – 51, 1971.
- [68] Gregory David Miller. *Periodically Poled Lithium Niobate: Modeling, Fabrication, and Nonlinear-Optical Performance*. PhD thesis, Stanford University, 1998.
- [69] V. Y. Shur, A. I. Lobov, A. G. Shur, S. Kurimura, Y. Nomura, K. Terabe, X. Y. Liu, and K. Kitamura. Rearrangement of ferroelectric domain structure induced by chemical etching. *Applied Physics Letters*, 87(2):022905 –, 2005.
- [70] K. Nakamura, J. Kurz, K. Parameswaran, and M. M. Fejer. Periodic poling of magnesium-oxide-doped lithium niobate. *Journal of Applied Physics*, 91(7):4528 – 34, 2002.

- [71] N. E. Yu, S. Kurimura, Y. Nomura, M. Nakamura, K. Kitamura, J. Sakuma, Y. Otani, and A. Shiratori. Periodically poled near-stoichiometric lithium tantalate for optical parametric oscillation. *Applied Physics Letters*, 84(10):1662 – 1664, 2004.
- [72] G. D. Miller, R. G. Batchko, M. M. Fejer, and R. L. Byer. Visible quasi-phase-matched harmonic generation by electric-field-poled lithium niobate. *Proceedings of the SPIE - The International Society for Optical Engineering*, 2700:34 – 45, 1996.
- [73] V. Y. Shur, E. L. Rumyantsev, E. V. Nikolaeva, E. I. Shishkin, D. V. Fursov, R. G. Batchko, L. A. Eyres, M. M. Fejer, and R. L. Byer. Nanoscale backswitched domain patterning in lithium niobate. *Applied Physics Letters*, 76(2):143 – 5, 2000.
- [74] J. H. Ro and M. Cha. Subsecond relaxation of internal field after polarization reversal in congruent LiNbO_3 and LiTaO_3 crystals. *Applied Physics Letters*, 77(15):2391 – 2393, 2000.
- [75] W. N. Herman and L. M. Hayden. Maker fringes revisited: second-harmonic generation from birefringent or absorbing materials. *Journal of the Optical Society of America B (Optical Physics)*, 12(3):416 – 27, 1995.
- [76] P. Blau, S. Pearl, A. Englander, A. Bruner, and D. Eger. Average power effects in periodically poled crystals. *Proceedings of the SPIE - The International Society for Optical Engineering*, 4972:34 – 41, 2003.
- [77] P. F. Bordui and M. M. Fejer. Inorganic crystals for nonlinear optical frequency conversion. *Annual Review of Materials Science*, 23:321 – 379, 1993.
- [78] A. L. Alexandrovski, M. M. Fejer, R. P. Route, and R. L. Byer. Photothermal absorption measurements in optical materials. *Pacific Rim Conference on Lasers and Electro-Optics, CLEO - Technical Digest*, pages 320 – 321, 2000.

- [79] C. Baumer, C. David, A. Tunyagi, K. Betzler, H. Hesse, E. Kratzig, and M. Wohlecke. Composition dependence of the ultraviolet absorption edge in lithium tantalate. *Journal of Applied Physics*, 93(5):3102 – 4, 2003.
- [80] H. Kurz, E. Kratzig, W. Keune, H. Engelmann, U. Gonser, B. Dishler, and A. Rauber. Photorefractive centers in LiNbO₃, studied by optical-, Mossbauer- and EPR-methods. *Applied Physics*, 12(4):355 – 368, 1977.
- [81] C. Baumer, C. David, K. Betzler, H. Hesse, K. Lengyel, L. Kovacs, and M. Wohlecke. Composition dependence of the OH-stretch-mode spectrum in lithium tantalate. *Physica Status Solidi A*, 201(4):R13–16, 2004.
- [82] Yongfa Kong, Wanlin Zhang, Xiaojun Chen, Jingjun Xu, and Guangyin Zhang. OH-absorption spectra of pure lithium niobate crystals. *Journal of Physics: Condensed Matter*, 11(9):2139 – 43, 1999.
- [83] M. Sheik-bahae, A. A. Said, T. H. Wei, D. J. Hagan, and E. W. van Stryland. Sensitive measurement of optical nonlinearities using a single beam. *IEEE Journal of Quantum Electronics*, 26(4):760 – 9, 1990.
- [84] G. Imeshev, M. A. Arbore, M. M. Fejer, A. Galvanauskas, M. Fermann, and D. Harter. Ultrashort-pulse second-harmonic generation with longitudinally nonuniform quasi-phase-matching gratings: pulse compression and shaping. *Journal of the Optical Society of America B (Optical Physics)*, 17(2):304 – 18, FEB 2000.
- [85] R. Desalvo, AA Said, and M. Sheik-Bahae. Infrared to Ultraviolet Measurements of Two-Photon Absorption and n_2 in Wide Bandgap Solids. *Journal of Quantum Electronics*, 32(8):1324, 1996.
- [86] A. Bruner, D. Eger, M. B. Oron, P. Blau, M. Katz, and S. Ruschin. Temperature-dependent sellmeier equation for the refractive index of stoichiometric lithium tantalate. *Optics Letters*, 28(3):194 – 6, 2003.

- [87] V. Z. Kolev, M. W. Duering, and B. Luther-Davies. Corrections to refractive index data of stoichiometric lithium tantalate in the 5-6 μm range. *Optics Letters*, 31(13):2033 – 5, 2006.
- [88] Masaru Nakamura, Shinji Higuchi, Shunji Takekawa, Kazuya Terabe, Yasunori Furukawa, and Kenji Kitamura. Refractive indices in undoped and MgO-doped near-stoichiometric LiTaO_3 crystals. *Japanese Journal of Applied Physics, Part 2: Letters*, 41(4):L465 – L467, A 2002.
- [89] D. Eimerl. High average power harmonic generation. *IEEE Journal of Quantum Electronics*, 23(5):575–592, May 1987.
- [90] Yoichi Sato and Takunori Taira. The studies of thermal conductivity in GdVO_4 , YVO_4 , and $\text{Y}_3\text{Al}_5\text{O}_{12}$ measured by quasi-one-dimensional flash method. *Optics Express*, 14(22):10528 – 10536, 2006.
- [91] Valerie C. Coffey. Powerful CW laser produces bright guidestar. *Laser Focus World*, 39(3):11+14 – 11+14, 2003.
- [92] Craig A. Denman, Paul D. Hillman, Gerald T. Moore, Jack D. Drummond, and John M. Telle. Continuous-wave sodium guidestar laser systems. *OSA Trends in Optics and Photonics Series*, 96 A:1621 – 1621, 2004.
- [93] Jay W. Dawson, Alex D. Drobshoff, Raymond J. Beach, Michael J. Messerly, Stephen A. Payne, Aaron Brown, Deanna M. Pennington, Douglas J. Bamford, Scott J. Sharpe, and David J. Cook. Multi-watt 589 nm fiber laser source. *Proceedings of SPIE - The International Society for Optical Engineering*, 6102, 2006.
- [94] A. G. Dronov M. Y. Vyatkin A. B. Rulkov S. V. Popov D. Georgiev, V. P. Gapontsev and J. R. Taylor. Watts-level frequency doubling of a narrow line linearly polarized Raman fiber laser to 589 nm. *Optics Express*, 13(18):6772–6776, 2005.

- [95] V. V. Dvoyrin, V. M. Mashinsky, L. I. Bulatov, I. A. Bufetov, A. V. Shubin, M. A. Melkumov, E. F. Kustov, E. M. Dianov, A. A. Umnikov, V. F. Khopin, M. V. Yashkov, and A. N. Guryanov. Bismuth-doped-glass optical fibers-a new active medium for lasers and amplifiers. *Optics Letters*, 31(20):2966 – 8, 2006.
- [96] K. Mizuuchi, A. Morikawa, T. Sugita, K. Yamamoto, N. Pavel, and T. Taira. Continuous-wave deep blue generation in a periodically poled MgO:LiNbO₃ crystal by single-pass frequency doubling of a 912-nm Nd:GdVO₄ laser. *Japanese Journal of Applied Physics, Part 2 (Letters)*, 43(10A):L1293 – 5, 2004.
- [97] H. Ishizuki and T. Taira. High-energy quasi-phase-matched optical parametric oscillation in a periodically poled MgO:LiNbO₃ device with a 5 mm*5 mm aperture. *Optics Letters*, 30(21):2918 – 20, 2005.
- [98] K. Nakamura, T. Hatanaka, and H. Ito. High output energy quasi-phase-matched optical parametric oscillator using diffusion-bonded periodically poled and single domain LiNbO₃. *Japanese Journal of Applied Physics, Part 2 (Letters)*, 40(4A):L337 – 9, 2001.
- [99] D. S. Hum, R. K. Route, G. D. Miller, and M. M. Fejer. Quasi-phase-matched second harmonic generation using 42 degrees rotated Y-cut near-stoichiometric lithium tantalate. *Conference on Lasers and Electro-Optics (CLEO), 16-21 May 2004, San Francisco, CA, USA*, 2004.
- [100] I. V. Ostrovskii and A. B. Nadtochiy. Free vibration of periodically poled ferroelectric plate. *Journal of Applied Physics*, 99(11):114106 – 1, 2006.
- [101] G. Imeshev, M. Proctor, and M. M. Fejer. Lateral patterning of nonlinear frequency conversion with transversely varying quasi-phase-matching gratings. *Optics Letters*, 23(9):673 – 5, 1998.
- [102] Z. D. Gao S. N. Zhu S. Kurimura S. Y. Tu, A. H. Kung and K. Kitamura. Green-pumped high-power optical parametric oscillator based on periodically poled MgO-doped stoichiometric LiTaO₃. *Optics Letters*, 31(24):3632–3634, 2006.

- [103] Z. D. Gao, S. N. Zhu, S. Y. Tu, and A. H. Kung. Monolithic red-green-blue laser light source based on cascaded wavelength conversion in periodically poled stoichiometric lithium tantalate. *Applied Physics Letters*, 89(18):181101 – , 2006.
- [104] S. Bahbah, F. Bretenaker, and C. Drag. Single-frequency quasi-continuous red radiation generated by a green-pumped singly resonant optical parametric oscillator. *Optics Letters*, 31(9):1283 – 5, 2006.
- [105] K. Sakai, Y. Koyata, and Y. Hirano. Planar-waveguide quasi-phase-matched second-harmonic-generation device in Y-cut MgO-doped LiNbO₃. *Optics Letters*, 31(21):3134 – 6, 2006.
- [106] M. Lobino, M. Marangoni, R. Ramponi, E. Cianci, V. Foglietti, S. Takekawa, M. Nakamura, and K. Kitamura. Optical-damage-free guided second-harmonic generation in 1 % MgO-doped stoichiometric lithium tantalate. *Optics Letters*, 31(1):83 – 5, 2006.
- [107] M. Marangoni, M. Lobino, R. Ramponi, E. Cianci, and V. Foglietti. High quality buried waveguides in stoichiometric LiTaO₃ for nonlinear frequency conversion. *Optics Express*, 14(1):248 – 253, 2006.
- [108] P. J. Matthews, A. R. Mickelson, and S. W. Novak. Properties of proton exchange waveguides in lithium tantalate. *Journal of Applied Physics*, 72(7):2562 – 74, 1992.
- [109] D. Eger, M. A. Arbore, M. M. Fejer, and M. L. Bortz. High intensity illumination effects in LiNbO₃ and KTiOPO₄ waveguides. *Journal of Applied Physics*, 82(3):998 – 1005, 1997.